AN ANALYSIS OF SELF-SIMILARITY, MOMENTUM CONSERVATION AND ENERGY TRANSPORT FOR AN AXISYMMETRIC TURBULENT JET THROUGH A STAGGERED ARRAY OF RIGID EMERGENT VEGETATION

A Thesis

by

JON SCOTT ALLEN

Submitted to the Office of Graduate Studies of
Texas A&M University
in partial fulfillment of the requirements for the degree of

MASTER OF SCIENCE

Chair of Committee,	Scott Socolofsky
Committee Members,	Kuang-An Chang
	Achim Stössel
Head of Department,	John Niedzwecki

August 2013

Major Subject: Ocean Engineering

ABSTRACT

Marsh vegetation is widely considered to offer protection against coastal storm damage, and vegetated flow has thus become a key area of hydrodynamic research. This study investigates the utility of simulated *Spartina alterniflora* marsh vegetation as storm protection using an ADV measurement technique, and is the first to apply jet self-similarity analysis to characterize the overall mean and turbulent flow properties of a three-dimensional axisymmetric jet through a vegetated array.

The mean axial flow of a horizontal axisymmetric turbulent jet is obstructed by three configurations of staggered arrays of vertical rigid plant stems. The entire experiment is repeated over five sufficiently high jet Reynolds number conditions to ensure normalization and subsequent collapse of data by nozzle velocity so that experimental error is obtained.

All self-similarity parameters for the unobstructed free jet correspond to typical published values: the axial decay coefficient B is 5.8 ± 0.2, the Gaussian spreading coefficient c is 85 ± 5, and the halfwidth spreading rate $\eta_{1/2}$ is 0.093 ± 0.003. Upon the introduction of vegetation, from partially obstructed to fully obstructed, B falls from 5.1 ± 0.2 to 4.2 ± 0.2 and finally 3.7 ± 0.1 for the fully obstructed case, indicating that vegetation reduces axial jet velocity.

Cross-sectionally averaged momentum for the unobstructed free jet is $M/M_0 = 1.05 \pm 0.07$, confirming conservation of momentum. Failure of conservation of momentum is most pronounced in the fully obstructed scenario—$M/M_0 = 0.54 \pm 0.05$. The introduction of vegetation increases spreading of the impinging jet. The entrainment coefficient α for the free jet case is 0.0575; in the fully obstructed case, $\alpha = 0.0631$.

Mean advection of mean and turbulent kinetic energy demonstrates an expected reduction in turbulence intensity within the vegetated array. In general, turbulent production decreases as axial depth of vegetation increases, though retains the bimodal profile of the free jet case; the fully vegetated case, however, exhibits clear peaks behind plant stems. Turbulent transport was shown to be unaffected by vegetation and appears to be primarily a function of axial distance from the jet nozzle.

An analysis of rate of dissipation revealed that not only does the cumulative effect of upstream wakes overall depress the magnitude of spectral energy density across all wavenumbers but also that plant stems dissipate large anisotropic eddies in centerline streamwise jet flow. This study, thus, indicates that sparse emergent vegetation both reduces axial flow velocity and has a dissipative effect on jet flow. Typically, however, storm surge does not exhibit the lateral spreading demonstrated by an axisymmetric jet; therefore, the results of this study cannot conclusively support the claim that coastal vegetation reduces storm surge axial velocity.

TABLE OF CONTENTS

LIST OF FIGURES

LIST OF TABLES

TABLE Page

1. INTRODUCTION

Increasing interest in protecting coastal settlements, environments and infrastructure from storm damage has promoted research into not only manmade coastal protection, such as flow and scour around seawalls and pilings, but also natural protective structures, including dunes and wetlands. This study seeks to investigate a frequently made argument that marsh vegetation reduces storm surge, specifically by simulating *Spartina alterniflora* vegetation—a common rigid, emergent wetland grass—as a staggered array of cylinders.

Various configurations of this vegetation are placed downstream of a fully turbulent jet to investigate how the axial distance of flow impingement from the jet nozzle affects downstream conditions. Alongside a standard calculation of turbulent kinetic energy and dissipation, the axial velocity decay and radial spreading of the altered jet are compared to a validated free jet scenario to determine if free jet self-similarity parameters can be adapted to vegetative flow. These measurements are important because demonstrated validation of self-similarity analysis to jets in vegetated flows permits generalization of the entire flow field in terms of self-similarity parameters and thus the application of a wide range of techniques and methods of characterizing self-similar jet flows.

The self-similarity of the axisymmetric turbulent jet has been studied extensively over the last fifty years, not only for its frequency in nature but also for the remarkable accuracy with which it represents flow under diverse initial conditions. Early studies developed the currently used momentum-based approach to characterize mean flows, turbulence intensities and energy transport as functions of axial and radial distance from the jet nozzle (Rajaratnam, 1976), (Wygnanski and Fiedler, 1969) and (Hussein et al., 1994). Sufficiently far from the jet nozzle in this self-symmetric region called the zone of established flow, jet velocities are dependent only on initial conditions (Xu and Antonia, 2002). Several other studies consider the potential cone in the zone of flow establishment prior to transition to self-symmetry in the zone of established flow (Keller, 1994) and (Liepmann, 1991).

Entrainment, the process by which ambient fluid is captured primarily through large-scale engulfment by vortical structures on the edge of the jet cone, is generally described in terms of a coefficient relating a mean radial entraining velocity at the edge the jet cone to the mean axial centerline velocity (Falcone, 2003). Ambient fluid, prior to entrainment, is in an irrotational state beyond the radial jet edge; however, once entrained, it acquires a vorticity and is advected downstream (Bremhorst and Harch, 1978). On a lesser scale, viscous diffusion of vorticity extracts external fluid into the turbulent flow and initiates small-scale motion of already entrained fluid (Turner, 1986). As a result, a packet of entrained fluid is not instantaneously fully and uniformly entrained; rather, pockets of irrotational fluid may still be found within the jet, but are best detected with instantaneous two-dimensional methods (Dahm, 1987).

Despite its frequency in literature, the applicability of the entrainment coefficient for round jets has recently been called into question (Agrawal and Prasad, 2003). Although the understanding of the underlying physics of the round turbulent jet has not changed drastically in the last half century, the definitions of self-similarity parameters have evolved (Liepmann, 1991). Current research efforts have focused on explaining shortfalls in conservation of momentum and agreement with predictions of kinetic energy terms. Nevertheless, the axisymmetric turbulent jet remains one of the most predictable, reproducible and widely studied flows.

Typical instruments of measurement include both point-wise acoustic dopper velocimetry (ADV) and planar particle image velocimetry (PIV). The former, employed in the present study, permits extensive statistical analysis and determination of subtle three-dimensional turbulent correlations; the latter, records two-dimensional snapshots of particle motion and enables determination of instantaneous vorticity and flow patterns.

Coastal vegetation has often been promoted as a first line of defense against storm surge. A rule of thumb states that 14.5 km of wetland reduces storm surge by 1 m, according to a 1963 report by the United States Army Corps of Engineers (Wamsley, 2010). This generalization is difficult to definitively confirm or disprove due to the large number of flow, storm and marsh characteristics; however, certain parameters can be measured under controlled conditions. Some studies investigate the effects of wake formation behind one or two cylinders (Luo et al., 1996) and (Kiya et al., 1980). Several experimental studies consider flow, especially drag and dissipation, through arrays of vegetation in channel flow (Nepf, 1999), (Liu et al., 2008), (Murphy et al., 2007), (James et al., 2004), (Kadlec, 1990) and (Tanino and Nepf, 2008). Recently, such flows have been mathematically modeled (Braun and Kudriavtsev, 1995), (Huai et al., 2009) and (Stoesser et al., 2009).

The present study seeks to further the understanding of vegetated flows by obstructing the zone of established flow of a free turbulent jet with sparsely vegetated arrays. Because the turbulence and mixing properties of jets are well known, changes in jet behavior upon impingement with simulated vegetation reveal the influence of plant arrays on jet physics. Application of standard jet self-similarity parameters to obstructed flow allows for the comparison of vegetated flow configurations to one another, as well as to the validation free jet scenario. By developing a network of measurement stations and validating self-similar conservation of momentum, entrainment and kinetic energy for a free jet, this same network can be used to study deviations from a free jet caused by the introduction of simulated vegetation.

The instrument of measurement, an ADV, allows high-frequency recording of three-dimensional velocities so that mean and turbulent parameters could be determined with accuracy. In addition to the free jet configuration, three additional configurations of vegetated arrays are subjected to five fully turbulent flow speeds with sufficiently high Reynolds numbers to permit the averaging, or collapse, of jet speeds.

As a result, the analysis allows the computation of mean flow parameters, Reynolds stresses and turbulent transport triple products with greater accuracy, as well as enabling the calculation of experimental error. By effectively bridging the gap between axisymmetric jet studies and open channel vegetation studies, this study quantitatively describes hydrodynamic parameters ranging from enhanced simple axial velocity decay to complex vegetation wake effects.

2. EXPERIMENTAL SETUP

2.1 Main tank

The experiment was conducted in the Hydrodynamic Laboratory Building in the Ocean Engineering Program at Texas A & M University at College Station. The experimental tank is an open and elevated glass-fronted steel tank measuring $1.30m$ in height, $1.32m$ in width and $3.00m$ in length. A top-mounted rack allows steady, precise three-dimensional instrument placement within the tank. To remedy unevenness in the tank bottom, a false floor was installed, thus providing a plane and level surface for placement of rigid simulated vegetation and the jet outlet stand.

2.2 Jet assembly and constant head tank

A constant head tank is a simple and reliable means of establishing and maintaining a jet with reproducible initial conditions. In this study, an open five-gallon bucket of a ten-inch diameter is suspended by a crane above the main tank, see Figure 2.1. Supplied by a high-speed and -volume bilge pump positioned under the false floor in the far downstream portion of the main tank, the water level in the bucket is held constant at $0.229m$ above the bucket bottom. Surplus water exits the bucket through perforations above the target water level and falls into a pan that returns the excess water to the experimental tank through a diffuser situated under the false floor and isolated from the upper jet flow chamber by horsehair lining.

Water is drawn continuously from the bottom of the bucket through a $3.66m$ long flexible tube with a $1.27cm$ inner diameter and expelled from a $0.12m$ rigid plastic tube with an inner diameter of $6.35cm$. This extended nozzle was designed to ease calibration and reduce tangential motion of the fluid. Although the main tank was filled to $0.387m$, the jet outlet was positioned so that the expanding jet cone remained

Figure 2.1: Suspended constant head tank at maximum vertical extent and experimental tank

sufficiently distant from walls, floor and free surface within the measurement domain.

Effectively, the jet vertical centerline is $0.187m$ above the false floor and $0.200m$ under the free surface throughout the measured range. Shinneeb et al. (2011) employed a similar main tank and jet setup, but varied the jet centerline and measurement plane vertically at a ratio of H/d, where $H/2$ is distance from free surface to jet centerline and d is jet nozzle diameter. That study considered $5 \leq H/d \leq 15$; the present study, for reference, has a fixed $H/d = 59$ (Shinneeb et al., 2011).

It is known that the halfwidth of an axisymmetric, incompressible non-buoyant jet will expand at an angle of $5.43°$ with respect to the jet centerline (Lipari, 2011). The jet height was chosen so that the maximum streamwise extent of measurements at $0.914m$ occurs at twice the halfwidth b, see Figure 2.2, and well before wall effects have measurable influence on self-similarity. Necessitated by irregularities in the shape of the tank bottom, placement of the false floor resulted in the mounted jet centerline measuring $73.7cm$ from the left wall and $58.4cm$ from the right wall.

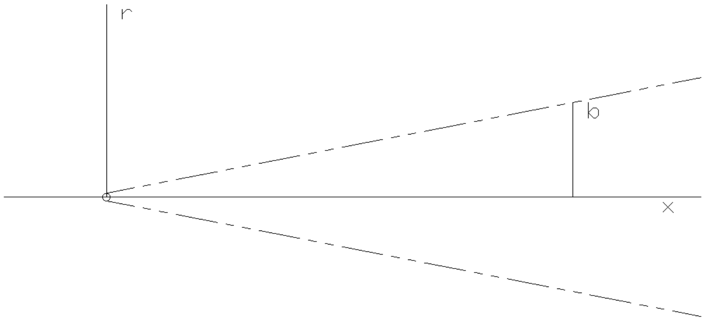

Figure 2.2: Plan view of measurement plane coordinate system

Though the jet cone does not contact either wall, the offset produces a slight variance in the tank recirculation current that is discernible in the resultant spanwise velocity profiles.

The constant head tank is raised or lowered to produce a range of turbulent initial nozzle velocities, of which five were chosen to generate collapsible profiles to improve experiment accuracy and permit the determination of experimental error. The highest tank placement Δh, $1.93m$ difference between water level of constant-head tank and water level of main tank, was the maximum vertical extent of the crane, and the lowest tank placement, $0.71m$, was the minimum elevation for which the return pan siphon would function. Intermediate placements occurred at $1.63m$, $1.32m$ and $1.02m$.

After measuring flow volumes for these volumes at the water surface in the main tank, the various placement heights produced the bulk velocities u_0 in Table 2.1, assuming a top-hat initial nozzle velocity profile (Xu and Antonia, 2002). Each jet ex-

Table 2.1: Constant-head tank placement and speed

Speed	Δh m	$\overline{u_0}$ m/s	$Re_{\overline{M_0}}$
1	1.93	3.31	18600
2	1.63	3.06	17200
3	1.32	2.77	15500
4	1.02	2.45	13700
5	0.71	2.08	11700

hibits fully turbulent initial conditions, $Re_{\overline{M_0}} \geq 4000$, where $Re_{\overline{M_0}}$, non-dimensional momentum Reynolds-like number, is defined by

$$Re_{\overline{M_0}} = \sqrt{\frac{\overline{M_0}}{\rho}}\frac{1}{\nu} \tag{2.1}$$

where $\overline{M_0}$ is mean initial momentum at the nozzle, ρ is density and ν is kinematic viscosity (Lipari, 2011). An alternate form of the Reynolds number with bulk discharge velocity as characteristic velocity scale is occasionally used and is defined by

$$Re_{\overline{u_0}} = \frac{\overline{u_0}d}{\nu} \tag{2.2}$$

where $\overline{u_0}$ is mean initial velocity at the nozzle and d is the jet outlet diameter. By geometry, $Re_{\overline{u_0}}/Re_{\overline{M_0}} = 1.13$ for radially axisymmetric jets (Lipari, 2011).

The described jet and tank setup is typical of modern jet studies. Due to the wealth of literature regarding free jets, it is important to reproduce accepted jet self-similarity in the present measurements before extending analysis to vegetated arrays, presented in Chapter 3.

2.3 Plant array

Without installation of vegetation, this study confirms accepted self-similarity and conservation parameters of axisymmetric jets. In this study, however, this initial analysis serves as a calibration and a necessary stepping stone to studying the effects of introducing simulated vegetation as an obstacle to flow. Once validated as a self-similar, conserving jet, arrays of simulated *Spartina alterniflora*, smooth cordgrass, are inserted in three configurations for each of the five test speeds.

Spartina alterniflora is a common rigid, emergent wetland plant and is simulated here by smooth acrylic rods of $6.35mm$ diameter vertically mounted on $0.305m$ by $0.914m$ acrylic sheets in an equidistant staggered pattern so that each interior plant is $8.8cm$ from each of its six neighbors, similar to the mathematical model proposed by Braun and Kudriavtsev (1995), though sparser. Stem oscillation produces random fluid-elastic instabilities and thus produces undesirable symmetric vortex shedding (Abd-Rabbo and Weaver, 1986) and (Jendrzejczyk et al., 1979). This undesired velocity-induced vibration was eliminated by mounting an aluminum c-channel atop rows of vegetation for $24 \leq x/d \leq 72$ perpendicular to the jet centerline.

Although relatively sparse compared to recent open-channel vegetation studies—vegetation density per meter a, given by

$$a = \frac{d}{\Delta S^2} \tag{2.3}$$

where ΔS is inter-plant spacing and compared with other studies in Table 2.2—it is this sparseness that retains the basic shape of the jet cone and enables comparison(Nepf, 1999). In nearly all studies of emergent, rigid vegetation, only plant stems—actual or simulated—are installed; in at least two instances, however, arrays of both simulated *Spartina alterniflora* stems and leaves were studied (Nepf et al.,

Table 2.2: Studies involving flow through vegetated arrays

Study	ad	Sensor type
present study	0.0052	ADV
Abd-Rabbo and Weaver (1986)	0.5	Tracer particles and camera
Balachandar and Parker (2002)	—	Numerical model
Braun and Kudriavtsev (1995)	0.25	Numerical model
Huai et al. (2009)	0.0036	ADV
Leonard and Luther (1995)	0.003 – 0.083	LDV
Lightbody and Nepf (2006)	0.01	ADV
Liu et al. (2008)	0.016	LDV
Murphy et al. (2007)	0.015 – 0.048	ADV, LDV and FVA
Neary (2003)	—	Numerical model
Nepf (1999)	0.008 – 0.07	ADV and LDV
Nepf et al. (1997)	0.007 – 0.288	ADV and LDV
Neumeier (2004)	—	ADV
Pye et al. (1995)	0.006	Current meter
Stoesser et al. (2009)	0.02	Numerical model
Tanino and Nepf (2008)	0.12 – 0.45	ADV

1997) and (Lightbody and Nepf, 2006). Yagci et al. (2010) found that the accuracy of a rigid cylinder representing an actual plant in terms of axial velocity reduction depended on the depth of the measurement plane.

In addition to the non-dimensional parameter ad, where d is stem diameter, plant density can be expressed by the dimensionless parameter ϕ, defined as

$$\phi = mA_S \tag{2.4}$$

where m is number of plants per horizontal area and A_S is stem cross-sectional area (Tanino and Nepf, 2008). There is no simple conversion from one parameter to another. By definition, ad is the preferred dimensionless vegetation density parameter for equidistant regular arrays, whereas ϕ is well suited for dense, random placements, such as simulated mangroves (Tanino and Nepf, 2009). For the present study, $ad = 0.0052$ and $\phi = 0.00477$. This ad was chosen to compare with other studies investigating *Spartina alterniflora*. The typical density of emergent marsh grasses with rounded stems is typically $0.01 \leq a \leq 0.07\frac{1}{cm}$ (Nepf and Ghisalberti, 2008).

Vortices shed from upstream cylinders attach to downstream inline cylinders, whereas side-by-side cylinders favor a mode of vortex shedding equivalent to an isolated cylinder if spacing is adequate (Kiya et al., 1980) and (Akilli et al., 2004). If $\Delta S \leq 1.4d$, no matter the orientation, as is the case in very dense arrays, the same study found that adjacent cylinders act as a single body in terms of vortex shedding (Kiya et al., 1980). In the present study, the staggered cylinder placement is between both of these extremes, so that while the first rows of plant stems appear to shed vortices as isolated cylinders; stems in the interior of the array not only shed their own vortices but also are subjected to vortices shed by upstream rows. Staggered arrays produce more flow resistance than inline arrays (Liu et al., 2008).

Vegetated plates were installed in three configurations, see Figure 2.3. In the free-jet configuration, no simulated vegetation is present; this configuration serves to validate the setup and analysis. This jet assembly was specifically chosen to replicate the most prevalent jet in literature, the axisymmetric radial jet. In Configuration 1, two vegetated arrays are inserted so that the free jet cone enters vegetation for $x/d > 120$ and all but Section 4 are within the free jet region. In configurations 2 and 3, the free jet cone enters vegetation at a smaller x/d, as described in Table 2.3.

Therefore, Configuration 1 represents a fully developed and self-similar jet flow in the distant zone of established flow at the point of impingement with vegetation. By contrast, the point of impingement for Configuration 3 is early within the zone of flow establishment. Configuration 2 is an intermediate stage between configurations 1 and 3, in which the flow impinges on vegetation within the early zone of established

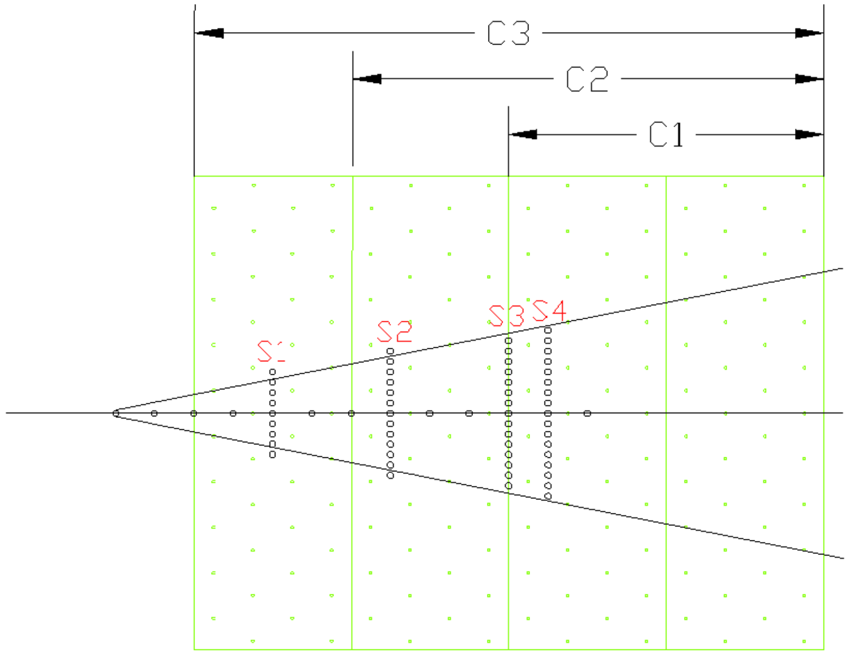

Figure 2.3: Plan view of measurement stations with sections and configurations indicated

Table 2.3: Extent of vegetation by configuration

Configuration	Free jet range x/d	Sections	Vegetated range x/d	Sections
Free jet	0 – 216	1 – 4	—	—
1	0 – 120	1 – 3	120 – 216	4
2	0 – 72	1	72 – 216	2 – 4
3	0 – 24	—	24 – 216	1 – 4

flow. The zone of established flow, as determined by this study, occurs between $12 < x/d < 24$, as is discussed in Chapter 3.2.

2.4 Measurement and record length

A 3D Nortek Vectrino ADV, with the control volume vertically centered on a measurement plane parallel to the water surface and vertically coincident with the jet centerline, recorded velocity in streamwise, spanwise and tangential directions. The addition of a fourth acoustic leg permitted the measurement of two vertical velocities; these were averaged to produce a single tangential velocity, thus the terms tangential and vertical are equivalent due to alignment.

The initial axial nozzle velocity was on the order of $1m/s$; therefore, a sampling rate of $50Hz$ was chosen to capture statistically independent samples and the main tank was seeded with seeding particles to ensure sufficiently high signal-to-noise ratio and signal correlation. Initial attempts to reduce tank recirculation with horsehair mounted on the far downstream wall resulting in substantial loss of ADV seed particles. Removal of the horsehair did result in a visible recirculation current visually estimated at no more than $0.01m/s$, which, as results will demonstrate, has a minimal effect on velocity profiles and no clear effect on momentum conservation or entrainment halfwidth. The sampling frequency should be at least twice as high as the highest frequency of interest, the so-called Nyquist frequency (Atta, 1974). In order to determine optimal record length, the ADV was positioned in the wake of a cylinder at a downstream position in fully vegetated flow. Allowing a maximum 10% deviation threshold for any realization from the full record axial mean, the minimum sample length at $50Hz$ was $36.3s$. Because the mean axial centerline velocity serves as a characteristic velocity scale, it is important to achieve an accurate mean.

In general, however, the record length at each station was $140 - 180s$. Radial and

Table 2.4: Location and extent of measurement sections

Section	Alignment	Stations	x/d	$(r/r_{1/2})_{max}$
1	radial	9	48	2.70
2	radial	13	84	2.25
3	radial	15	120	1.71
4	radial	17	132	1.85
5	axial	12	$12 - 144$	0

tangential velocities are considerably smaller in magnitude and variable and are not characteristic length scales; therefore, higher deviation is permitted. At this sample length, maximum deviation of radial and tangential velocity realizations from mean are approximately 75% and 200%, respectively, due to the small magnitude of these velocities and a raw mean of zero, see figures B.1– B.8 in Appendix B. Over all sections and configuration, $\frac{\overline{v}}{\overline{u_c}} < 0.1$ and $\frac{\overline{w}}{\overline{u_c}} \ll 0.1$.

In order to capture adequate spatially varying velocity data, the selected testing pattern, see Figure 2.3 and Table 2.4, consisted of 64 axial and radial measurement stations. Twelve equidistant centerline measure stations at a spacing of $7.62cm$, the first of which is placed $7.62cm$ downstream of the jet nozzle, record axial decay. Radial measurement stations resemble perpendicular branches off of the axial measurement line and extend a distance of twice the anticipated free-jet halfwidth—defined as the radial distance at which $u(\eta) = u_c/2$—each side of the centerline at a spacing of $2cm$. Aside from Section 1, which has only 9 stations total, this radial measurement spacing produced sufficient radial resolution to demonstrate momentum conservation of the free jet case with low error.

2.5 Postprocessing

Raw ADV output includes instantaneous velocity, correlation and signal-to-noise ratio in three Cartesian directions. Although there is value to this raw velocity and its

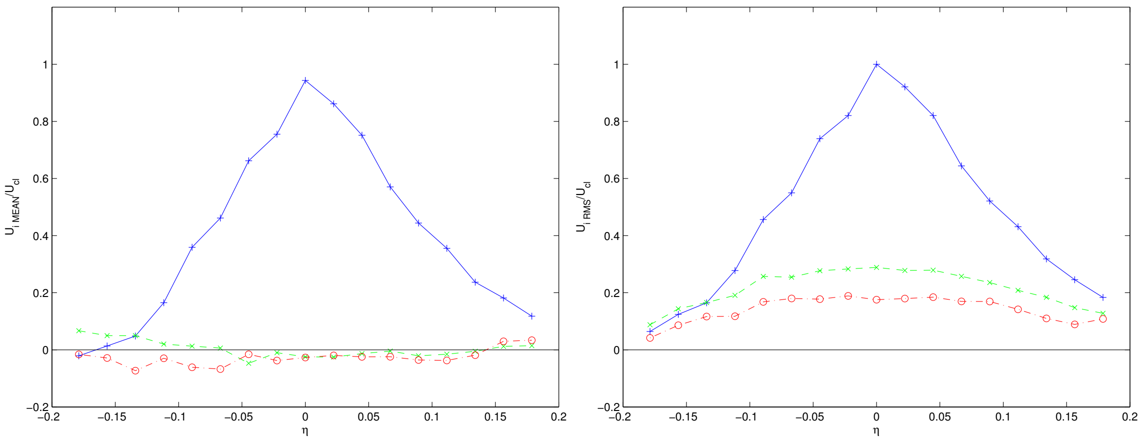

(a) $\overline{\mathrm{u_i}}$ mean

$\overline{u}(+)$ $\overline{v}(\times)$ $\overline{w}(\bigcirc)$

(b) $\overline{\mathrm{u_i}}$ RMS

$\overline{u}(+)$ $\overline{v}(\times)$ $\overline{w}(\bigcirc)$

Figure 2.4: Normalized spanwise mean velocity profiles for Section 4 of the free jet

mean over the entire record, it is common practice to compute the root-mean-square (RMS) to obtain turbulent strength according to

$$u' = \sqrt{\frac{1}{N}\sum_{i=1}^{N}(u_i')^2} = \sqrt{\frac{1}{N}\sum_{i=1}^{N}(u-\overline{u})^2} \tag{2.5}$$

where u' is a turbulent fluctuation and $\overline{u}$ is a mean velocity (Carollo et al., 2002). Figures 2.4 and 2.5 illustrate the comparative amplitudes of mean and RMS velocity profiles of the same data set, Section 4 of the free jet, normalized to centerline axial velocity.

In many cases, it may be preferable to despike ADV data prior to use. Based on the physics-based approach to detect and smooth spikes described in Goring and Nikora (2002), the present study initially used a modified version of this algorithm that maintains peaks of a user-defined minimum peak width. Additional spatial and temporal despiking techniques are available for particle image velocimetry (PIV)

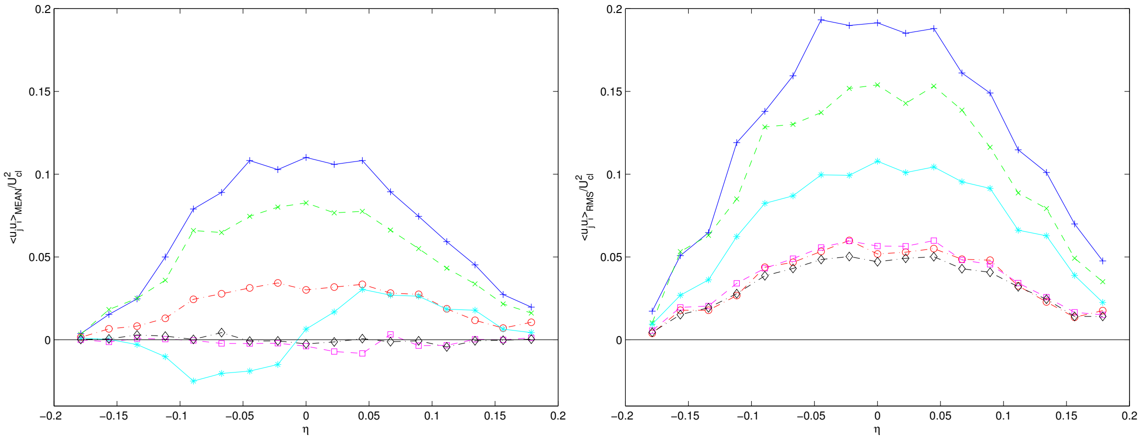

(a) $\overline{u'_j u'_i}$ mean

$\overline{u'u'}(+)$ $\overline{v'v'}(\times)$ $\overline{w'w'}(\bigcirc)$

$\overline{u'v'}(*)$ $\overline{u'w'}(\Box)$ $\overline{v'w'}(\Diamond)$

(b) $\overline{u'_j u'_i}$ RMS

$\overline{u'u'}(+)$ $\overline{v'v'}(\times)$ $\overline{w'w'}(\bigcirc)$

$\overline{u'v'}(*)$ $\overline{u'w'}(\Box)$ $\overline{v'w'}(\Diamond)$

Figure 2.5: Normalized spanwise Reynolds stress profiles for Section 4 of the free jet

(Weisgraber and Liepmann, 1998). Although error was marginally reduced in unobstructed near-centerline flow, peak preservation modifications failed to retain sufficient detail of large-scale turbulent structures along the entrainment boundary, as well as behind stem wakes within the plant array. Overall, an average 5% of momentum was lost at sections 3 and 4, see Figure 2.6. In addition, there was no physical justification for the removal of turbulent peaks; therefore, it was decided to retain all raw velocity data, though the occasional aberrant reading may have insignificantly elevated averaged derived quantities, such as volumetric flow rate, momentum and energy.

As described in Chapter 2.2, the slight offset of the jet centerline within the main tank resulted in unequal recirculation currents. This effect, visible in all spanwise velocity profiles, is small and consistent across all cross-section and does not displace the jet mean from the centerline. Jet self-similarity parameters are defined for a

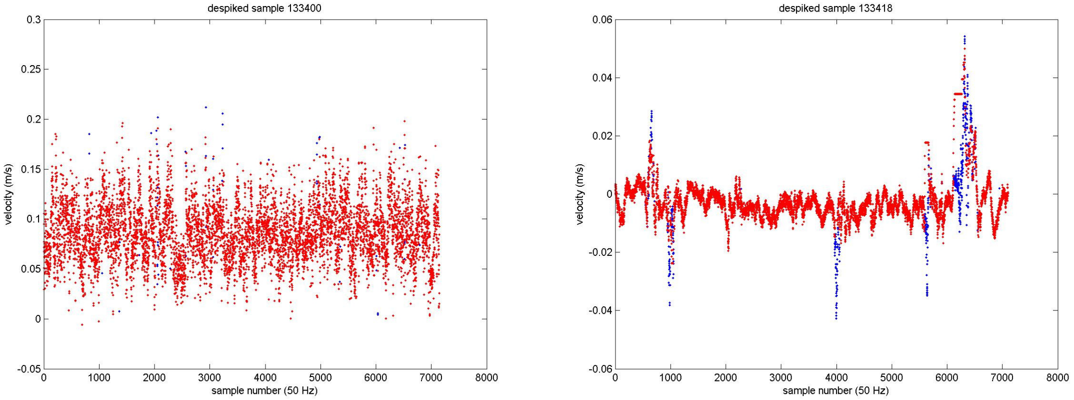

(a) Centerline

Configuration 3 Speed 3

Section 4 Station 00

removed points in blue

(b) Entrainment boundary

Configuration 3 Speed 3

Section 4 Station 18

removed points in blue

Figure 2.6: Despiked ADV data

presumed Gaussian curve with a maximum mean coincident with the jet centerline; therefore, the curve is folded and averaged about the centerline to produce a spanwise Gaussian profile with symmetric sides, see Figure 2.7. During early alignment of the jet, the ADV was set to record at varying distances along the jet centerline; records were processed and Gaussian fitted to ensure vertical and horizontal centerline alignment. Due to the slight unequal recirculation present within the tank, most radial profiles exhibit variability at extreme radial stations.

Each measurement station was tested under three configurations at five speeds, in addition to free jet configurations, across each of the 64 stations. All five jet speeds are well-developed turbulent flows, and therefore, as expected from jet theory, collapse upon normalization with respect to respective initial nozzle velocity. Thus, after collapse, the fifteen vegetated runs produce three collapsed data sets—one for each configuration—as well as the free jet validation runs. Throughout the

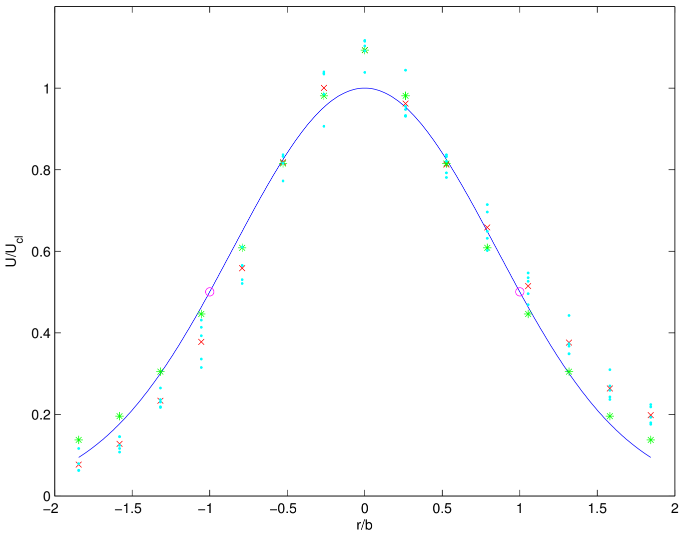

Figure 2.7: Example Gaussian fit to spanwise axial velocity profile

realization(·) raw mean(×) folded mean(∗) halfwidth(◯) Gaussian fit(−)

remainder of this study, referenced quantities are speed averaged, and the corresponding errors are the Gaussian standard deviation of the normalized five speeds prior to averaging. To obtain the collapsed velocity, each computed mean value is normalized with respect to its bulk nozzle velocity. These five non-dimensional mean values are then averaged to obtain the collapsed value. This procedure is applied to mean velocities, Reynolds stresses and turbulent transport triple products, though the power of the normalizing bulk velocity is adjusted to obtain a non-dimensional mean. Figure 2.7 illustrates the collapsing of the five speeds to a single raw mean value and demonstrates the effect of the recirculation at extreme radial measurement stations.

3. FREE JET

3.1 Types of jets

Fluid turbulent jets are widely studied not only for their frequency in nature and utility in industrial applications but also for their remarkable property of self-similarity. Over five decades of research has produced a large body of data regarding the jet characteristics of multiple configurations, thus enabling the study of other phenomena through jets. Well away from the point of inflow, in the zone of established flow, variability in the self-similarity parameters of a downstream jet can infer the behavior of upstream obstacles or flow conditions.

Rajaratnam (1976) describes the equations of motion and solutions to several types of jets—including plane, circular, radial, compound and wall jets. The circular jet employed in this study, in particular, is well described in literature and, due to axisymmetry, allows for simplification of the equations of motion. Further specifications—such as no swirl or initial tangential velocity, isotropic buoyancy, incompressibility of jet and quiescent ambient fluid, and steady flow—permit substantial further simplification.

Early studies have assumed that for a sufficiently turbulent jet in an ideally infinite and quiescent domain, downstream conditions are only a function of initial conditions, including Reynolds number and jet velocity profile, the latter because physical jets are not point sources (Hussain and Zaman, 1981) and (Hussein et al., 1994).

Due to axisymmetry, jet geometry is described in cylindrical coordinates, where x denotes streamwise or axial distance; r, streamwise or radial distance; and θ, tangential angle. The measurement plane is horizontal to the water surface and is bisected by the jet flow centerline; therefore, θ also describes the vertical displacement. Respective velocities are u, v and w.

The Navier-Stokes equations with constant density and kinetic viscosity and without external forces are given by

$$\begin{aligned}
\frac{\partial u}{\partial x}+\frac{1}{r}\frac{\partial}{\partial r}(rv)+\frac{1}{r}\frac{\partial w}{\partial \theta} &= 0 && (3.1)\\
\frac{\partial u}{\partial t}+(\mathbf{u}\cdot\nabla)\,u &= -\frac{1}{\rho}\frac{\partial p}{\partial x}+\nu\nabla^2 u && (3.2)\\
\frac{\partial v}{\partial t}+(\mathbf{u}\cdot\nabla)\,v-\frac{w^2}{r} &= -\frac{1}{\rho}\frac{\partial p}{\partial r}+\nu\left(\nabla^2 v-\frac{v}{r^2}-\frac{2}{r^2}\frac{\partial w}{\partial \theta}\right) && (3.3)\\
\frac{\partial w}{\partial t}+(\mathbf{u}\cdot\nabla)\,w+\frac{vw}{r} &= -\frac{1}{\rho}\frac{\partial p}{\partial \theta}+\nu\left(\nabla^2 w-\frac{w}{r^2}-\frac{2}{r^2}\frac{\partial v}{\partial \theta}\right) && (3.4)
\end{aligned}$$

where

$$\begin{aligned}
(\mathbf{u}\cdot\nabla) &= u\frac{\partial}{\partial x}+v\frac{\partial}{\partial r}+\frac{w}{r}\frac{\partial}{\partial \theta} && (3.5)\\
\nabla^2 &= \frac{\partial^2}{\partial x^2}+\frac{1}{r}\frac{\partial}{\partial r}\left(r\frac{\partial}{\partial r}\right)+\frac{1}{r^2}\frac{\partial^2}{\partial \theta^2} && (3.6)
\end{aligned}$$

(Kundu and Cohen, 2008). For a swirl-free and steady flow, $\frac{\partial}{\partial\theta}$ and $\frac{\partial}{\partial t}$, respectively, are equal to zero. Equations 3.1 to 3.4 thus reduce to

$$\begin{aligned}
\frac{\partial u}{\partial x}+\frac{1}{r}\frac{\partial}{\partial r}(rv) &= 0 && (3.7)\\
\left(u\frac{\partial}{\partial x}+v\frac{\partial}{\partial r}\right)u &= -\frac{1}{\rho}\frac{\partial p}{\partial x}+\nu\nabla^2 u && (3.8)\\
\left(u\frac{\partial}{\partial x}+v\frac{\partial}{\partial r}\right)v-\frac{w^2}{r} &= -\frac{1}{\rho}\frac{\partial p}{\partial r}+\nu\left(\nabla^2 v-\frac{v}{r^2}\right) && (3.9)\\
\left(u\frac{\partial}{\partial x}+v\frac{\partial}{\partial r}\right)w+\frac{vw}{r} &= \nu\left(\nabla^2 w-\frac{w}{r^2}\right) && (3.10)
\end{aligned}$$

In Cartesian coordinates, the two-dimensional continuity equates $\frac{\partial u}{\partial x}=-\frac{\partial v}{\partial y}$; however, the additional term within the cylindrical form of the Navier-Stokes equations

$\frac{\partial u}{\partial x} = -\frac{\partial v}{\partial r} - \frac{v}{r}$ complicates simplification. By multiplying all terms of the continuity equation by u and collecting terms, Equation 3.7 produces

$$\frac{\partial u^2}{\partial x} - u\frac{\partial u}{\partial x} + \frac{1}{r}\frac{\partial}{\partial r}(ruv) - v\frac{\partial u}{\partial r} = 0 \tag{3.11}$$

Likewise, Equation 3.7 produces

$$\frac{\partial uv}{\partial x} - u\frac{\partial v}{\partial x} + \frac{1}{r}\frac{\partial}{\partial r}\left(rv^2\right) - v\frac{\partial v}{\partial r} = 0 \tag{3.12}$$

if multiplied by v and

$$\frac{\partial uw}{\partial x} - u\frac{\partial w}{\partial x} + \frac{1}{r}\frac{\partial}{\partial r}(rvw) - v\frac{\partial w}{\partial r} = 0 \tag{3.13}$$

if multiplied by w (Rajaratnam, 1976).

Adding Equation 3.11 to the left side of the streamwise conservation of momentum Equation 3.8 and simplifying results in

$$\frac{\partial u^2}{\partial x} + \frac{1}{r}\frac{\partial}{\partial r}(ruv) = -\frac{1}{\rho}\frac{\partial p}{\partial x} + \nu u \nabla^2 u \tag{3.14}$$

(Rajaratnam, 1976). Analogous operations produce the spanwise and tangential conservation of momentum expressions

$$\frac{\partial uv}{\partial x} + \frac{\partial v^2}{\partial r} + \frac{v^2 - w^2}{r} = -\frac{1}{\rho}\frac{\partial p}{\partial r} + \nu v\left(\nabla^2 v - \frac{v}{r^2}\right) \tag{3.15}$$

$$\frac{\partial uw}{\partial x} + \frac{1}{r}\frac{\partial rvw}{\partial r} + \frac{vw}{r} = \nu w\left(\nabla^2 w - \frac{w}{r^2}\right) \tag{3.16}$$

In a jet with no initial swirl, tangential velocities are small compared to streamwise and spanwise velocities over the entire domain, and derivatives of the product including a tangential velocity are yet smaller. As a result, terms $\frac{\partial uw}{\partial x}$ and $\frac{1}{r}\frac{\partial rvw}{\partial r}$ are neglected.

To apply these simplified equations of motion to turbulent jets, first implement Reynolds decomposition by splitting velocity into mean and turbulent components $u_i = \overline{u_i} + u_i{}'$, where $\overline{u}$ is mean axial velocity and u' is a turbulent fluctuation, into Equations 3.7, 3.14 and 3.15. Using an order-of-magnitude argument, the boundary layer approximation assumes that the axial stress gradient $\nu\partial^2 u/\partial x^2$is neglible (Rajaratnam, 1976). After averaging and neglecting the remaining small viscous terms these equations can be recast as

$$\begin{aligned}
\frac{\partial \overline{u}}{\partial x} &= -\frac{1}{r}\frac{\partial r\overline{v}}{\partial r} && (3.17)\\
\frac{\partial}{\partial x}\left(\overline{u}^2 + \overline{u'^2} + \frac{\overline{p}}{\rho}\right) &= -\frac{1}{r}\frac{\partial r\left(\overline{uv} + \overline{u'v'}\right)}{\partial r} && (3.18)\\
\frac{\partial \overline{u'v'}}{\partial x} &= -\frac{\partial}{\partial r}\left(\overline{v'^2} + \frac{\overline{p}}{\rho}\right) + \frac{\overline{w'^2} - \overline{v'^2}}{r} && (3.19)
\end{aligned}$$

(Hussein et al., 1994) and (Lipari, 2011).

This further simplification leaves only $\frac{wv}{r} = 0$ in Equation 3.16. Although this statement would suggest that any product including a tangential product may be neglected, and indeed this is common practice, it is preferrable to nominally retain the $\frac{w^2}{r}$ term in Equation 3.15 to account for normal tangential turbulent contributions, although another common assumption that $w^2 = v^2$ is occasionally used to further simplify Equation 3.15 and eliminates the governing equations of w altogether (Weisgraber and Liepmann, 1998) and (Browne et al., 1987).

This form of the governing equations is especially useful for determining an expression for momentum; this procedure is covered in detail in Lipari (2011) and produces an expression for momentum, see Equation 3.31.

3.2 Self-similarity

Inherent to circular free jets, radial velocity v and vertical velocity w are ideally zero at centerline. The form of self-similarity equations as proposed by Lipari (2011) are used for comparison against the historical reanalyses of several significant previous studies contained in the article.

Issuing forth from a nozzle of diameter d at a bulk mean velocity u_0, jet outflow spreads spanwise while quiescent ambient fluid is entrained, see Figure 2.2. Xu and Antonia (2002) studied the effects of jet initial conditions, in particular orifice configuration, and the development and emergence of the zone of established flow. In general, outlets are classified as either contraction nozzles or pipes, the former exhibiting a characteristic "top hat" initial axial velocity profile of uniform bulk velocity $\overline{u_0}$ and the latter, a logarithmic profile for turbulent pipe flow. The jet nozzle in this study consists of a 0.12 m pipe; however, exhibits an axial decay more consistent with a contraction nozzle. Although most studies include contraction nozzles, some recent studies have looked at pipe flows (Falcone, 2003).

Self-similarity becomes apparent in the zone of established flow, which is characterized by a centerline axial $\overline{u}_c$ velocity profile that decays inversely to distance along the centerline streamwise axis from the nozzle velocity and an axisymmetric radial velocity profile that decays inversely with respect to spanwise distance from flow centerline (Hussein et al., 1994). The onset of self-similarity begins as early as $6d$ (Kassab et al., 1996) and (Liepmann and Gharib, 1992). By visual inspection of streamwise axial velocity profiles, the present study suggests that the onset of emergent self-similarity presently occurs between $12 < x/d < 24$.

3.3 Axial velocity

The centerline axial velocity is related to the initial bulk nozzle velocity by

$$\frac{u_c}{u_0} = B\frac{d}{x - x_B} \tag{3.20}$$

(Lipari, 2011). A momentum virtual origin offset x_B is required because the free jet has an initial diameter, though the expanding jet cone is approximated as having a point source. The axial self-similarity parameters B and x_B are found through linear regression. Parameter B is an indicator of how rapidly centerline axial velocity decays with increasing axial distance from the jet. This formulation is more straightforward than the commonly used

$$\frac{u_c}{u_0} = \frac{C_1}{2}\frac{d}{x} \tag{3.21}$$

and avoids ambiguity regarding the effective axial distance from the physical jet outlet.

Xu and Antonia (2002) found that B values of approximately 5.6 and 6.5 correspond, respectively, to contraction nozzles and pipe flows. The unobstructed free jet in this study was found to have a B value of 5.8 ± 0.2 with a linear coefficient of determination $R^2 = 0.9907$ across eleven points, conforming to the value range for top-hat jets. In turbulent jets, axial velocity decays more rapidly than expected due to flow reversal at jet boundaries (Schneider, 1985). The momentum virtual origin x_B/d of the averaged free jet was found have a value of 0 ± 6. Due to the small diameter of the nozzle, $d = 6.35mm$, uncertainty in the experimental virtual origin was large in all analyses; therefore, these results are provided for comparison purposes only. Centerline axial velocities spanned $24 \leq x/d \leq 132$. The centerline reading at $x/d = 12$ was determined to potentially be within the zone of flow establishment and thus excluded. As has been noted by Lipari (2011), tank recirculation, which was minimized though nevertheless observed in this study, can reduce downstream momentum and artificially depress the B value.

Spanwise, axial velocity decays according to a Gaussian profile

$$\frac{u(\eta)}{u_c} = e^{-c\eta^2} \tag{3.22}$$

where $\eta = r/(x - x_S)$ (Wygnanski and Fiedler, 1969), (Hussein et al., 1994) and (Lipari, 2011). Parameter r is radial distance from centerline, and x_S is the spreading virtual origin. Because x_B and x_S are not based on the same mechanism, differences in virtual origin offset do not indicate error.

This notation, promoted in Lipari (2011), deviates from a common definition of a location parameter of similar usage $\eta_m = r/(c_1 x)$, where c_1 an experimental constant with the value 0.103 for circular jets, (Mih, 1989). Whereas linear regression of streamwise axial velocity decay yields a momentum virtual origin offset x_B, linear regression of spanwise axial velocity decay produces a spreading virtual origin offset x_S. A so-called radial halfwidth b or $r_{1/2}$ at which $u(\eta) = u_c/2$ serves as a spanwise characteristic length scale. Most entrainment occurs within $\pm 1.7b$ (Shlien, 1987). The halfwidth is occasionally defined as $u(b) = u_c/e$, though the definition $u(\eta) = u_c/2$ is used throughout this thesis (Agrawal and Prasad, 2002). In addition to η notation, ξ notation, where $\xi = r/r_{1/2}$, is encountered and provides for convenient normalization of spanwise velocity profiles (Agrawal and Prasad, 2003).

Typically, the spanwise profile of the axial velocity of a free jet is presumed to be Gaussian (Agrawal and Prasad, 2003). Figure 2.7 illustrates the folding of radial velocity profiles about the jet centerline and Gaussian fit, in this case for Section 3 of Configuration 1. The recirculation effect of the finite tank is visible as deviation from the folded mean for $|r/b| > 1$. The halfwidth spreading rate $S_{1/2}$ is otherwise defined as $\eta_{1/2}$

$$S_{1/2} = \eta_{1/2} = \frac{r_{1/2}}{x - x_s} \tag{3.23}$$

Typical values for c and $\eta_{1/2}$ are 76.5 and 0.095 for contraction jets and 90.2 and 0.086 for pipe flows (Xu and Antonia, 2002). Contraction jets, thus, decay axially and grow radially more rapidly than pipe flows. Due to conservation of momentum, halfwidth growth is necessarily accompanied by accelerated axial velocity decay. As a result of higher shear and enhanced entrainment, large-scale flow structures, such as vortical rings, occur closer to the outlet of contraction jets than for pipe flows (Liepmann, 1991). The averaged c and $\eta_{1/2}$ values for the free jet in this study are 81 ± 5 and 0.093 ± 0.003, and x_S/d is found to be -9 ± 14. These values result from linear regression of spanwise values over $84 \leq x/d \leq 120$. As is the case with x_B, uncertainty is great for all analyses of x_S and the value is given for comparison only. See Table 3.1 for a comparison of spread self-similarity parameters for all four measurement sections. Of the four measured sections, Section 1 was excluded from this average due to the poor radial resolution of the axial velocity profile. Parameters c and $\eta_{1/2}$ correspond to values expected of a top-hat jet, though somewhat elevated due to the extended nozzle length.

Deviation of experimental results from theory is often based on the frequently made assumption of some degree of isotropic flow (Kassab et al., 1996). Semi-isotrophy develops in the zone of established flow so that $\overline{v}^2/\overline{u}^2 = 0.6$, and spanwise axial velocity profiles in the zone of established flow collapse uniformly and are thus self-similar(Kassab et al., 1996). Figure 3.1a shows that although profiles

Table 3.1: Spreading self-similarity parameters of free jet

Section	x/d	c	$\eta_{1/2}$
1	48	86 ± 22	0.09 ± 0.01
2	84	82 ± 4	0.092 ± 0.002
3	120	81 ± 6	0.093 ± 0.004
4	132	81 ± 8	0.093 ± 0.004

collapse near the centerline, the mean radial velocity ratio is smaller than expected $0.2 < \overline{v}^2/\overline{u}^2 < 0.4$ and suggests that small semi-isotropic eddies occur primarily at the far radial edge and are overall diminished as vegetation is introduced. The ratio $\overline{w}^2/\overline{u}^2$, see Figure 3.1c, exhibits a similar shape. The effect of the simplification that $\overline{v}^2 = \overline{w}^2$ is especially frequently encountered in jet studies; however, as early as 1969, the failure of the isotropic models away from the streamwise centerline has been recognized (Wygnanski and Fiedler, 1969). Figures 3.1e and 3.1f demonstrate that generally $0.2 \leq \overline{w}^2/\overline{v}^2 \leq 0.5$ and $0.2 \leq \overline{w'w'}/\overline{v'v'} \leq 0.4$, respectively. As is shown in Figure 3.1b, curiously, $\overline{v'v'}$ is roughly equivalent to $\overline{u'u'}$ over the measurement plane.

3.4 Flow rate

Measurement of the jet flow rate yields a means to determine both nozzle outlet velocity and entrainment velocity. The general form for the volumetric flow rate of a circular jet is given by

$$Q = \int_0^\infty 2\pi r u \,\mathrm{d}r \tag{3.24}$$

The initial flow rate Q_0 is thus calculated from

$$Q_0 = A_0 u_{0bulk} = \frac{\pi}{4} d^2 \overline{u}_{0bulk} \tag{3.25}$$

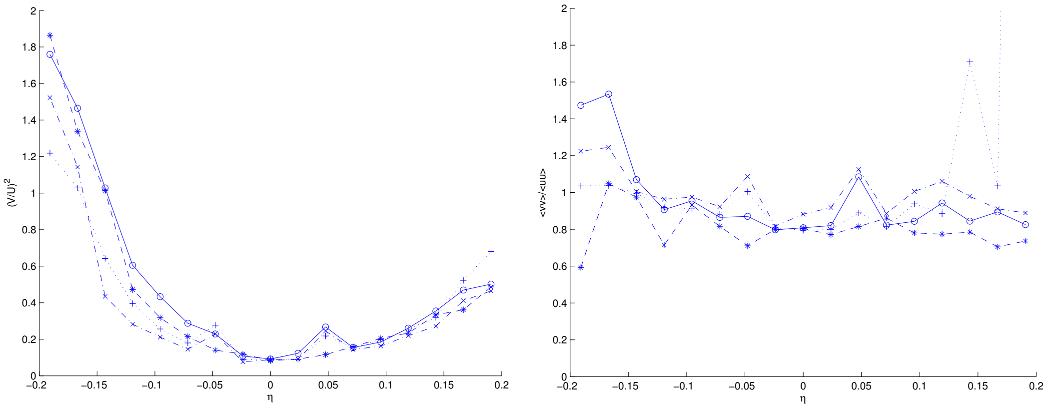

(a) $(\overline{v}/\overline{u})^2$ (b) $\overline{v'v'}/\overline{u'u'}$

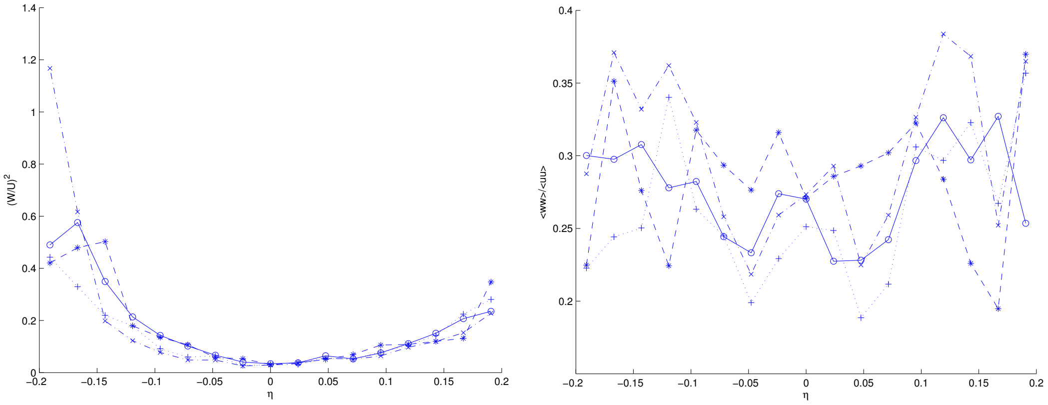

(c) $(\overline{w}/\overline{u})^2$ (d) $\overline{w'w'}/\overline{u'u'}$

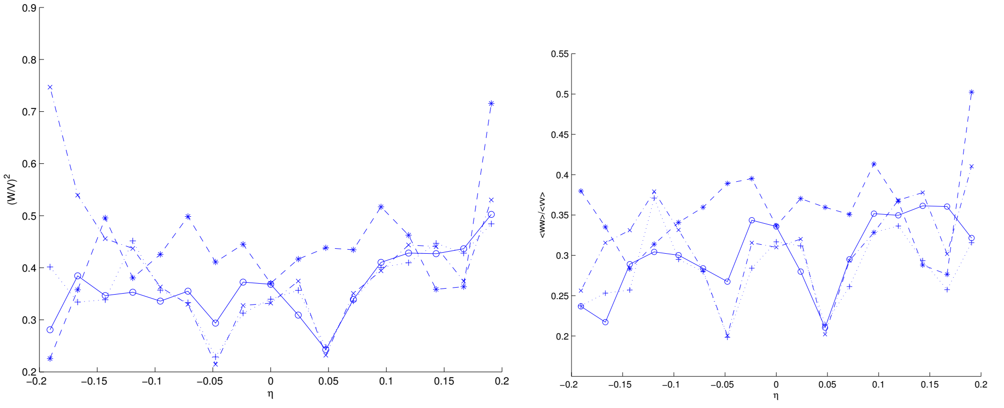

(e) $(\overline{w}/\overline{v})^2$ (f) $\overline{w'w'}/\overline{v'v'}$

Figure 3.1: Mean velocity and normal Reynolds stress ratios at Section 4

Configuration − free jet($*$) 1(◯) 2($+$) 3($\times$)

where A_0 is the area of the outlet nozzle.

The entrainment hypothesis put forth by Sir Geoffrey Taylor predicts that ambient fluid at the shear interface with the radially expanding jet is first drawn in toward the jet centerline at an entrainment velocity $\overline{v_e}$

$$\overline{v_e} = \alpha \overline{u_c} \tag{3.26}$$

that is directly proportion by a certain factor, the entrainment coefficient α, to a corresponding axial velocity along the jet centerline

$$\alpha = \frac{c}{b\overline{u_c}} \tag{3.27}$$

where b is halfwidth and c is an experimental constant (Ricou and Spalding, 1961).

As a result, volumetric flux can be expressed in terms of mean centerline axial velocity and characteristic turbulent jet self-similarity properties

$$\frac{dQ}{dx} = 2\pi c = 2\pi\alpha b\overline{u_c} \tag{3.28}$$

(Turner, 1986). Table 3.2 demonstrates that $0.0551 \leq \alpha \leq 0.0638$ over the free jet range and is calculated from Equation 3.28. A commonly accepted value for α is 0.057(Falcone, 2003). An alternate formulation of the entrainment rate $\frac{dQ}{dx}$ is given in

$$\frac{dQ}{dx} = C_3 \frac{Q_0}{d} \tag{3.29}$$

(Crow and Champagne, 1971). Typically, the value of C_3 falls within the range $0.185 \leq C_3 \leq 0.34$ for the zone of established flow (Falcone, 2003).

Table 3.2: Numerically integrated volume flux and entrainment coefficient for free jet

Section	x/d	Q/Q_0	α
1	48	14.49	0.0638
2	84	26.37	0.0633
3	120	30.32	0.0574
4	132	36.00	0.0551

Applying Equation 3.28 and calculating volumetric flow derivatives across spanwise sections using a central-difference method, the free jet was found to have an average $\alpha = 0.0575$ over $84 \leq x/d \leq 132$, due to radial resolution at sections 1 and 2. A closer inspection of α calculated per section, using the same method, see Table 3.2, reveals a gradual shift towards lower entrainment velocities relative to centerline axial velocities. The mechanism for this decay is unclear and suggests that either method of computation is flawed or that the jet may not be truly self-similar. It is probable the axial resolution of the four sections is insufficient to accurately determine α. Entrainment velocities are related to α, by definition, and thus also exhibit streamwise decay in obstructed flow.

3.5 Momentum

In general, momentum for a circular jet is fundamentally defined by

$$M = Qu = \int_0^\infty 2\pi r u^2 \, \mathrm{d}r \qquad (3.30)$$

For an ideal jet entering an infinite domain of quiescent ambient fluid, equations 3.18 and 3.19 are integrated twice, with third-order and higher terms neglected, to produce

$$M = 2\pi\rho \int_0^\infty \left(\overline{u}^2 + \overline{u'^2} - \frac{\overline{v'^2} + \overline{w'^2}}{2} \right) r \, \mathrm{d}r \tag{3.31}$$

Equation 3.31 for axial momentum, which can be decomposed into mean and turbulent momentum contributions

$$\frac{\overline{M}}{M_0} \approx 8\left(B\eta_{1/2}\right)^2 \int_0^\infty \left(\frac{\overline{u}}{u_0}\right)^2 \xi \, \mathrm{d}\xi = 2.885\left(B\eta_{1/2}\right)^2 \tag{3.32}$$

$$\frac{M'}{M_0} \approx 8B^2 \int_0^\infty \left(f_{\overline{u'^2}} - \frac{f_{\overline{v'^2}} + f_{\overline{w'^2}}}{2} \right) \eta \, \mathrm{d}\eta \tag{3.33}$$

respectively, where $f_{\overline{u'^2}}$ represents axial Reynolds stress normalized to mean axial centerline velocity (Hussein et al., 1994), (Weisgraber and Liepmann, 1998), (Papanicolaou and List, 1988) and (Lipari, 2011). Turbulent contribution in Equation 3.33 are normalized to nozzle axial velocity. Equation 3.31 takes into account the momentum-based characterization of the jet cone through parameter B, as well as the spreading analysis parameter $\eta_{1/2}$. Based on the top-hat jet profile, i.e., $u_0 = \overline{u_0}_{bulk}$, momumentum at the nozzle for an axisymmetric jet is given by

$$M_0 \approx \overline{M_0} = \pi\rho(\frac{d}{2})^2\overline{u_0}^2 \tag{3.34}$$

(Schneider, 1985).

Assumptions of purely quiescent ambient fluid, such as $u_\infty = 0$ and $\frac{dp_\infty}{dx} = 0$, become problematic when tank recirculation or encroachment of the jet cone on tank walls occurs. Terms that had been previously neglected due to this assumption may now contribute to sapping momentum at axial distances far from the outlet nozzle (Hussein et al., 1994). Such jets exhibit a downstream failure to conserve initial momentum, $\frac{M}{M_0} = \frac{\overline{M}+M'}{M_0} < 1$. Vortex interaction occurs as free shear layers encounter wall shear layers (Shinneeb et al., 2011).

For the free jet over , this study found $\frac{\overline{M}}{M_0} = 0.83 \pm 0.04$, $\frac{M'}{M_0} = 0.22 \pm 0.06$ and $\frac{M}{M_0} = \frac{\overline{M}+M'}{M_0} = 1.05 \pm 0.07$. These values result from linear regression of spanwise values over $84 \leq x/d \leq 132$. For various studies reviewed, $\frac{\overline{M}}{M_0}$ generally varies from 0.82 to 0.98 (Lipari, 2011). Two experiments reviewed in the journal article demonstrated $\frac{M'}{M_0}$ values of 0.07 and 0.09. As a result, the present study predicts a relatively low mean momentum ratio and a relatively high turbulent momentum ratio, though the sum of these ratios indicate momentum conservation and thus validation of setup, measurement scheme and analysis.

Despite efforts to eliminate recirculation and limit recording time to the downstream extent of the free jet, measurements realize a small recirculation current that unevenly affects axial velocities across the spanwise profile, most noticeably at extreme radial measurement stations. Attempts to measure and adjust for the recirculation velocity magnitude could not be applied uniformly for all speeds, sections and configurations.

Considering a confined jet within a chamber, rather than a free jet in an infinitely large, quiescent ambient fluid, tank recirculation accelerates centerline momentum decay. The ratio of expected retained momentum is expressed by

$$\frac{M}{M_0} = \left[1 + \frac{16}{\pi B^2}\left(\frac{x}{d}\right)^2 \frac{A_0}{A_R}\right]^{-1} \tag{3.35}$$

where B is the momentum self-similarity parameter, A_0 is the area of the jet outlet and A_R is the cross-sectional area of the chamber (Hussein et al., 1994).

For the present setup, this ratio is essentially unity; therefore, any failure of in-plane momentum conservation would not be due to the confined cross-sectional area

Table 3.3: Axial conservation of momentum by self-similarity parameter for free jet

Section	x/d	$\overline{M}/M_0$	M'/M_0	M/M_0
1	48	0.8 ± 0.2	0.15 ± 0.07	1.0 ± 0.2
2	84	0.82 ± 0.05	0.3 ± 0.1	1.12 ± 0.09
3	120	0.83 ± 0.06	0.17 ± 0.02	1.00 ± 0.07
4	132	0.83 ± 0.07	0.185 ± 0.009	1.02 ± 0.08

Table 3.4: Numerically integrated axial conservation of momentum for free jet

Section	x/d	$\overline{M}/M_0$	M'/M_0	M/M_0
1	48	0.838	0.298	1.135
2	84	0.945	0.443	1.388
3	120	0.759	0.265	1.024
4	132	0.818	0.208	1.026

of the tank.

Applying equations 3.32 and 3.33, conservation of momentum for the free jet is summarized in Table 3.3. Mean momentum is a function of both the axial decay coefficient of mean axial velocity and radial speading coefficients. Turbulent momentum, but contrast, is computed with section-specific mean Reynolds stress and mean axial centerline velocity. Conservation of momentum, however, can aslo be calculated directly by applying Equation 3.31 through numerical integration,. The resulting direct values for conservation of momentum—see Table 3.4—support values derived from self-similarity parameters. Results for the free jet configuration confirm published values and validate the method of analysis for further application to obstructed flow.

3.6 Energy

Expressed in vector form, equations 3.2 – 3.4 yield

$$\frac{\mathrm{D}\mathbf{u}}{\mathrm{D}t} = \frac{\partial \mathbf{u}}{\partial t} + \left(\mathbf{u} \cdot \nabla\right) \mathbf{u} - \frac{u_\theta^2}{r}\hat{r} + \frac{u_r u_\theta}{r}\hat{\theta} \quad = \quad -\frac{1}{\rho}\nabla p + \epsilon \tag{3.36}$$

The dissipative term ϵ is expressed as a closure term. Derivation of an expression for turbulent kinetic energy, however, is more straightforward with Einstein notion

$$u_j \frac{\partial u_i}{\partial x_j} - \frac{u_\theta^2}{r}\hat{r} + \frac{u_r u_\theta}{r}\hat{\theta} \quad = \quad -\frac{1}{\rho}\frac{\partial p}{\partial x_i} + \epsilon \tag{3.37}$$

where a further assumption of steady flow eliminates $\frac{\partial}{\partial t}$.

These equations can be manipulated, see the Appendix A for detailed derivation, to produce an energy balance for turbulent kinetic energy

$$\begin{aligned}
&\left[\left(\overline{u}\frac{\partial}{\partial x} + \overline{v}\frac{\partial}{\partial r}\right)\overline{q}\right]_{\text{advection}} + \\
&\left[2\left(\frac{\partial \overline{u}}{\partial r}\overline{u'u'} + \frac{\partial \overline{u}}{\partial x}\overline{v'u'} + \frac{\partial \overline{v}}{\partial r}\overline{v'v'} + \frac{\partial \overline{v}}{\partial x}\overline{v'u'} + \frac{\partial \overline{w}}{\partial x}\overline{w'u'} + \frac{\partial \overline{w}}{\partial r}\overline{w'v'}\right)\right]_{\text{production}} + \\
&\left[\frac{\partial \overline{u'q}}{\partial x} + \frac{1}{r}\frac{\partial\left(r\overline{v'q}\right)}{\partial r}\right]_{\text{turbulence transport}} = \left[-\frac{2}{\rho}\left(\frac{\partial \overline{u'p}}{\partial x} + \frac{\partial \overline{v'p}}{\partial r}\right)\right]_{\text{pressure transport}} + \\
&\left[\epsilon\right]_{\text{dissipation}}
\end{aligned} \tag{3.38}$$

where $q = u'u' + v'v' + w'w'$ (Raupach, 1992). Following a similar procedure, and multiplying through by mean velocity, rather than turbulent fluctuation, at Equation A.5 in Appendix A produces an analogous energy balance for mean kinetic energy.

Advection represents the movement of turbulent kinetic energy by mean velocity. By contrast, the turbulence and pressure transport terms represent turbulent kinetic energy moved by turbulence and pressure gradients, respectively. The production term—also occurring, though negated, in the energy balance for mean kinetic energy—represents the conversion of mean kinetic energy to turbulent kinetic energy as the Reynolds stresses interact with mean shear (Kundu and Cohen, 2008). Advection, production and turbulent transport—these terms may be directly calculated. The magnitude of the pressure transport term, however, is often determined as the closing term in the balance of the energy equation (Ramaprian and Chandrasekhara, 1985). Free-jet values across each are included in Chapter 4.4.

The remaining term, the closure dissipation term, represents the final conversion of turbulent kinetic energy into heat on the molecular level, given explicitly by

$$\epsilon = \nu \left(\overline{\frac{\partial u'_i}{\partial x_j} \frac{\partial u'_i}{\partial x_j}} + \overline{\frac{\partial u'_i}{\partial x_j} \frac{\partial u'_j}{\partial x_i}} \right) \tag{3.39}$$

(Lipari, 2011).

This expression is computationally cumbersome and rarely determined instantaneously (Elsner and Elsner, 1996). Instead, it is general practice to employ an FFT to compute spectral energy density

$$S_{uu}(f) = \frac{2}{N^2 \Delta f} |X_k|^2 \tag{3.40}$$

where N is the number of samples in the original record, Δf is the sampling frequency divided by N, and X_k is the amplitude of the velocity spectrum output from the FFT. In the present study, the complete record at each measurement station was split into realizations of 1024 samples, the velocity spectrum was folded about its center, and the resulting energy density spectra were averaged for smoothing. The final spectrum was scaled for variance preservation.

From an energy perspective, the axial energy density spectrum, $S_{uu}(f)$, is given by

$$S_{uu}(f) = \frac{18}{55} A \epsilon^{\frac{2}{3}} \left(\frac{\overline{u}}{2\pi} \right)^{\frac{2}{3}} f^{-\frac{5}{3}} \tag{3.41}$$

where A is an experimental constant approximately equal to 1.5, ϵ is the rate of turbulent dissipation and f is the shedding frequency (Nepf, 1999). Expressed as a function of wavenumber k, where $k = \frac{2\pi}{\overline{u}} f$, this expression is alternatively given by Kolmogorov's $K^{-5/3}$ Law

$$S_{uu}(k) = \frac{18}{55} A \epsilon^{\frac{2}{3}} k^{-\frac{5}{3}} \tag{3.42}$$

(Kundu and Cohen, 2008). To compute dissipation rate, ϵ is isolated and is the mean product of the spectral energy density and wavenumber

$$\epsilon = \overline{\left(\frac{S_{uu}(k) k^{\frac{5}{3}}}{\frac{18}{55} A} \right)^{\frac{3}{2}}} \tag{3.43}$$

Although dissipation is a viscous phenomenon, equations 3.42 and 3.43 are valid over the so-called inertial subrange, in which energetic large-scale eddies break apart through inertial forces—vortex streching—into small eddies that dissipate through viscous heat generation (Kundu and Cohen, 2008). This region may readily be determined by a -5/3 slope on a log-log plot of wavenumber to spectral energy density, see Figure 3.2. The eddies occurring at smaller wavenumbers are anisotropic because they are advected by mean gradients. By contrast, the eddies at higher wavenumbers are nearly isotropic and in a state of viscous dissipation. The width of the inertial subrange is a function of Reynolds number and, as will demonstrated in Chapter 4.4, obstacles to flow.

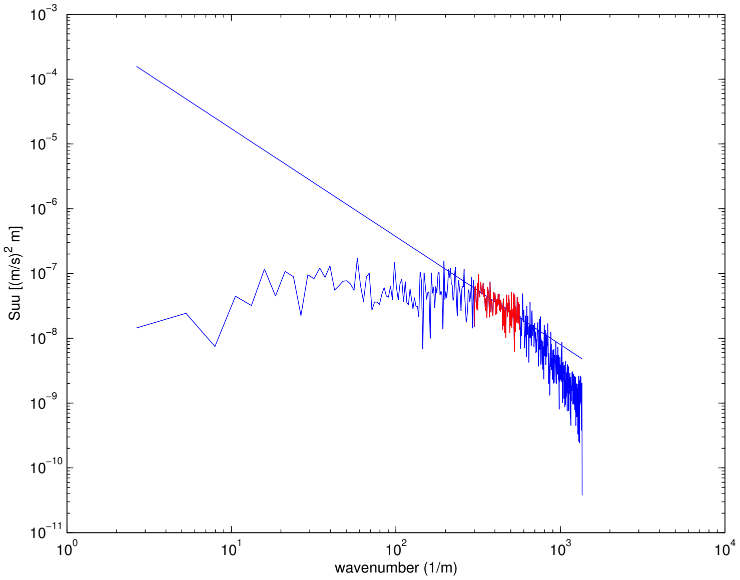

Figure 3.2: Energy density spectrum of axial velocity at Section 4 centerline of the free jet

$k^{-5/3}$ indicated by a straight line and inertial subrange in red

4. VEGETATION

4.1 Types of vegetation

Having validated the free jet over the four radial sections and five experimental speeds, the free jet is obstructed by arrays of simulated vertical rigid vegetation. Three configurations are selected so that the free jet impinges upon plant arrays at various stages of jet development, see Figure 2.3. Configuration 1 allows the jet to develop full self-similarity before entering vegetation; Configuration 2 allows study of impingement within the early zone of established flow; and Configuration 3 populates the full zone of flow establishment with vegetation.

The selected type of vegetation, rigid and emergent staggered vegetation, is but one of several commonly studied wetland plants. Many researchers have investigated *Spartina alterniflora* and similar rigid vegetation, both actual and simulated, under emergent and submerged conditions, see Table 2.2. Under these conditions, it is possible to investigate diffusion and turbulent mixing as agents of nutrient exchange and plant-induced drag, as a means of reducing storm surge. Additionally, significant research exists on drag induced by flexible submerged vegetation (Gambi et al., 1990).

In one study involving live *Spartina anglica* mounted in a recirculating flume, Pye et al. (1995) demonstrated that the presence of saltwater vegetation influences the concentration of suspended sediment, settling velocity and the deposition rate of cohesive sediments by means of flow shear stress and turbulence. In a related study, submerged flexible *Zostera marina* was found to extract momentum from the mean flow through drag, and the density of the vegetation was directly related to turbulent intensity, shear stress as canopy level and a reduction of the mean flow velocity, each a property relevant to sediment suspension and nutrient distribution (Gambi et al., 1990). Neumeier (2004) has thus suggested that *Spartina alterniflora* is better suited to erosion protection from storm surge than to increased local sediment deposition under normal conditions.

For sparsely vegetated arrays where $ad < 0.1$, see Equation 2.3, the cumulative effects of multiple stem wakes are neglected, and only the wake structure of the closest upstream stem is presumed to have significant effects on flow characteristics at any measurement location (Nepf et al., 1997). The present study demonstrates, however, that sufficiently high-frequency ADV measurements can capture the combined effects of distant upstream vegetation on mean and turbulent jet flow parameters, thus providing a means of quantitatively studying the effects of multiple stem wakes in field or laboratory settings.

Measurements across the vegetated domain are taken for the same approximate duration and at the same 64 measurement stations across the same centerline and four radial sections at the same five speeds for each of the three vegetated configurations, as with the free jet, resulting in more than forty hours of $50Hz$ 3-D ADV records. Speeds are found to collapse for plant configurations and are the primary means of determining experimental error, see Chapter 2.5. The spacing of centerline measurement stations and axial distance of radial sections optimize ADV placement with respect to plant array introduction.

In addition to recording multiple stem wake interactions, several stations are in the immediate wake of individual stems, as well as immediately in front of stems, thus permitting the future detailed study of both downstream and upstream effects of isolated stems, respectively. The scope of the present study is largely limited to cumulative wake interaction, though single-wake effects are clearly visible in plotted data and warrant further study.

4.2 Plant location and vortex shedding

Derived properties—such as streamwise self-similarity parameters, conservation of momentum and turbulent kinetic energy balance—provide substantial information about the overall domain under the influence of various vegetated configurations. They, by definition, depict multiple wake effects. In order to determine the effects of individual stem wakes, against a background of multiple wake effects, it is necessary to look directly at individual measurement station records.

Figures B.1 to B.24 in Appendix B indicate that radial and tangential mean velocities and all Reynolds stresses and turbulent triple products increase and axial mean velocity decreases behind plant stems. Directly behind a stem—within a recirculation zone extending downstream up to approximately one diameter and separated from the mean flow by a free shear layer—the mean axial velocity is negative, thus resulting in a gradual vertical spiral that displaces slow fluid from the base of the plant stem to the top of the plant canopy, if submerged, or the free surface, if emergent (Stoesser et al., 2009), (Liu et al., 2008) and (Sadeque et al., 2008). Due to probe dimensions, however, direct measurement within this zone was not achieved. Although mean axial velocity is clearly converted to radial velocity, Reynolds stresses and turbulent triple products, there is insufficient evidence—only a slight increases in $\overline{w}$—to confirm the observation of vertical fluid displacement (Stoesser et al., 2009).

In the radial direction, these velocities result both in the expansion of the jet cone and the manifestation of vortical eddies primarily within the axial-radial plane. Tangential triple products, however, demonstrate a pronounced increase behind stems.

The mode of vortices shed off an isolated cylinder is a function of the Reynolds number (Balachandar and Parker, 2002). An isolated cylinder, a widely studied configuration, is essentially an element within an array with assumed infinite stem spacing. In laminar flow, a symmetric wake detaches from the cylinder, whereas in turbulent flow, cylinders develop an alternately shedding horseshoe vortex, known as the von Karman vortex street (Balachandar and Parker, 2002) and (Luo et al., 1996). A study by Guillaume and LaRue (1999) investigated configurations of two, three and four side-by-side cylinders and found that although cases with two or three cylinders experienced multiple modes of vortex shedding, the four-cylinder case only produced a single, multiple wake shedding mode. Applied to the present study, this finding suggests a single, collective shedding mode for the first row, if not for each subsequent row.

As a cylinder transitions from complete emergence to increasing degrees of submergence, the horseshoe vortex comprising the wake bubble decreases in size (Sadeque et al., 2008). In the first rows of a staggered array, the alternate vortex shedding of each cylinder may be considered independent for low Reynolds numbers (Abd-Rabbo and Weaver, 1986). In turbulent flow, von Karman vortex streets interfere, especially in dense arrays, causing an increase in downstream dynamic pressure and an accompanying increase in spanwise velocity and decrease in streamwise velocity as fluid seeks to circumvent the vegetated array, which is consistent with the findings of the present study (Braun and Kudriavtsev, 1995). Although this study varies neither stem spacing nor diameters, Balachandar and Parker (2002) found that the length scale of vortex shedding is defined by spacing, not stem diameter.

4.3 Self-similarity and momentum

The arrays of simulated vegetation are designed to imitate the rigid stems of sparse salt marsh *Spartina alterniflora*, thereby preserving the characteristic shape of jet flow—and the convenient ability to approximate self-similarity parameters—without deviating significantly from realistic field conditions, thus allowing an analysis of the promoted shore protective properties of marsh vegetation. By directly applying the theory and means of analysis put forth in Chapter 3.2, one computes vegetated flow self-similarity parameters describing axial or streamwise decay, as well as radial or spanwise spreading. For simplicity and economy, no especial designation differentiates true free jet self-similarity parameters and vegetated flow self-similarity parameters. Figures in Appendix B record mean and RMS values of mean velocity, Reynolds stresses and triple products for all collapsed cross sections; these figures are provided for reference.

Applying Equation 3.20, axial decay along the jet centerline is measured with the same assumption of linearity with respect to axial distance from the jet outlet, see figures 4.1 and 4.2. The undulating streamwise profile for Configuration 3 in figures 4.1b and 4.2d neatly indicate the positioning and effect of plants stem wakes on axial velocity for the fully vegetated flow domain. The resulting axial decay coefficient B steadily drops as the point of array impingement nears the jet outlet, physically manifesting as slower downstream axial centerline velocities, see Table 4.1. Although the coefficient of determination R^2 is above 0.95 across eleven points for all four section-averaged configurations, determination of the momentum virtual origin x_B is subject to the same deficiency as for the free jet, namely the relatively small nozzle diameter, and thus of no apparent practical use. As with the free jet, averaged centerline axial velocities spanned $24 \leq x/d \leq 132$, which is wholly within the self-similar range.

Likewise, spanwise spreading is determined by Gaussian fitting radial folded profiles to Equation 3.22, resulting in Table 4.2. As introduced vegetation nears the jet nozzle, the shape of the profile widens as c decreases, and the radial displacement of the halfwidth from the axial centerline increases, indicated by an increase in $\eta_{1/2}$. Again, there is no definitive significance of the spreading virtual origin x_S. Figure

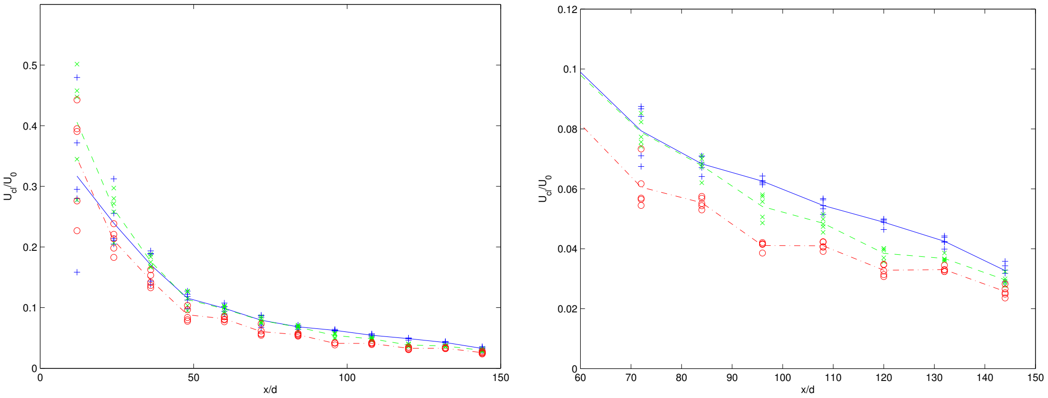

(a) Full range

Configuration − 1(+) 2(×) 3(◯)

(b) Zone of established flow

Configuration − 1(+) 2(×) 3(◯)

Figure 4.1: Axial streamwise velocity decay

Table 4.1: Section-averaged self-similar momentum parameters of vegetated jet

Configuration	B	x_B/d	R^2
Free jet	5.8 ± 0.2	0 ± 6	0.991
1	5.1 ± 0.2	7 ± 4	0.953
2	4.2 ± 0.2	14 ± 2	0.973
3	3.7 ± 0.1	10 ± 2	0.967

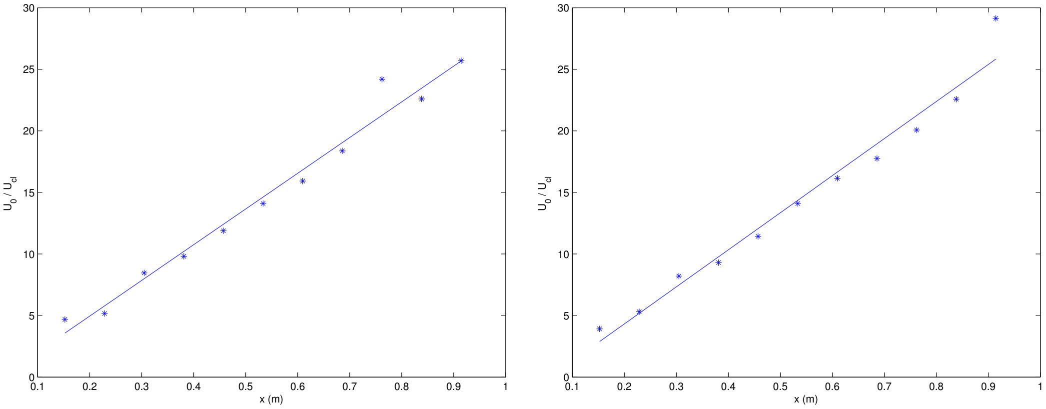

(a) Free jet (b) Configuration 1

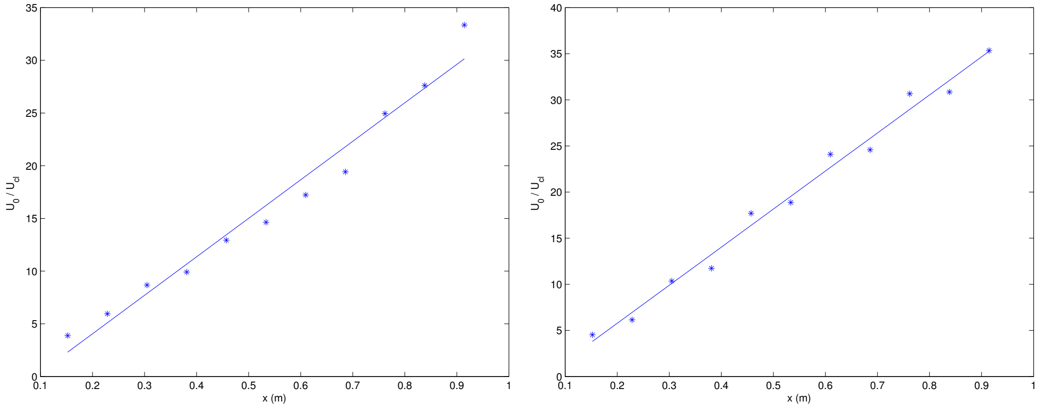

(c) Configuration 2 (d) Configuration 3

Figure 4.2: Streamwise linear regression of mean axial velocity

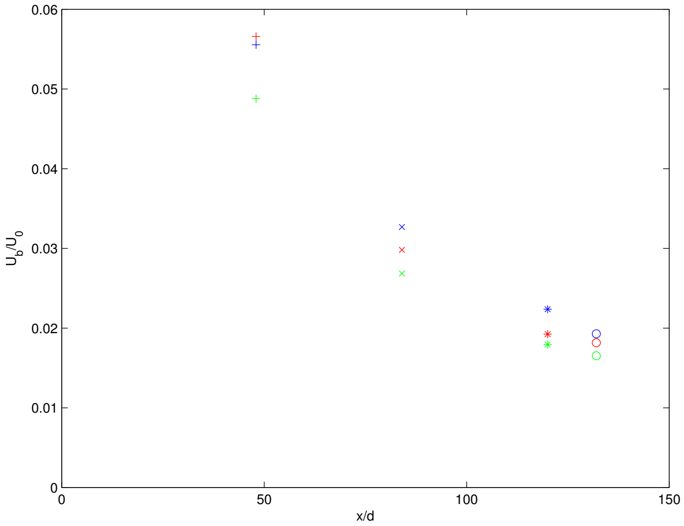

Figure 4.3: Axial velocity halfwidth

Section – 1(+) 2(×) 3(∗) 4(◯)

Configuration – 1(blue) 2(red) 3(green)

4.3 displays axial halfwidth velocity; as expected, velocities are reduced as vegetation is introduced. These values result from linear regression of spanwise values over $84 \leq x/d \leq 120$; Section 1 is excluded from the average due to insufficient radial resolution. Table 4.3 and Figure 4.4 present spreading self-similarity parameters for each section for all configurations. In every case, the Gaussian fit of Section 1 profiles is accompanied by high experimental error.

Plotting calculated collapsed radial sections by configuration normalized to nozzle velocity, see Figure 4.5, reveals that the increased presence of vegetation produces a shallower, broader velocity profile. The radial spreading Gaussian fit for Configuration 2 results in higher experimental error across all sections and propagates through all derived parameters. In general, however, the collapsing of speeds enhanced parameter determination. The slight overall deviation and elevated uncertainty of Configuration 2 from the general decreasing or increasing trend of parameters from free

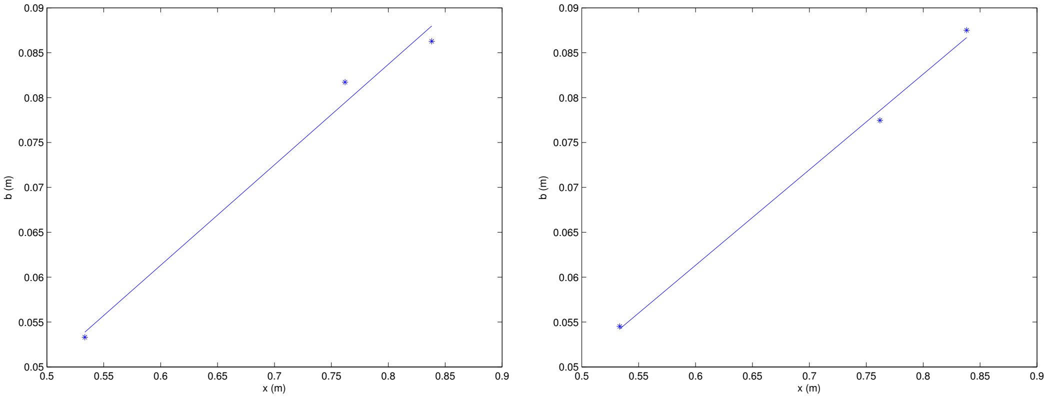

(a) Free jet (b) Configuration 1

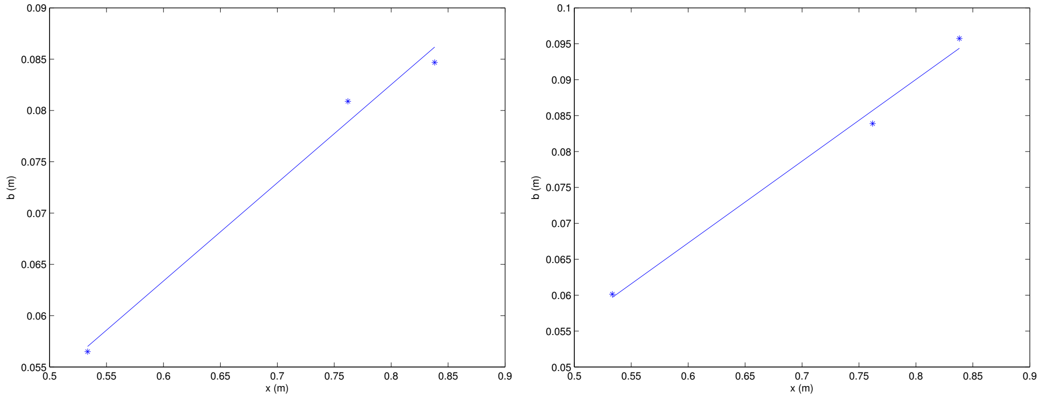

(c) Configuration 2 (d) Configuration 3

Figure 4.4: Spanwise linear regression of mean axial velocity

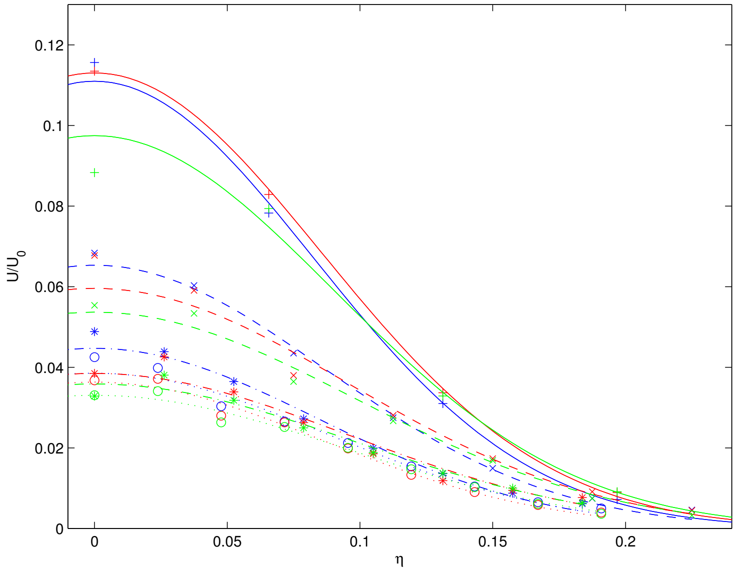

Figure 4.5: Axial velocity profiles normalized to nozzle velocity

Section – 1(+ solid) 2(× dashed) 3(∗ dash dot) 4(◯ dot)

Configuration – 1(blue) 2(red) 3(green)

jet to Configuration 3 may be indicative of subtle changes caused the intermediate point of flow impingement upon vegetation across the five experimental speeds.

To facilitate determination of spreading self-similarity parameters through Gaussian approximation, edge effects necessitated the occasional bilateral truncation of extreme radial stations for select profiles. By universally applying an algorithm that detects unrealistically high normalized RMS edge values, as compared to neighboring profile velocities or stresses and can be seen in figures B.11b and B.14b, these aberrant reading values are eliminated during Gaussian fitting to ensure a proper representative Gaussian curve. In all other cases, these values are retained.

Vegetated flow axial decay self-similarity parameters indicate accelerated centerline velocity decay, and vegetated flow spreading parameters indicate a broader radial zone of fluid entrainment. Equation 3.32 demonstrates that the product of

Table 4.2: Section-averaged self-similar spreading parameters of vegetated jet

Configuration	c	$\eta_{1/2}$	x_S/d	R^2
Free jet	85 ± 5	0.093 ± 0.003	-9 ± 14	—
1	79 ± 3	0.094 ± 0.002	1 ± 6	0.984
2	70 ± 6	0.100 ± 0.005	-29 ± 30	0.895
3	64 ± 4	0.104 ± 0.003	-9 ± 12	0.980

Table 4.3: Self-similar spreading parameters of vegetated jet

Section	x/d	c	$\eta_{1/2}$
Free Jet			
1	48	86 ± 22	0.09 ± 0.01
2	84	82 ± 4	0.092 ± 0.002
3	120	81 ± 6	0.093 ± 0.004
4	132	81 ± 8	0.093 ± 0.004
Configuration 1			
1	48	99 ± 14	0.084 ± 0.007
2	84	83 ± 4	0.092 ± 0.002
3	120	77 ± 2	0.095 ± 0.001
4	132	76 ± 2	0.095 ± 0.002
Configuration 2			
1	48	58 ± 16	0.11 ± 0.02
2	84	66 ± 9	0.103 ± 0.007
3	120	71 ± 6	0.099 ± 0.004
4	132	73 ± 6	0.098 ± 0.004
Configuration 3			
1	48	67 ± 12	0.10 ± 0.01
2	84	64 ± 4	0.104 ± 0.004
3	120	64 ± 4	0.105 ± 0.003
4	132	64 ± 5	0.105 ± 0.004

the axial parameter B and radial parameter $\eta_{1/2}$ is proportional to mean axial jet momentum. Applying the same technique to jet flow through vegetated arrays to yield a vegetated flow self-similar conservation of momentum produces Table 4.4 for section-averaged configurations and Table 4.6 for each section of each configuration.

The values for vegetated flow conservation of axial momentum suggest a loss of momentum from $M/M_0 = 1.05 \pm 0.07$ for the free jet configuration to $M/M_0 = 0.54 \pm 0.05$ for the fully vegetated configuration. This formulation of M/M_0 relies on Equation 3.32 and by extension B, which measures the total axial decay along the jet centerline without accounting for a potentially abrupt change in velocity upon transitioning from free jet to vegetated flow. Spanwise profiles, and thus self-similarity parameters, are independent of this effective smoothing effect. Due to the low uncertainty of B and $\eta_{1/2}$ in tables 4.1 and 4.2 along the centerline, the derived M/M_0 of Table 4.4 describes an actual deficiency of momentum. It is prudent, nevertheless, to consider any vegetated B and property derived from B as pertaining to vegetated flow and a result of smoothing axial decay, despite high linear correlation. Table 4.6 contains momentum calulations for each section and configuration.

A numerical integration of radial profiles from vegetation configurations may either support the M/M_0 computation based on vegetated flow self-similarity parameters or indicate failure of the vegetated flow self-similarity assumption by signaling an abrupt change in conservation of momentum along the jet centerline of each vegetated configuration. Tables 4.5 and 4.7 represent mean, turbulent and total momentum calculated by numerically integrating RMS velocities spanwise at each radial section in accordance with Equation 3.31.

In all instances, mean and turbulent numerically integrated momentum components exceed momentum components determined through self similarity analysis, though are generally within experimental error, see Figure 4.6. No abrupt

Table 4.4: Section-averaged self-similar conservation of axial momentum for vegetated jet

Configuration	$\overline{M}/M_0$	M'/M_0	M/M_0
Free jet	0.83 ± 0.04	0.28 ± 0.06	1.05 ± 0.07
1	0.67 ± 0.05	0.17 ± 0.04	0.85 ± 0.08
2	0.51 ± 0.04	0.3 ± 0.2	0.8 ± 0.2
3	0.44 ± 0.04	0.10 ± 0.03	0.54 ± 0.05

Table 4.5: Section-averaged numerically integrated conservation of axial momentum and entrainment coefficient for vegetated jet

Configuration	$\overline{M}/M_0$	M'/M_0	M/M_0	α
Free jet	0.9 ± 0.3	0.3 ± 0.1	1.2 ± 0.4	0.0575
1	0.8 ± 0.3	0.3 ± 0.1	1.1 ± 0.4	0.0566
2	0.8 ± 0.3	0.52 ± 0.07	1.3 ± 0.3	0.0580
3	0.7 ± 0.3	0.16 ± 0.05	0.9 ± 0.3	0.0631

change in momentum across the sections for a given configuration is clearly observed, though low axial resolution prevents further exploring this potentially interesting phenomenon. Conservation of momentum ratios determined for both vegetated flow self-similarity parameters generally follow the trend of decreasing with respect to increasing axial distance; the corresponding values for numerically integrated configurations, to an extent, do as well.

In the far zone of established flow, both methods used to determine momentum indicate that turbulence has either reduced or lost the capacity to transport momentum, as would be expected of the small, isotropic eddies that dominate high-wavenumber viscous dissipation. Early in the zone of established flow, the momentum calculated from numerical integration is noticeably greater than unity and momentum calculated by the self-similarity method; in Figure 4.6c, numerically integrated momentum greatly exceeds initial momentum over sections 1 and 2. Because in-plane momentum cannot be gained, only advected out of plane or dissipated, this excess momentum is likely the result of insufficient radial resolution between measurement stations. Self-similarity parameters, by contrast, in Figure 4.6a indicate a rising portion of momentum advected by the mean flow for the free jet and Configuration 1, which would be expected in a stretch of free jet where large, energetic eddies are anisotropic and capable of transporting momentum. Vegetated configurations 2 and 3 enter vegetation early and thus lose momentum through advection or dissipation.

Table 4.8 indicates that the entrainment coefficient α likewise decays along the streamwise axis for each configuration, though sections 3 and 4 of the vegetated configurations suggest increased stability of the parameter in the zone of established flow. The axial decay of α and the instance of multiple total numerically integrated momentum ratios exceeding unity suggest that the radial resolution, $\Delta r = 2\ cm$, may be insufficient, though this spacing was chosen to avoid overlap of the ADV sampling volume.

Although numerically calculated conservation of momentum ratios recommend caution applying vegetated flow self-similar parameters to derived properties of vegetated configurations, a combination of increased radial resolution and increased number of sections—a measure of axial resolution with regard to jet impingement upon vegetated arrays—may reconcile the current discrepancy.

4.4 Energy

An energy balance for turbulent kinetic energy was presented in Chapter 3.6 and is presumed to apply to obstructed flow as well. Equation A.18 applies to vegetated configurations without adaptation or approximation. The self-similarity analysis of the various vegetated arrays demonstrated that as progressively more vegetation

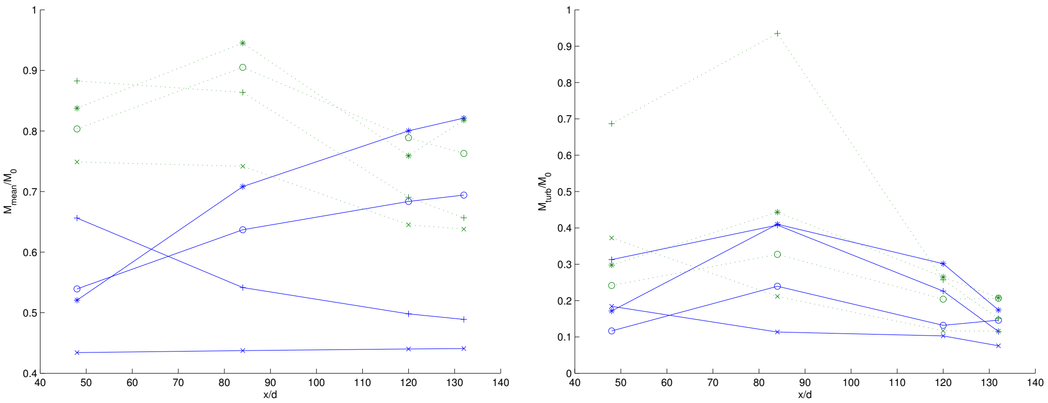

(a) Mean momentum (b) Turbulent momentum

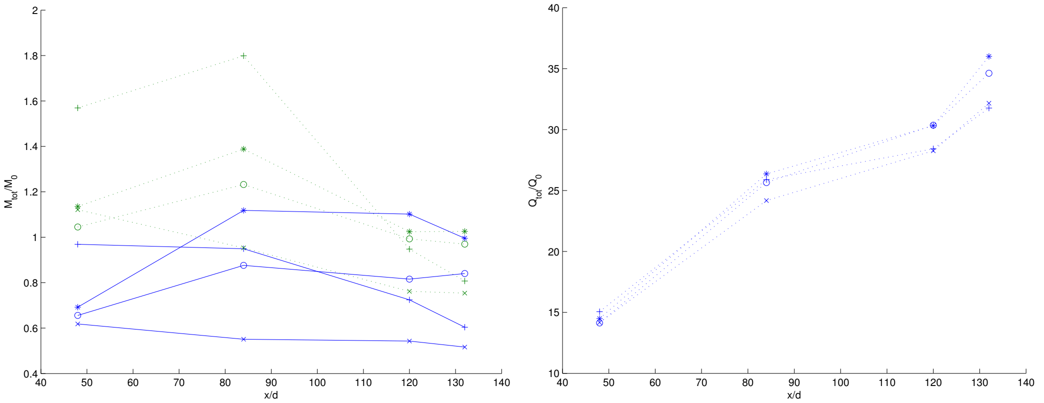

(c) Total momentum (d) Volume flux

Figure 4.6: Streamwise conservation of momentum

Configuration − free jet($*$) 1(◯) 2(+) 3(×)

self similarity(−) numericallyintegrated($\cdots$)

Table 4.6: Self-similar axial conservation of momentum for vegetated jet

Section	x/d	$\overline{M}/M_0$	M'/M_0	M/M_0
Free jet				
1	48	0.8 ± 0.2	0.15 ± 0.07	1.0 ± 0.2
2	84	0.82 ± 0.05	0.3 ± 0.1	1.12 ± 0.09
3	120	0.83 ± 0.06	0.17 ± 0.02	1.00 ± 0.07
4	132	0.83 ± 0.07	0.185 ± 0.009	1.02 ± 0.08
Configuration 1				
1	48	0.54 ± 0.05	0.12 ± 0.06	0.66 ± 0.07
2	84	0.64 ± 0.03	0.2 ± 0.1	0.9 ± 0.1
3	120	0.68 ± 0.06	0.13 ± 0.01	0.82 ± 0.07
4	132	0.70 ± 0.06	0.15 ± 0.01	0.84 ± 0.07
Configuration 2				
1	48	0.7 ± 0.2	0.3 ± 0.4	1.0 ± 0.4
2	84	0.54 ± 0.05	0.4 ± 0.4	1.0 ± 0.4
3	120	0.50 ± 0.04	0.2 ± 0.2	0.7 ± 0.2
4	132	0.49 ± 0.05	0.12 ± 0.05	0.6 ± 0.1
Configuration 3				
1	48	0.4 ± 0.1	0.18 ± 0.08	0.6 ± 0.1
2	84	0.44 ± 0.05	0.11 ± 0.05	0.55 ± 0.09
3	120	0.44 ± 0.04	0.10 ± 0.04	0.54 ± 0.06
4	132	0.44 ± 0.04	0.08 ± 0.03	0.52 ± 0.05

Table 4.7: Numerically integrated axial conservation of momentum for vegetated jet

Section	x/d	$\overline{M}/M_0$	M'/M_0	M/M_0
Free jet				
1	48	0.838	0.298	1.135
2	84	0.945	0.443	1.388
3	120	0.759	0.265	1.024
4	132	0.818	0.208	1.026
Configuration 1				
1	48	0.8 ± 0.2	0.27 ± 0.09	1.1 ± 0.3
2	84	0.9 ± 0.3	0.4 ± 0.2	1.3 ± 0.4
3	120	0.8 ± 0.3	0.22 ± 0.07	1.0 ± 0.4
4	132	0.8 ± 0.4	0.2 ± 0.1	1.0 ± 0.5
Configuration 2				
1	48	0.9 ± 0.2	0.7 ± 0.4	1.6 ± 0.5
2	84	0.9 ± 0.3	1.1 ± 0.2	2.0 ± 0.3
3	120	0.7 ± 0.2	0.29 ± 0.09	1.0 ± 0.3
4	132	0.7 ± 0.3	0.17 ± 0.08	0.8 ± 0.4
Configuration 3				
1	48	0.8 ± 0.13	0.41 ± 0.09	1.2 ± 0.2
2	84	0.8 ± 0.2	0.23 ± 0.07	1.0 ± 0.3
3	120	0.7 ± 0.3	0.13 ± 0.06	0.8 ± 0.3
4	132	0.7 ± 0.3	0.13 ± 0.05	0.8 ± 0.4

Table 4.8: Numerically integrated volume flux and entrainment coefficient for vegetated jet

Section	x/d	Q/Q_0	α
Free jet			
1	48	14.49	0.0638
2	84	26.37	0.0633
3	120	30.32	0.0574
4	132	36.00	0.0551
Configuration 1			
1	48	14 ± 2	0.0639
2	84	26 ± 4	0.0627
3	120	31 ± 6	0.0524
4	132	35 ± 8	0.0549
Configuration 2			
1	48	15 ± 2	0.0676
2	84	26 ± 4	0.0583
3	120	29 ± 5	0.0560
4	132	32 ± 7	0.0597
Configuration 3			
1	48	14 ± 2	0.0766
2	84	24 ± 4	0.0649
3	120	29 ± 6	0.0631
4	132	32 ± 8	0.0613

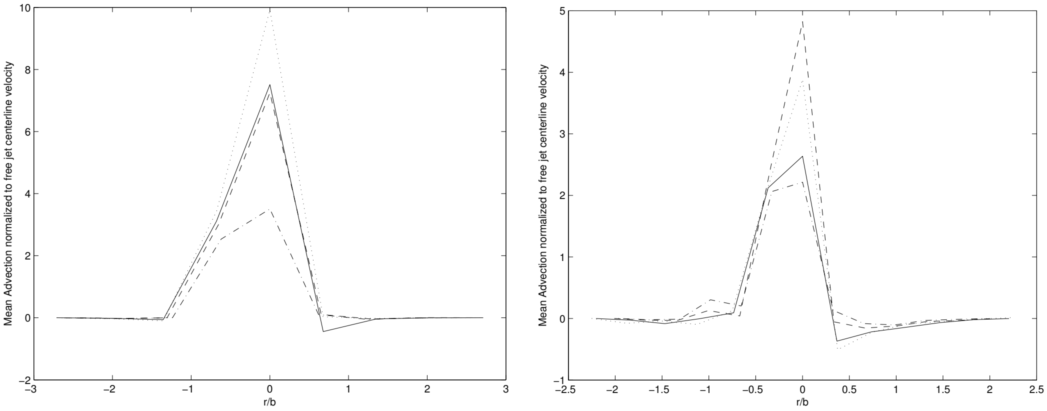

(a) Section 1 (b) Section 2

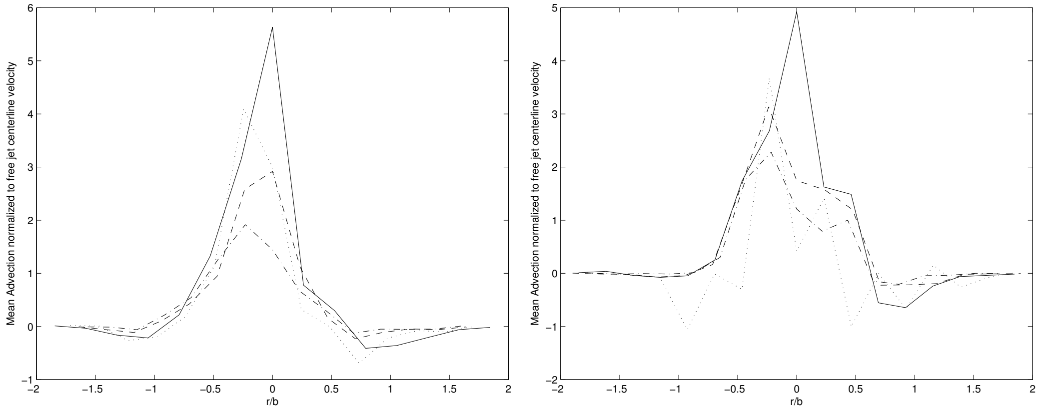

(c) Section 3 (d) Section 4

Figure 4.7: Mean advection of mean kinetic energy across spanwise sections

Configuration − free jet (−) 1 (−−) 2 (−.) 3 (· · ·)

was introduced, mean axial velocity decreased and the width of the jet increased, indicating that a transfer of mean kinetic energy from mean advection to transport, viscous dissipation and production of turbulence, see Figure 4.7 (Kundu and Cohen, 2008).

As number of plants in flow and axial distance into the array increase, changes in turbulence intensity are observed as a result of flow disruption. Nepf (1999) found that turbulent intensity is greater within sparse vegetation, decreasing as density

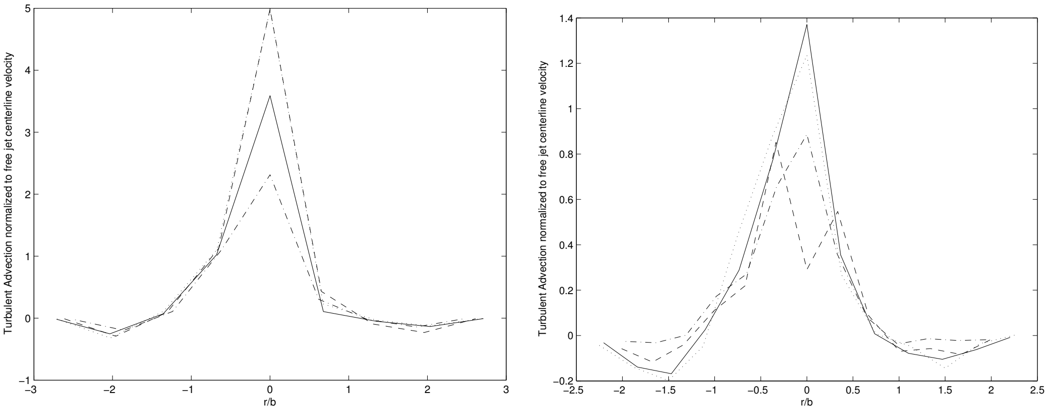

(a) Section 1 (b) Section 2

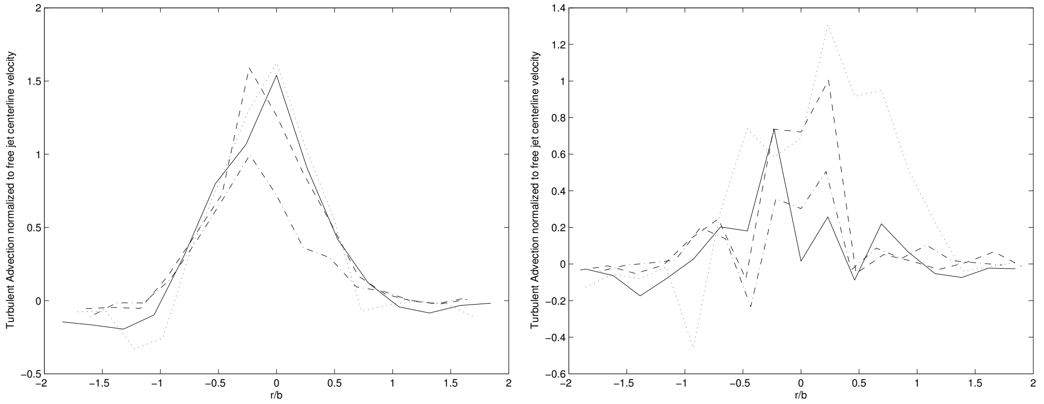

(c) Section 3 (d) Section 4

Figure 4.8: Mean advection of turbulent kinetic energy across spanwise sections

Configuration − free jet (−) 1 (−−) 2 (−.) 3 (···)

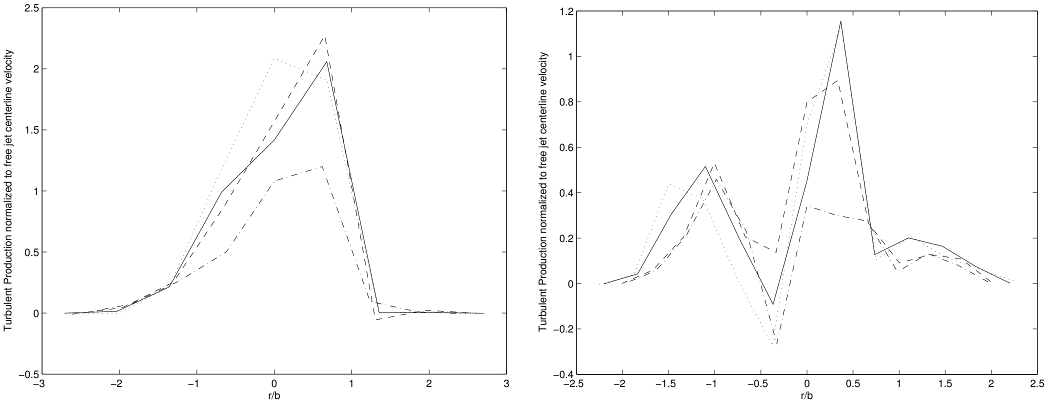

(a) Section 1

(b) Section 2

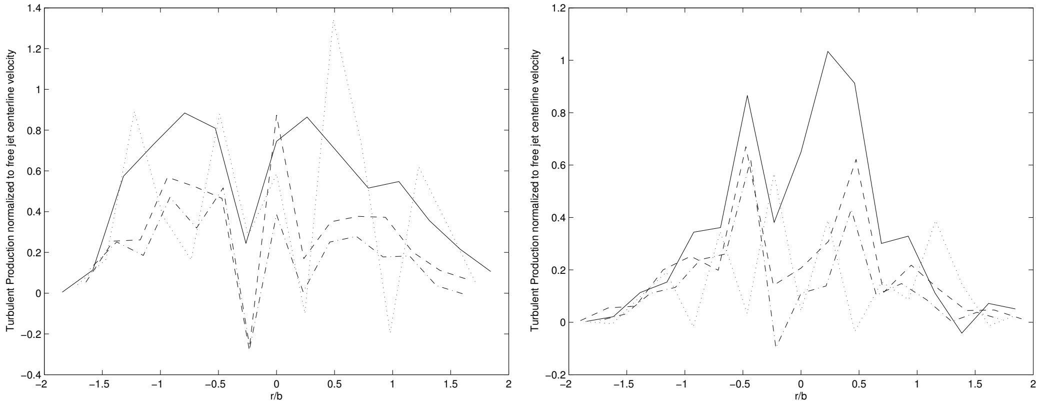

(c) Section 3

(d) Section 4

Figure 4.9: Production of turbulence across spanwise sections

Configuration − free jet (−) 1 (−−) 2 (−.) 3 (· · ·)

increases, and noted similar decreases in diffusivity due to smaller eddy scales. Likewise, Leonard and Luther (1995) found that marsh plants with increased vegetative density resulted in lower flow speeds and turbulent intensity. Figure 4.8 indicates that Reynolds stresses, the products of turbulent intensity, decrease as depth of the introduced vegetated array increases. The high rate of turbulent dissipation within the stem wake results in low turbulent intensity throughout the plant canopy (Raupach and Shaw, 1982).

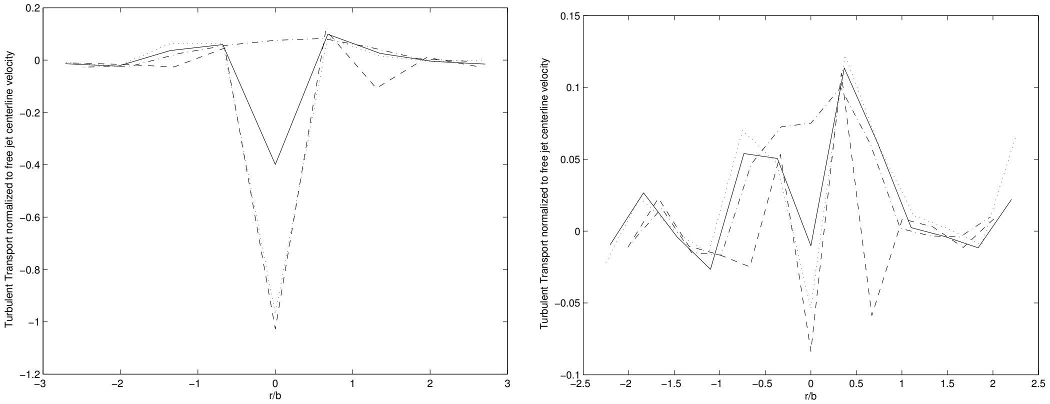

(a) Section 1 (b) Section 2

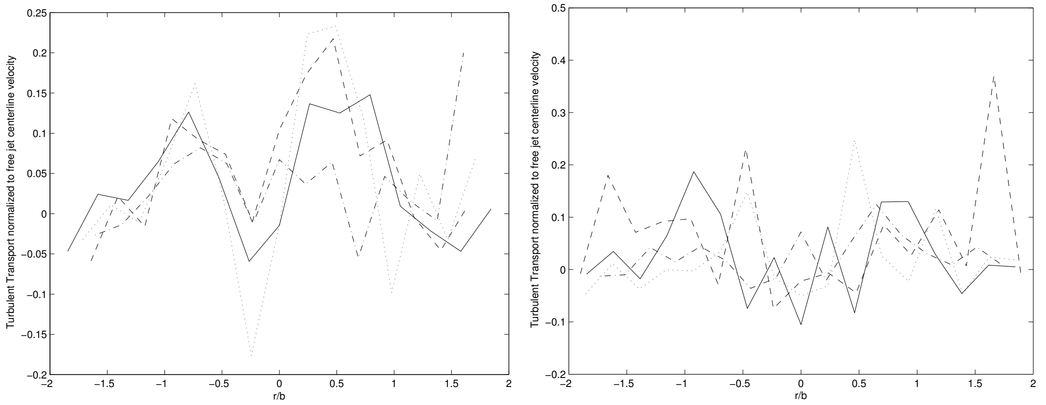

(c) Section 3 (d) Section 4

Figure 4.10: Turbulent Transport across spanwise sections

Configuration − free jet (−) 1 (−−) 2 (−.) 3 (···)

In addition, Figure 4.9 indicates that turbulent production is likewise diminished due to plants and becomes characteristically bimodal about the flow centerline in a region where mean axial flow of the jet cone is interacting with entrained fluid through shear to generate turbulence. Turbulent production due to plants in emergent vegetation, however, occurs primarily in stem wakes, which is observed for Configuration 3 in Figure 4.9d (Nepf et al., 1997). In the present study, significant turbulent production occurred at all sections of the free jet.

Though normalization of mean advection and turbulent production to free jet centerline axial velocities reveals no clear dependence on axial distance into the array, turbulent transport, by contrast, appears to be a function of axial distance. Figure 4.10 demonstrates the growth of this term as axial distance increases, though no significant dependence on depth of vegetated array is evident. As the magnitude of mean axial flow decreases with respect to axial distance, the produced and existing turbulence is increasingly moved about by other turbulence.

In all cases, normalized values are exaggerated in magnitude due to insufficient radial resolution. Equation 3.38 illustrates both axial and radial differential contributions. In general, measurement station placement in the streamwise centerline alignment was adequate to capture axial velocity profiles; however, the $2cm$ radial spacing did not capture enough measurement points within the halfwidth.

According to Leonard and Luther (1995), turbulent eddies within marsh vegetation are generated at a length scale that differs from the length scale of eddy dissipation, and the turbulence created by the stem wake is of a smaller length scale and thus quickly dissipated (Liu et al., 2008). However, evidence for neither of these statements is readily apparent in the present study. Figures 4.11 and 4.12, illustrate spectral energy density the axial centerlines of sections 4 and 3, respectively. Figure 4.12 represents a measurement location behind a plant stem and indicates the production of energetic eddies below the inertial subrange. For example, in Configuration 3 of Section 3, see Figure 4.12d, there is a substantial loss of energy observed as vortex stretching reduces the size of eddies. These small eddies decay quickly because of the increased shear stress between them (Deissler, 1984).

Figure 4.11a, depicting the spectral energy density for Section 4 of the free jet along the jet centerline, for example, shows a clear separation between anisotropic eddies, isotropic eddies and the inertial subrange. The last of these zones clearly

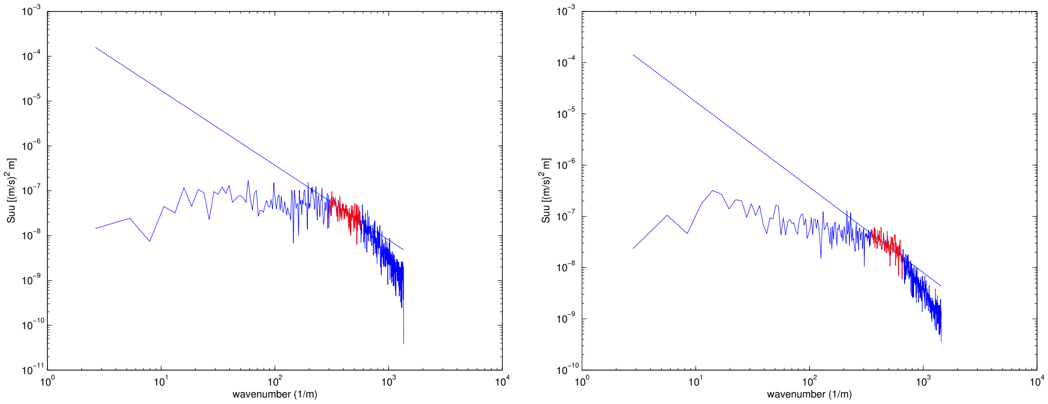

(a) Free jet

(b) Configuration 1

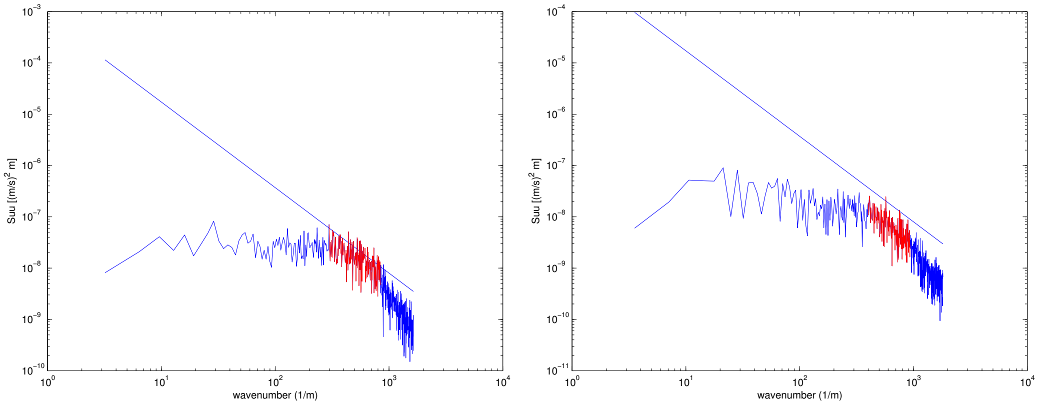

(c) Configuration 2

(d) Configuration 3

Figure 4.11: $S_{uu}(k)$ at Section 4 centerline (not behind plant stem)

$k^{-5/3}$ indicated by a straight line and inertial subrange in red

exhibits a $k^{-5/3}$ slope in accordance Kolmogorov's $K^{-5/3}$ Law. This measurement location is for the free jet and thus not affected by a plant stem; therefore, the energy spectrum should reflect a fully developed self-similar jet. As vegetation is introduced, see Figure 4.11, the inertial subrange and isotropic zone appear to shift to a higher wavenumber, corresponding to increased dissipation of increasingly smaller length-scales. No significant evolution is obvious in high-energy eddies. Unlike stem eddies, which quickly dissipate, these cumulative array eddies break up without energy loss before entering the inertial subrange.

Immediately behind a stem along the centerline at Section 3, see Figure 4.12, similar evolution of the inertial subrange is observed, though difficult to discern from the viscous dissipation range. As vegetation is introduced, the spectral energy density of larger, anisotropic eddies decreases noticeably and is most apparent from Figure 4.12d, although the magnitude of the inertial subrange remains relatively unchanged.

Approximately one halfwidth from the centerline, mean axial advection is reduced relative to radial and tangential advection. In this region, large, anisotropic eddies are entraining ambient fluid and slowly breaking down through vortex stretching. Despite the enhanced dissipation evident from the translation of the spectrum to higher wavenumbers in Figure 4.13, the shape of the spectrum is relatively unaffected as compared to figures 4.11 and 4.12, suggesting that the energy spectrum is depicting the cumulative effect of stem wakes combined with turbulent production and dissipation already present due to entrainment, though the spectral energy density of any given wavenumber for configurations 2 and 3 is decreased with respect to those for the free jet and Configuration 1.

Figure 4.14 was recorded at a location behind a plant near Figure 4.13, further out than the halfwidth on Section 4. Though the shapes of the energy density spectra are roughly identical, the magnitudes observed in Figure 4.14 are smaller by an order

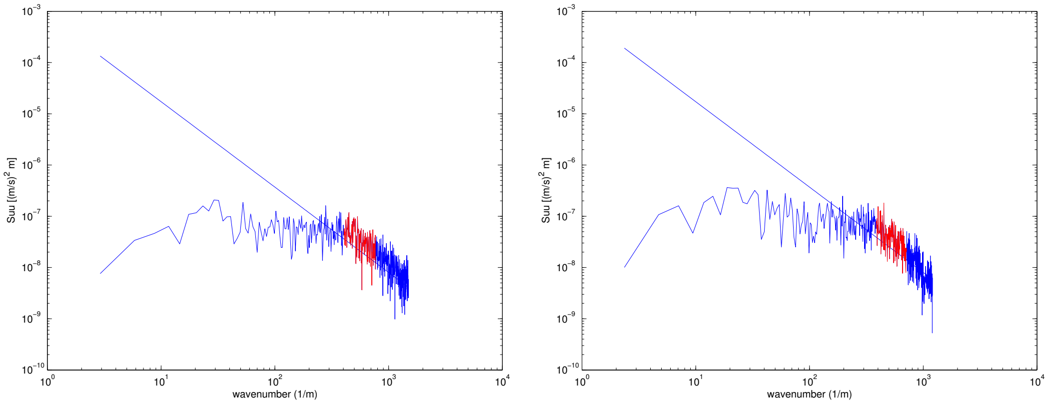

(a) Free jet (b) Configuration 1

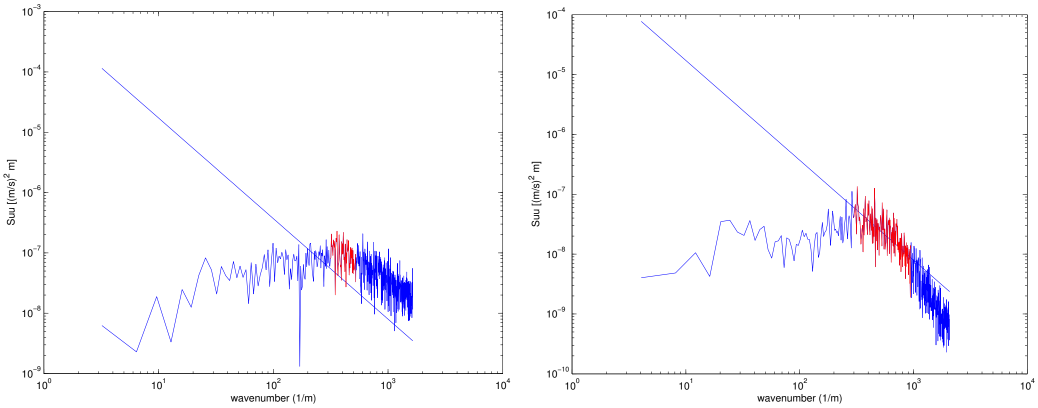

(c) Configuration 2 (d) Configuration 3

Figure 4.12: $S_{uu}(k)$ at Section 3 centerline (behind plant stem)

$k^{-5/3}$ indicated by a straight line and inertial subrange in red

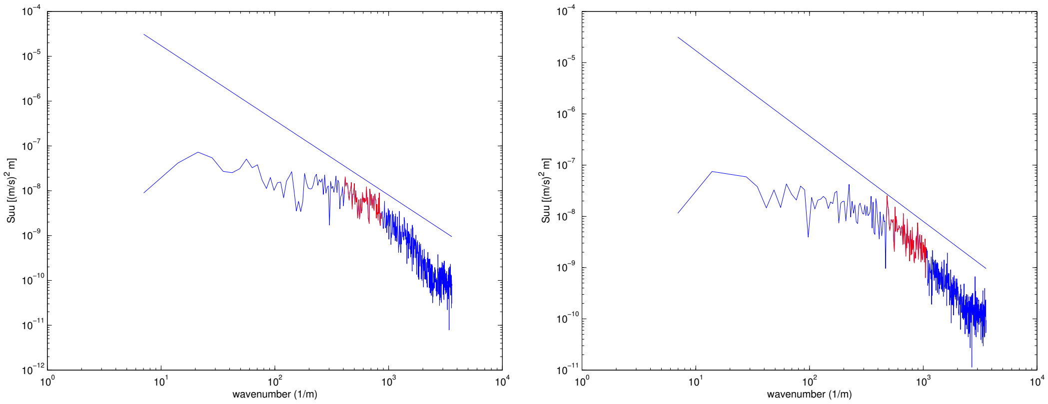

(a) Free jet (b) Configuration 1

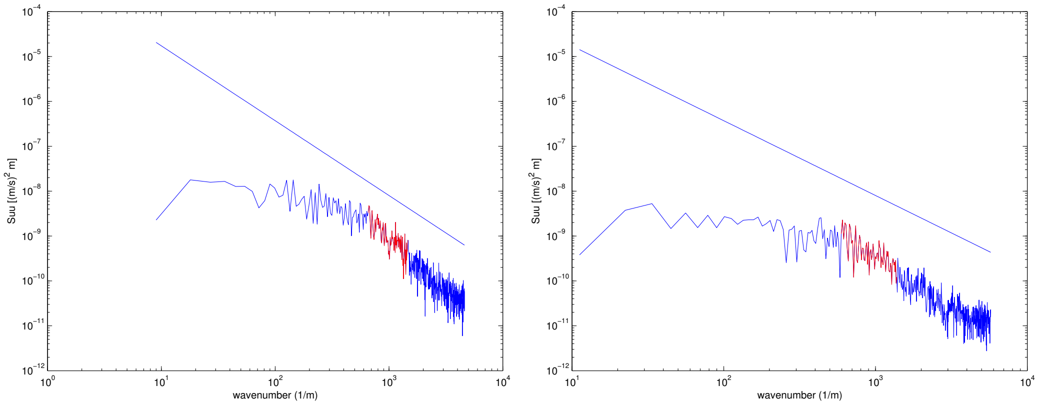

(c) Configuration 2 (d) Configuration 3

Figure 4.13: $S_{uu}(k)$ at Section 4 radial halfwidth (not behind plant stem) $k^{-5/3}$ indicated by a straight line and inertial subrange in red

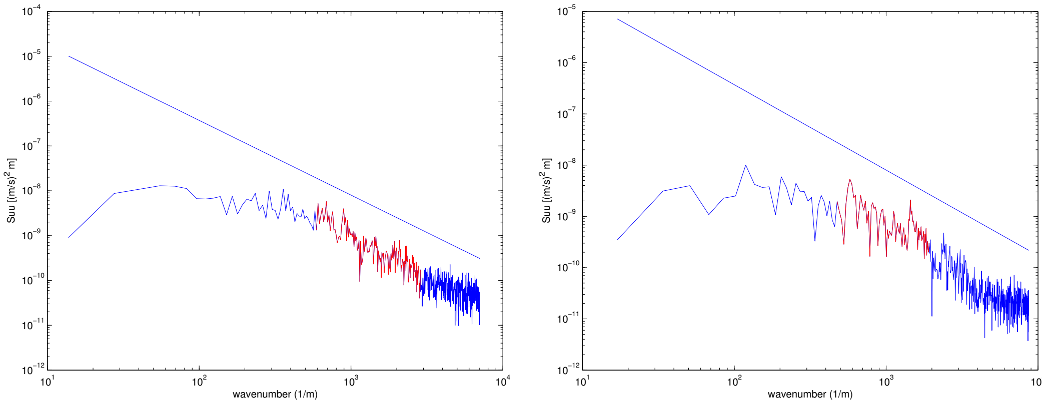

(a) Free jet (b) Configuration 1

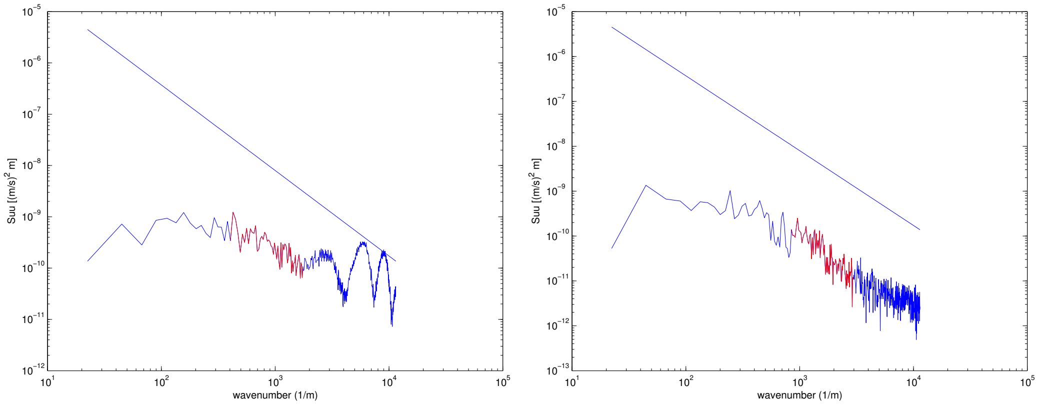

(c) Configuration 2 (d) Configuration 3

Figure 4.14: $S_{uu}(k)$ at Section 4 radial halfwidth (behind plant stem)

$k^{-5/3}$ indicated by a straight line and inertial subrange in red

Table 4.9: Dissipation rate at jet centerline

Section	x/d	location	normalized to $\overline{u}_c{}^3$
Free jet			
1	48	behind stem	0.385
2	84	not behind stem	1.12
3	120	behind stem	1.25
4	132	not behind stem	0.370
Configuration 1			
1	48	behind stem	0.385
2	84	not behind stem	1.12
3	120	behind stem	1.26
4	132	not behind stem	0.426
Configuration 2			
1	48	behind stem	0.154
2	84	not behind stem	0.222
3	120	behind stem	1.71
4	132	not behind stem	0.295
Configuration 3			
1	48	behind stem	0.0474
2	84	not behind stem	0.122
3	120	behind stem	0.730
4	132	not behind stem	0.112

of magnitude. It is difficult to determine how much, if any, of this reduction in magnitude is due to upstream stem wake; the radial distance of $4cm$ between these two points results in significantly diminished velocities and turbulent intensity in all directions. Figure 4.14c exhibits unusual high-wavenumber structures that may indicate the vortex shedding frequency of the upstream plant stem.

In the majority of measurement station records, it is difficult to accurately calculate rate of dissipation from spectral energy density due to frequently unclear boundaries of the inertial subrange. In general, the inertial subrange is more readily identified in the free jet than in the fully vegetated case.

Tables 4.9 and 4.10 demonstrate an application of Equation 3.43 to figures 4.11

Table 4.10: Dissipation rate at jet halfwidth

Section	x/d	location	normalized to $\overline{u}_c{}^3$
Free jet			
4	132	not behind stem	0.0611
4	132	behind stem	0.0208
Configuration 1			
4	132	not behind stem	0.0604
4	132	behind stem	0.0135
Configuration 2			
4	132	not behind stem	0.0156
4	132	behind stem	0.0015
Configuration 3			
4	132	not behind stem	0.0036
4	132	behind stem	0.0005

to 4.14. Although the resulting centerline rates of dissipation normalized to mean axial centerline velocity are greater behind stems presented in Table 4.9, the limited number of processed profiles suggests caution. With similar caution, Table 4.10 suggests that, though the two measurement stations are too far radially separated for quantitative comparison, cumulative upstream stem wakes represent the dominant reduction of dissipation rate at the radial halfwidth and beyond.

5. SUMMARY AND CONCLUSIONS

This study established a connection between traditional jet studies and current investigations of drag and turbulent kinetic energy in vegetative arrays. In addition to verifying and expanding the body of knowledge regarding self-similar axisymmetric turbulent jets, statistical methods are applied to several configurations of flow obstruction with vegetated arrays designed to investigate effects on jet self-similarity development, conservation of momentum and turbulent kinetic energy.

Using flow characterization techniques applied to free jets, vegetated flow equivalents for jets impinging on vegetation are suggested and determined, resulting in parameters that express the retained jet characteristics, as well as take into account multiple stem wake effects. Each configuration is executed under five collapsible speeds to demonstrate preservation of jet self-similarity, to apply self-similarity parameters and to determine experimental uncertainty, which previous free-jet studies have not considered. This method of analysis, in addition to standard dye studies and PIV, provides a means of characterizing natural and industrial jet flows through marsh vegetation or other sparse stem array.

Despite the limited configuration and scale of the experiment, even sparse, smooth simulated vegetation demonstrated a significant and effective ability to extract mean axial velocity and momentum from mean flow, converting it to radial or tangential velocity, Reynolds stress and turbulence for eventual dissipation. This enhanced dissipation does support the claim that marsh vegetation is an effective means of reducing the mean velocity of storm surge. The axial velocity decay parameter B reduces from 5.8 ± 0.2 for the free jet to 3.7 ± 0.1 for the fully vegetated configuration, indicating enhanced decay of mean axial centerline velocity. Likewise, the entrainment coefficient α at $\frac{x}{d} = 132$ increased from 0.0551 for the free jet to 0.613

for the fully vegetated case, indicating a greater rate of spreading. Caution must be applied to this conclusion if storm surge is sufficiently high to submerge vegetation, in which case the canopy will not correspond to the emergent vegetation modeled in this study.

As predicted by energy balance, mean axial flow is converted to radial or tangential flow, turbulence or dissipated at an accelerated rate within a vegetative array. As confirmation, total axial momentum normalized to initial momentum was found to range from 1.02 ± 0.08 for the free jet to 0.52 ± 0.05 at $\frac{x}{d} = 132$ for the fully vegetated configuration, indicating a failure of conservation of momentum in the presence of vegetation. An analysis of turbulent kinetic energy indicated mean advection of both mean and turbulent kinetic energy, as well as turbulent production, decreased as plant stems were introduced into the flow. Turbulent transport, on the other hand, appeared to be more a function of axial density and increased in the distant zone of established flow.

The purpose of this study was two-fold: to test the applicability of jet self-similarity techniques to vegetated flows and the rule of thumb stating that sparse emergent vegetation has the ability to dissipate storm surge. Although additional research involving variable stem density and diameter is required to confirm full applicability of self-similarity analysis to vegetated arrays, the results of the present study offer initial evidence towards the validity of this approach, and the abundance of literature regarding self-similar jets and relative ease of the method suggest that further research is worthwhile. More importantly, however, this study found that even a relatively short length of sparse vegetation is capable of significantly reducing the axial velocity of a jet and enhancing turbulent dissipation. Actual storm surge, however, more closely resembles a line source than a point source and is incapable of lateral spreading. Therefore, this study, as a result, cannot provide conclusive evidence to support the argument that emergent wetlands serve as protection against coastal storm surge.

REFERENCES

Abd-Rabbo, A. and Weaver, D. (1986), ‘A flow visualization study of flow development in a staggered tube array’, *Journal of Sound and Vibration* **106**(2), 241–256.

Agrawal, A. and Prasad, A. (2002), ‘Properties of vortices in the self-similar turbulent jet’, *Experiments in Fluids* **33**(4), 565–577.

Agrawal, A. and Prasad, A. (2003), ‘Integral solution for the mean flow profiles of turbulent jets, plumes, and wakes’, *Journal of Fluids Engineering* **125**(5), 813–822.

Akilli, H., Akar, A. and Karakus, C. (2004), ‘Flow characteristics of circular cylinders arranged side-by-side in shallow water’, *Flow Measurement & Instrumentation* **15**(4), 187.

Atta, C. W. V. (1974), ‘Sampling techniques in turbulence measurements’, *Annual Review of Fluid Mechanics* **6**(1), 75–91.

Balachandar, S. and Parker, S. J. (2002), ‘Onset of vortex shedding in an inline and staggered array of rectangular cylinders.’, *Physics of Fluids* **14**(10), 3714.

Braun, M. and Kudriavtsev, V. (1995), ‘Fluid-flow structures in staggered banks of cylinders located in a channel’, *Journal of Fluids Engineering* **117**(1), 36–44.

Bremhorst, K. and Harch, W. (1978), ‘Mechanism of jet entrainment’, *AIAA Journal* **16**(10), 1104–1106.

Browne, L. W. B., Antonia, R. A. and Shah, D. A. (1987), ‘Turbulent energy-dissipation in a wake’, *Journal of Fluid Mechanics* **179**, 307–326.

Carollo, F. G., Ferro, V. and Termini, D. (2002), ‘Flow velocity measurements in vegetated channels’, *Journal of Hydraulic Engineering* **128**(7), 664.

Crow, S. C. and Champagne, F. H. (1971), ‘Orderly structure in jet turbulence’, *Journal of Fluid Mechanics* **48**, 547.

Dahm, W. (1987), ‘Measurements of entrainment and mixing in turbulent jets’, *AIAA Journal* **25**(9), 1216–1223.

Deissler, R. G. (1984), 'Turbulent solutions of the equations of fluid motion', *Review of Modern Physics* **56**(2), 223.

Elsner, J. and Elsner, W. (1996), 'On the measurement of turbulence energy dissipation', *Measurement Science & Technology* **7**(10), 1334–1348.

Falcone, A. (2003), 'Entrainment velocity in an axisymmetric turbulent jet', *Jounal of Fluids Engineering* **125**(4), 620–627.

Gambi, M., Nowell, A. and Jumars, P. (1990), 'Flume observations on flow dynamics in zosera-marina (eelgrass) beds', *Marine Ecology. Progress Series* **61**(1–2), 159–169.

Goring, D. and Nikora, V. (2002), 'Despiking acoustic doppler velocimeter data.', *Journal of Hydraulic Engineering* **128**(1), 117.

Guillaume, D. and LaRue, J. (1999), 'Investigation of the flopping regime with two-, three- and four-cylinder arrays', *Experiments in Fluids* **27**(2), 145–156.

Huai, W.-x., Chen, Z.-b., Han, J., Zhang, L.-x. and Zeng, Y.-h. (2009), 'Mathematical model for the flow with submerged and emerged rigid vegetation', *Journal of Hydrodynamics, Series B* **21**(5), 722–729.

Hussain, A. K. M. F. and Zaman, K. B. M. Q. (1981), 'The preferred mode of the axisymmetric jet', *Journal of Fluid Mechanics* **110**, 39–71.

Hussein, H. J., Capp, S. P. and George, W. K. (1994), 'Velocity-measurements in a high-reynolds-number, momentum-conserving, axisymmetrical, turbulent jet', *Journal of Fluid Mechanics* **258**, 31–75.

James, C., Birkhead, A., Jordanova, A. and O'Sullivan, J. (2004), 'Flow resistance of emergent vegetation', *Journal of Hydraulic Research* **42**(4), 390–398.

Jendrzejczyk, J., Chen, S. and Wambsganss, M. (1979), 'Dynamic responses of a pair of circular tubes subjected to liquid cross flow', *Journal of Sound and Vibration*

67(2), 263–273.

Kadlec, R. H. (1990), 'Overland flow in wetlands: vegetation resistance.', *Journal of Hydraulic Engineering* **116**(5), 691–706.

Kassab, S., Bakry, A. and Hassan, W. (1996), 'Laser doppler anemometry measurements in an axisymmetric turbulent jet', *Review of Scientific Instruments* **67**(5), 1842.

Keller, J. (1994), 'Entrainment effects in vortex flows.', *Physics of Fluids* **6**(9), 3028.

Kiya, M., Arie, M., Tamura, H. and Mori, H. (1980), 'Vortex shedding from two circular cylinders in staggered arrangement', *Journal of Fluids Engineering* **102**(2), 166–171.

Kundu, P. K. and Cohen, I. M. (2008), *Fluid Mechanics (4th Edition)*, Burlington, MA: Elsevier.

Leonard, L. A. and Luther, M. E. (1995), 'Flow hydrodynamics in tidal marsh canopies', *Limnology and Oceanography* **40**(8), 1474–1484.

Liepmann, D. (1991), 'Streamwise vorticity and entrainment in the near field of a round jet.', *Physics of Fluids A* **3**(5), 1179.

Liepmann, D. and Gharib, M. (1992), 'The role of streamwise vorticity in the near-field entrainment of round jets', *Journal of Fluid Mechanics* **245**, 643–668.

Lightbody, A. F. and Nepf, H. M. (2006), 'Prediction of velocity profiles and longitudinal dispersion in emergent salt marsh vegetation.', *Limnology & Oceanography* **51**(1), 218–228.

Lipari, G. (2011), 'Review of experimental data on incompressible turbulent round jets', *Flow Turbulence and Combustion* **87**(1), 79–114.

Liu, D., Diplas, P., Fairbanks, J. D. and Hodges, C. C. (2008), 'An experimental study of flow through rigid vegetation', *Journal of Geophysical Research* **113**, F04015.

Luo, S., Gan, T. and Chew, Y. (1996), ‘Uniform flow past one (or two in tandem) finite length circular cylinder(s)’, *Journal of Wind Engineering and Industrial Aerodynamics* **59**(1), 69–93.

Mih, W. (1989), ‘Equations for axisymmetric and two-dimensional turbulent jets’, *Journal of Hydraulic Engineering* **115**(12), 1715–1719.

Murphy, E., Ghisalberti, M. and Nepf, H. (2007), ‘Model and laboratory study of dispersion in flows with submerged vegetation’, *Water Resources Research* **43**(5).

Neary, V. S. (2003), ‘Numerical solution of fully developed flow with vegetative resistance’, *Journal of Engineering Mechanics* **129**(5), 558.

Nepf, H. (1999), ‘Drag, turbulence, and diffusion in flow through emergent vegetation’, *Water Resources Research* **35**(2), 479–489.

Nepf, H. and Ghisalberti, M. (2008), ‘Flow and transport in channels with submerged vegetation’, *Acta Geophysica* **56**, 753–777.

Nepf, H. M., Sullivan, J. A. and Zavistoski, R. A. (1997), ‘A model for diffusion within emergent vegetation’, *Limnology and Oceanography* **42**(8), 1735–1745.

Neumeier, U. (2004), ‘Flow resistance and associated sedimentary processes in a spartina maritima salt-marsh’, *Journal of Coastal Research* **20**(2), 435–447.

Papanicolaou, P. N. and List, E. J. (1988), ‘Investigations of round vertical turbulent buoyant jets’, *Journal of Fluid Mechanics* **195**, 341–391.

Pye, K., Shi, Z. and Pethick, J. S. (1995), ‘Flow structure in and above the various heights of a saltmarsh canopy: a laboratory flume study’, *Journal of Coastal Research* **11**(4), 1204.

Rajaratnam, N. (1976), *Turbulent Jets*, Amsterdam; New York: Elsevier.

Ramaprian, B. and Chandrasekhara, M. (1985), ‘Lda measurements in plane turbulent jets’, *Journal of Fluids Engineering* **107**(2), 264–271.

Raupach, M. (1992), ‘Drag and drag partition on rough surfaces’, *Boundary-Layer*

Meteorology **60**(4), 375–395.

Raupach, M. R. and Shaw, R. H. (1982), ‘Averaging procedures for flow within vegetation canopies.’, *Boundary-Layer Meteorology* **22**(1), 79–90.

Ricou, F. and Spalding, D. (1961), ‘Measurements of entrainment by axisymmetrical turbulent jets’, *Journal of Fluid Mechanics* **11**(1), 21–32.

Sadeque, M. A. F., Rajaratnam, N. and Loewen, M. R. (2008), ‘Flow around cylinders in open channels.’, *Journal of Engineering Mechanics* **134**(1), 60–71.

Schneider, W. (1985), ‘Decay of momentum flux in submerged jets’, *Journal of Fluid Mechanics* **154**, 91–110.

Shinneeb, A., Bugg, J. and R, B. (2011), ‘Coherent structures in shallow water jets’, *Journal of Fluids Engineering* **133**(1).

Shlien, D. J. (1987), ‘Observations of dispersion of entrained fluid in the self-preserving region of a turbulent jet’, *Journal of Fluid Mechanics* **183**, 163.

Stoesser, T., Salvador, G., Rodi, W. and Diplas, P. (2009), ‘Large eddy simulation of turbulent flow through submerged vegetation’, *Transport in Porous Media* **78**(3), 347–365.

Tanino, Y. and Nepf, H. (2008), ‘Laboratory investigation of mean drag in a random array of rigid, emergent cylinders’, *Journal of Hydraulic Engineering* **134**(1), 34–41.

Tanino, Y. and Nepf, H. (2009), ‘Laboratory investigation of lateral dispersion within dense arrays of randomly distributed cylinders at transitional reynolds number’, *Physics of Fluids* **21**(4).

Turner, J. S. (1986), ‘Turbulent entrainment–the development of the entrainment assumption, and its application to geophysical flows’, *Journal of Fluid Mechanics* **173**, 431–471.

Wamsley, T. V. (2010), ‘The potential of wetlands in reducing storm surge’, *Ocean*

Engineering **37**(1), 59–68.

Weisgraber, T. and Liepmann, D. (1998), 'Turbulent structure during transition to self-similarity in a round jet', *Experiments in Fluids* **24**(3), 210–224.

Wygnanski, I. and Fiedler, H. (1969), 'Some measurements in the self-preserving jet', *Journal of Fluid Mechanics* **38**(3), 577–612.

Xu, G. and Antonia, R. (2002), 'Effect of different initial conditions on a turbulent round free jet', *Experiments in Fluids* **33**(5), 677–683.

Yagci, O., Tschiesche, U. and Kabdasli, M. (2010), 'The role of different forms of natural riparian vegetation on turbulence and kinetic energy characteristics', *Advances in Water Resources* **33**(5), 601–614.

APPENDIX A

DERIVATION OF TURBULENT KINETIC ENERGY BALANCE

Decomposing velocity into mean and turbulent components—recall that $u_i = \overline{u_i} + {u_i}'$—produces

$$\begin{gathered}
\left(\overline{u_j} + {u_j}'\right) \frac{\partial \left(\overline{u_i} + {u_i}'\right)}{\partial x_j} - \frac{\left(\overline{u_\theta} + {u_\theta}'\right)^2}{r} \hat{r} + \\
\frac{\left(\overline{u_r} + {u_r}'\right)\left(\overline{u_\theta} + {u_\theta}'\right)}{r} \hat{\theta} = -\frac{1}{\rho} \frac{\partial \left(\overline{p} + p'\right)}{\partial x_i} + \epsilon
\end{gathered} \tag{A.1}$$

Multiplying out the terms and ensemble averaging each produces equations

$$\begin{aligned}
\overline{u_j} \frac{\partial \overline{u_i}}{\partial x_j} + \overline{u_j} \frac{\partial {u_i}'}{\partial x_j} + {u_j}' \frac{\partial \overline{u_i}}{\partial x_j} + \\
{u_j}' \frac{\partial {u_i}'}{\partial x_j} - \left(\frac{\overline{u_\theta}^2}{r} + \frac{u'_\theta u'_\theta}{r} + 2 \frac{\overline{u_\theta} {u_\theta}'}{r} \right) \hat{r} + \\
\left(\frac{\overline{u_r}\,\overline{u_\theta}}{r} + \frac{{u_r}'{u_\theta}'}{r} + \frac{\overline{u_r}{u_\theta}'}{r} + \frac{{u_r}'\overline{u_\theta}}{r} \right) \hat{\theta} = -\left(\frac{1}{\rho} \frac{\partial \overline{p}}{\partial x_i} + \frac{1}{\rho} \frac{\partial p'}{\partial x_i} \right) + \epsilon
\end{aligned} \tag{A.2}$$

$$\begin{aligned}
\overline{u_j} \frac{\partial \overline{u_i}}{\partial x_j} + \left\langle {u_j}' \frac{\partial {u_i}'}{\partial x_j} \right\rangle - \\
\left(\frac{\overline{u_\theta}^2}{r} + \frac{\langle u'_\theta u'_\theta \rangle}{r} \right) \hat{r} + \left(\frac{\overline{u_r}\,\overline{u_\theta}}{r} + \frac{\langle {u_r}'{u_\theta}' \rangle}{r} \right) \hat{\theta} = -\frac{1}{\rho} \frac{\partial \overline{p}}{\partial x_i} + \epsilon
\end{aligned} \tag{A.3}$$

respectively.

Subtracting Equation A.3, the inital expression for mean kinetic energy, from

Equation A.2 leaves the initial expression for turbulent kinetic energy

$$\begin{aligned}\overline{u_j}\frac{\partial u_i'}{\partial x_j} + u_j'\frac{\partial \overline{u_i}}{\partial x_j} + u_j'\frac{\partial u_i'}{\partial x_j} - \left\langle u_j'\frac{\partial u_i'}{\partial x_j}\right\rangle - \left(\frac{u'_\theta u'_\theta}{r} + 2\frac{\overline{u_\theta}u_\theta'}{r} - \frac{\langle u'_\theta u'_\theta\rangle}{r}\right)\hat{r} + \\ \left(\frac{u_r'u_\theta'}{r} + \frac{\overline{u_r}u_\theta'}{r} + \frac{u_r'\overline{u_\theta}}{r} - \frac{\langle u_r'u_\theta'\rangle}{r}\right)\hat{\theta} = -\frac{1}{\rho}\frac{\partial p'}{\partial x_i} + \epsilon\end{aligned} \tag{A.4}$$

Multiplying this expression through by u_k' produces

$$\begin{aligned}\overline{u_j}u_k'\frac{\partial u_i'}{\partial x_j} + u_k'u_j'\frac{\partial \overline{u_i}}{\partial x_j} + u_k'u_j'\frac{\partial u_i'}{\partial x_j} - \\ u_k'\left\langle u_j'\frac{\partial u_i'}{\partial x_j}\right\rangle - u_r'\left(\frac{u'_\theta u'_\theta}{r} + 2\frac{\overline{u_\theta}u_\theta'}{r} - \frac{\langle u'_\theta u'_\theta\rangle}{r}\right)\hat{r} + \\ u_\theta'\left(\frac{u_r'u_\theta'}{r} + \frac{\overline{u_r}u_\theta'}{r} + \frac{u_r'\overline{u_\theta}}{r} - \frac{\langle u_r'u_\theta'\rangle}{r}\right)\hat{\theta} = -\frac{1}{\rho}u_k'\frac{\partial p'}{\partial x_i} + \epsilon\end{aligned} \tag{A.5}$$

which upon ensemble averaging yields

$$\begin{aligned}\overline{u_j}\left\langle u_k'\frac{\partial u_i'}{\partial x_j}\right\rangle + \langle u_k'u_j'\rangle\frac{\partial \overline{u_i}}{\partial x_j} + \\ \left\langle u_k'u_j'\frac{\partial u_i'}{\partial x_j}\right\rangle - \left(\frac{\langle u_r'u'_\theta u'_\theta\rangle}{r} + 2\frac{\overline{u_\theta}\,\langle u_r'u_\theta'\rangle}{r}\right)\hat{r} + \\ \left(\frac{\langle u_r'u_\theta'u_\theta'\rangle}{r} + \frac{\overline{u_r}\,\langle u_\theta'u_\theta'\rangle}{r} + \frac{\overline{u_\theta}\,\langle u_r'u_\theta'\rangle}{r}\right)\hat{\theta} = -\frac{1}{\rho}\left\langle u_k'\frac{\partial p'}{\partial x_i}\right\rangle + \epsilon\end{aligned} \tag{A.6}$$

where $\langle u_i'\rangle = 0$ and $\langle \overline{u_i}u_i'u_j'\rangle = \overline{u_i}\,\langle u_i'u_j'\rangle$.

At this point, taking Equation A.6 and swapping i and k indices generates

$$\begin{aligned}\overline{u_j}\left\langle u_i'\frac{\partial u_k'}{\partial x_j}\right\rangle + \langle u_i'u_j'\rangle\frac{\partial \overline{u_k}}{\partial x_j} + \\ \left\langle u_i'u_j'\frac{\partial u_k'}{\partial x_j}\right\rangle - \left(\frac{\langle u_r'u'_\theta u'_\theta\rangle}{r} + 2\frac{\overline{u_\theta}\,\langle u_r'u_\theta'\rangle}{r}\right)\hat{r} + \\ \left(\frac{\langle u_r'u_\theta'u_\theta'\rangle}{r} + \frac{\overline{u_r}\,\langle u_\theta'u_\theta'\rangle}{r} + \frac{\overline{u_\theta}\,\langle u_r'u_\theta'\rangle}{r}\right)\hat{\theta} \\ = -\frac{1}{\rho}\left\langle u_i'\frac{\partial p'}{\partial x_k}\right\rangle + \epsilon\end{aligned} \tag{A.7}$$

Next, summing equations A.6 and A.7 and collapsing indices so that $i = k$ produces

$$\begin{aligned}
2\overline{u_j}\left\langle {u_i}'\frac{\partial {u_i}'}{\partial x_j}\right\rangle + 2\left\langle {u_i}'{u_j}'\right\rangle\frac{\partial \overline{u_i}}{\partial x_j} + \\
2\left\langle {u_i}'{u_j}'\frac{\partial {u_i}'}{\partial x_j}\right\rangle - \left(2\frac{\left\langle {u_r}'u'_\theta u'_\theta\right\rangle}{r} + 4\frac{\overline{u_\theta}\left\langle {u_r}'{u_\theta}'\right\rangle}{r}\right)\hat{r} + \\
\left(2\frac{\left\langle {u_r}'{u_\theta}'{u_\theta}'\right\rangle}{r} + 2\frac{\overline{u_r}\left\langle {u_\theta}'{u_\theta}'\right\rangle}{r} + 2\frac{\overline{u_\theta}\left\langle {u_r}'{u_\theta}'\right\rangle}{r}\right)\hat{\theta} \\
= -\frac{2}{\rho}\left\langle {u_i}'\frac{\partial p'}{\partial x_i}\right\rangle + \epsilon
\end{aligned} \tag{A.8}$$

Applying continuity identities,

$$\begin{aligned}
\frac{\partial\left\langle {u_i}'{u_j}'\right\rangle}{\partial x_j} &= \left\langle {u_j}'\frac{\partial {u_i}'}{\partial x_j}\right\rangle + \left\langle {u_i}'\frac{\partial {u_j}'}{\partial x_j}\right\rangle \\
&= \left\langle {u_j}'\frac{\partial {u_i}'}{\partial x_j}\right\rangle + 0 && \text{(A.9)} \\
\frac{\partial\left\langle {u_i}'{u_i}'\right\rangle}{\partial x_j} &= 2\left\langle {u_i}'\frac{\partial {u_i}'}{\partial x_j}\right\rangle && \text{(A.10)} \\
\frac{\partial\left\langle {u_i}'{u_i}'{u_j}'\right\rangle}{\partial x_j} &= \left\langle {u_j}'\frac{\partial {u_i}'{u_i}'}{\partial x_j}\right\rangle + \left\langle {u_i}'{u_i}'\frac{\partial {u_j}'}{\partial x_j}\right\rangle \\
&= \left\langle {u_j}'\frac{\partial {u_i}'{u_i}'}{\partial x_j}\right\rangle + 0 \\
&= \left\langle {u_j}'2\left({u_i}'\frac{\partial {u_i}'}{\partial x_j}\right)\right\rangle \\
&= 2\left\langle {u_i}'{u_j}'\frac{\partial {u_i}'}{\partial x_j}\right\rangle && \text{(A.11)}
\end{aligned}$$

the contracted form of the energy equation reduces to

$$\begin{aligned}
\overline{u_j}\left\langle\frac{\partial {u_i}'{u_i}'}{\partial x_j}\right\rangle + 2\frac{\partial\overline{u_i}}{\partial x_j}\left\langle {u_i}'{u_j}'\right\rangle + \\
\left\langle\frac{\partial {u_i}'{u_i}'{u_j}'}{\partial x_j}\right\rangle - \frac{2}{r}\left(\left\langle {u_r}'u'_\theta u'_\theta\right\rangle + 2\overline{u_\theta}\left\langle {u_r}'{u_\theta}'\right\rangle\right)\hat{r} + \\
\frac{2}{r}\left(\left\langle {u_r}'{u_\theta}'{u_\theta}'\right\rangle + \overline{u_r}\left\langle {u_\theta}'{u_\theta}'\right\rangle + \overline{u_\theta}\left\langle {u_r}'{u_\theta}'\right\rangle\right)\hat{\theta} = -\frac{2}{\rho}\left\langle\frac{\partial {u_i}'p'}{\partial x_i}\right\rangle + \epsilon
\end{aligned} \tag{A.12}$$

Grouping terms by physical significance yields

$$\begin{aligned}
&\left[\overline{u_j}\left\langle\frac{\partial u_i{}'u_i{}'}{\partial x_j}\right\rangle\right]_{\text{advection}} + \\
&\left[2\frac{\partial\overline{u_i}}{\partial x_j}\left\langle u_i{}'u_j{}'\right\rangle + \frac{2}{r}\left(\overline{u_r}\left\langle u_\theta{}'u_\theta{}'\right\rangle + \overline{u_\theta}\left\langle u_r{}'u_\theta{}'\right\rangle\right)\hat{\theta} - \frac{2}{r}\left(2\overline{u_\theta}\left\langle u_r{}'u_\theta{}'\right\rangle\right)\hat{r}\right]_{\text{production}} + \\
&\left[\left\langle\frac{\partial u_i{}'u_i{}'u_j{}'}{\partial x_j}\right\rangle + \frac{2}{r}\left\langle u_r{}'u_\theta{}'u_\theta{}'\right\rangle\hat{\theta} - \frac{2}{r}\left\langle u_r{}'u_\theta'u_\theta'\right\rangle\hat{r}\right]_{\text{turbulence transport}} = \\
&\left[-\frac{2}{\rho}\left\langle\frac{\partial u_i{}'p'}{\partial x_i}\right\rangle\right]_{\text{pressure transport}} + [\epsilon]_{\text{dissipation}}
\end{aligned} \tag{A.13}$$

Expanding i and j indices reduces tensors in Equation A.12 to directional vectors,

$$\begin{aligned}
&\left[\overline{u}\frac{\partial\left\langle u'u'\right\rangle}{\partial x} + \overline{v}\frac{\partial\left\langle u'u'\right\rangle}{\partial r} + 2\frac{\partial\overline{u}}{\partial x}\left\langle u'u'\right\rangle + 2\frac{\partial\overline{u}}{\partial r}\left\langle u'u'\right\rangle + \right. \\
&\left.\frac{\partial\left\langle u'u'u'\right\rangle}{\partial x} + \frac{1}{r}\frac{\partial\left(r\left\langle v'u'u'\right\rangle\right)}{\partial r} = -\frac{2}{\rho}\frac{\partial\left\langle u'p\right\rangle}{\partial x} + \epsilon\right]\hat{x}
\end{aligned} \tag{A.14}$$

$$\begin{aligned}
&\left[\overline{u}\frac{\partial\left\langle v'v'\right\rangle}{\partial x} + \overline{v}\frac{\partial\left\langle v'v'\right\rangle}{\partial r} + 2\frac{\partial\overline{v}}{\partial x}\left\langle v'u'\right\rangle + 2\frac{\partial\overline{v}}{\partial r}\left\langle v'v'\right\rangle + \frac{\partial\left\langle u'v'v'\right\rangle}{\partial x} + \right. \\
&\left.\frac{1}{r}\frac{\partial\left(r\left\langle v'v'v'\right\rangle\right)}{\partial r} - \frac{2}{r}\left(\left\langle v'w'w'\right\rangle + 2\overline{w}\left\langle v'w'\right\rangle\right) = -\frac{2}{\rho}\frac{\partial\left\langle v'p\right\rangle}{\partial r} + \epsilon\right]\hat{r}
\end{aligned} \tag{A.15}$$

$$\begin{aligned}
&\left[\overline{u}\frac{\partial\left\langle w'w'\right\rangle}{\partial x} + \overline{v}\frac{\partial\left\langle w'w'\right\rangle}{\partial r} + 2\frac{\partial\overline{w}}{\partial x}\left\langle w'u'\right\rangle + 2\frac{\partial\overline{w}}{\partial r}\left\langle w'v'\right\rangle + \frac{\partial\left\langle u'w'w'\right\rangle}{\partial x} + \right. \\
&\left.\frac{1}{r}\frac{\partial\left(r\left\langle v'w'w'\right\rangle\right)}{\partial r} + \frac{2}{r}\left(\left\langle v'w'w'\right\rangle + \overline{v}\left\langle w'w'\right\rangle + \overline{w}\left\langle w'v'\right\rangle\right) = \epsilon\right]\hat{\theta}
\end{aligned} \tag{A.16}$$

where $\frac{\partial}{\partial\theta} = 0$ due to swirl-free conditions. Defining a quantity $q = u'u' + v'v' + w'w'$ and summing the scalar values of kinetic energy vectors given by equations A.14 – A.16, produces

$$\begin{aligned}
&\left(\overline{u}\frac{\partial}{\partial x} + \overline{v}\frac{\partial}{\partial r}\right)\left\langle q\right\rangle + 2\left(\frac{\partial\overline{u}}{\partial r}\left\langle u'u'\right\rangle + \frac{\partial\overline{u}}{\partial x}\left\langle v'u'\right\rangle\frac{\partial\overline{v}}{\partial r}\left\langle v'v'\right\rangle\right) + \\
&2\left(\frac{\partial\overline{v}}{\partial x}\left\langle v'u'\right\rangle + \frac{\partial\overline{w}}{\partial x}\left\langle w'u'\right\rangle + \frac{\partial\overline{w}}{\partial r}\left\langle w'v'\right\rangle\right) + \frac{\partial\left\langle u'q\right\rangle}{\partial x} + \frac{1}{r}\frac{\partial\left(r\left\langle v'q\right\rangle\right)}{\partial r} +
\end{aligned}$$

$$\frac{2}{r}\left(\overline{v}\left\langle w'w'\right\rangle - \overline{w}\left\langle w'v'\right\rangle\right) = -\frac{2}{\rho}\left(\frac{\partial\left\langle u'p\right\rangle}{\partial x} + \frac{\partial\left\langle v'p\right\rangle}{\partial r}\right) + \epsilon \tag{A.17}$$

Figures B.9 to B.16 support a frequent simplification—i.e., $\overline{v}\left\langle w'w'\right\rangle \approx \overline{w}\left\langle w'v'\right\rangle$—thus producing

$$\begin{aligned} &\left[\left(\overline{u}\frac{\partial}{\partial x} + \overline{v}\frac{\partial}{\partial r}\right)\overline{q}\right]_{\text{advection}} + \\ &\left[2\left(\frac{\partial\overline{u}}{\partial r}\overline{u'u'} + \frac{\partial\overline{u}}{\partial x}\overline{v'u'} + \frac{\partial\overline{v}}{\partial r}\overline{v'v'} + \frac{\partial\overline{v}}{\partial x}\overline{v'u'} + \frac{\partial\overline{w}}{\partial x}\overline{w'u'} + \frac{\partial\overline{w}}{\partial r}\overline{w'v'}\right)\right]_{\text{production}} + \\ &\left[\frac{\partial\overline{u'q}}{\partial x} + \frac{1}{r}\frac{\partial\left(r\overline{v'q}\right)}{\partial r}\right]_{\text{turbulence transport}} \\ &= \left[-\frac{2}{\rho}\left(\frac{\partial\overline{u'p}}{\partial x} + \frac{\partial\overline{v'p}}{\partial r}\right)\right]_{\text{pressure transport}} + \left[\epsilon\right]_{\text{dissipation}} \end{aligned} \tag{A.18}$$

where terms are grouped by physical significance. In addition, samples are temporally and statistically independent and spatially static; therefore, ensemble averaging simplifies to a mean average.

APPENDIX B

VELOCITY PROFILES ACROSS RADIAL CROSS SECTIONS

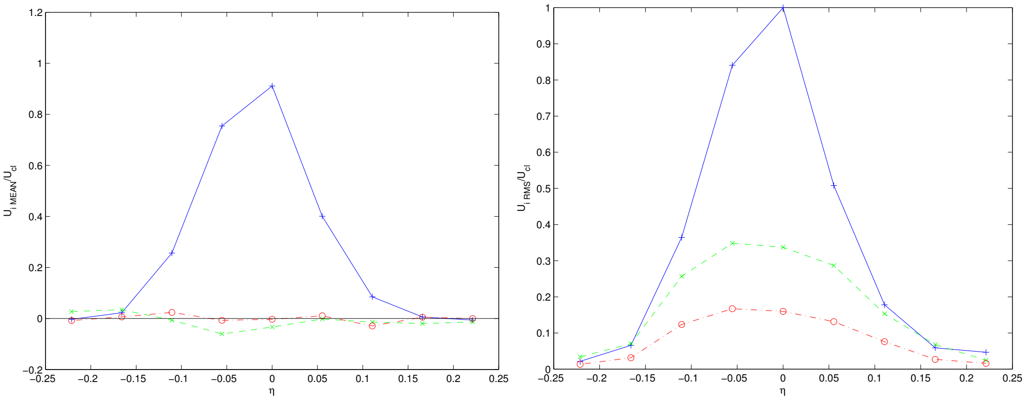

(a) Free jet - Mean (b) Free jet - RMS

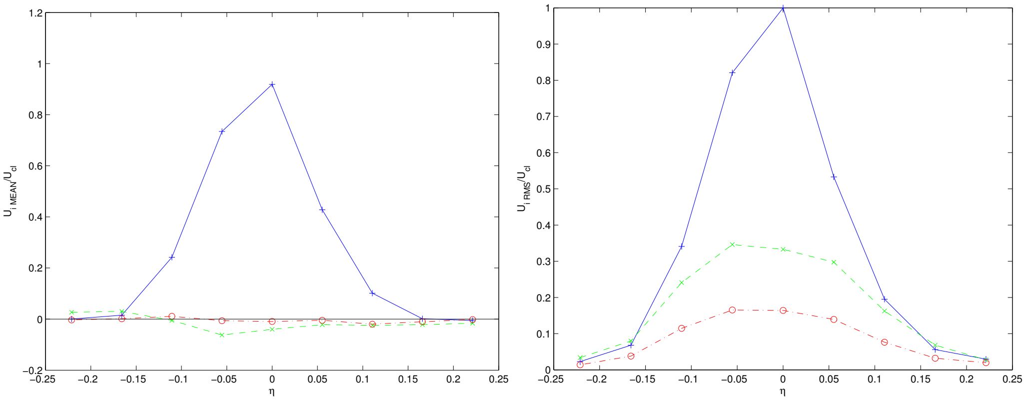

(c) Configuration 1 - Mean (d) Configuration 1 - RMS

Figure B.1: $\overline{\mathrm{u_i}}$ Section 1 of free jet and Configuration 1

$\overline{u}(+)\ \overline{v}(\times)\ \overline{w}(\bigcirc)$

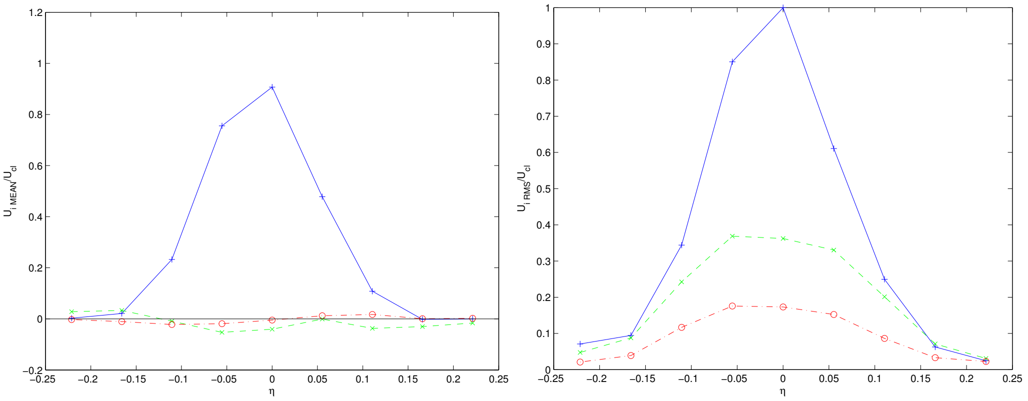

(a) Configuration 2 - Mean (b) Configuration 2 - RMS

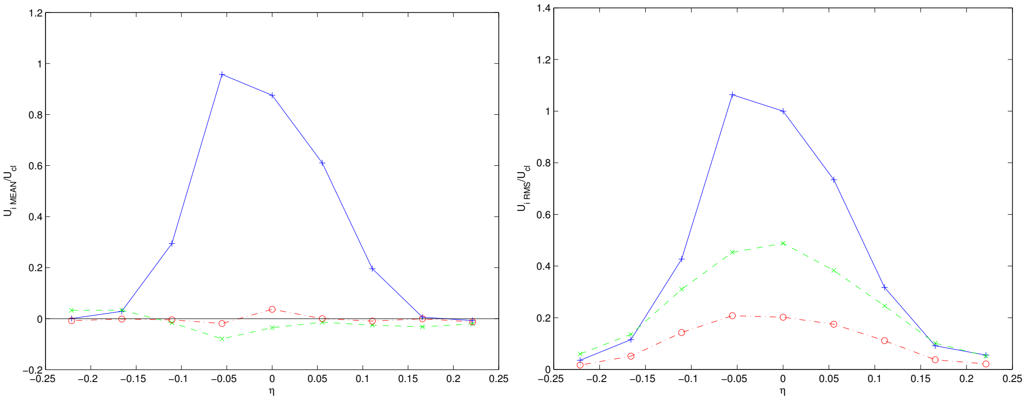

(c) Configuration 3 - Mean (d) Configuration 3 - RMS

Figure B.2: $\overline{\mathrm{u_i}}$ Section 1 of Configurations 2 and 3

$\overline{u}(+)$ $\overline{v}(\times)$ $\overline{w}(\bigcirc)$

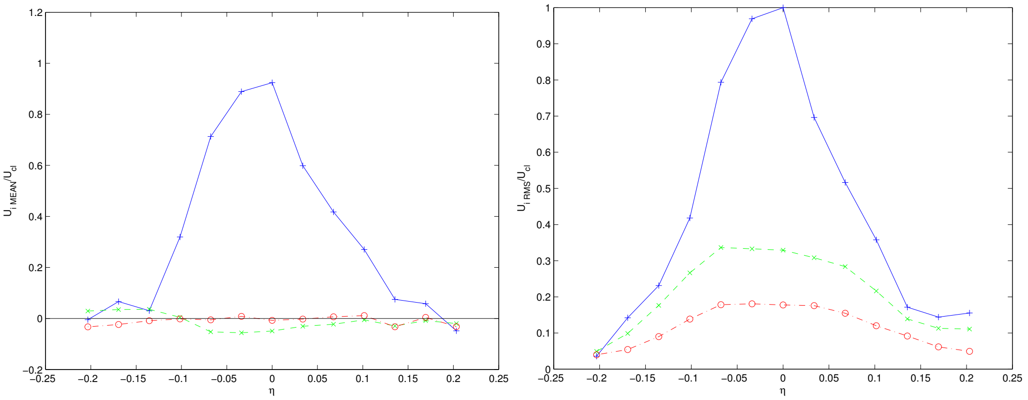

(a) Free jet - Mean (b) Free jet - RMS

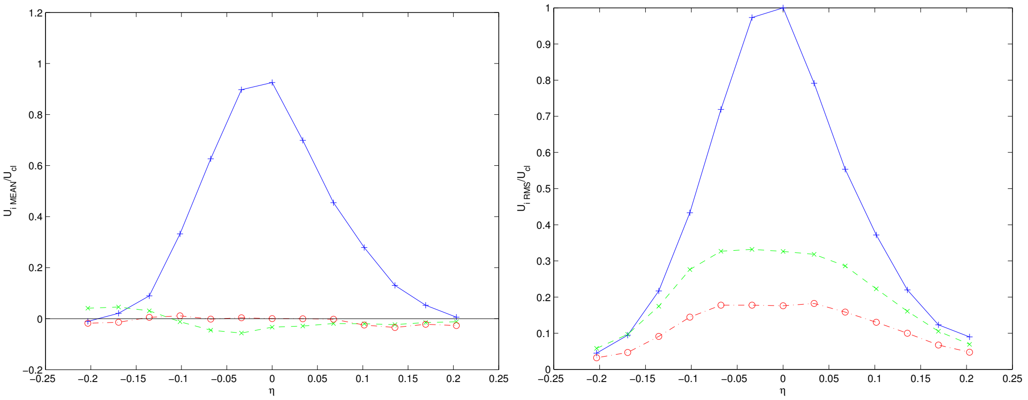

(c) Configuration 1 - Mean (d) Configuration 1 - RMS

Figure B.3: $\overline{\mathrm{u_i}}$ Section 2 of free jet and Configuration 1

$\overline{u}(+)$ $\overline{v}(\times)$ $\overline{w}(\bigcirc)$

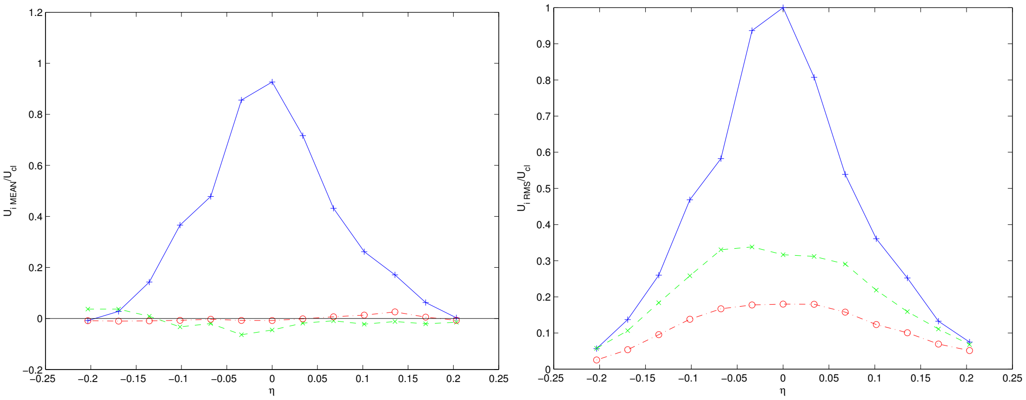

(a) Configuration 2 - Mean (b) Configuration 2 - RMS

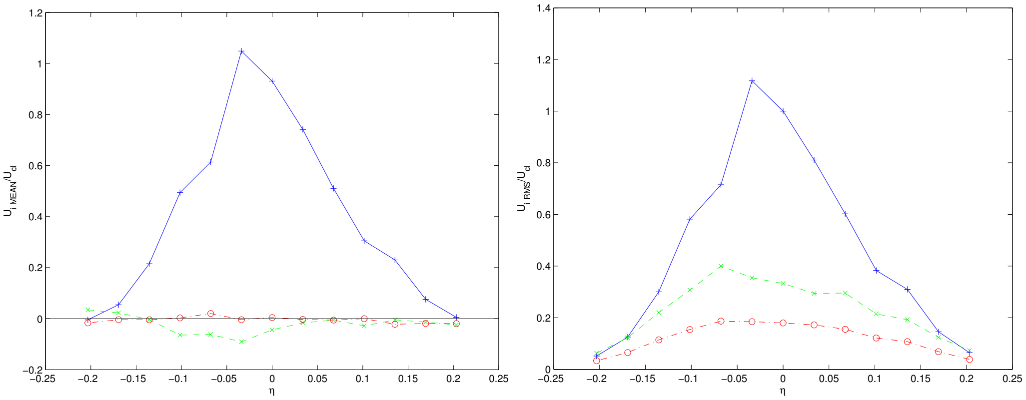

(c) Configuration 3 - Mean (d) Configuration 3 - RMS

Figure B.4: $\overline{\mathrm{u_i}}$ Section 2 of Configurations 2 and 3

$\overline{u}(+)\ \overline{v}(\times)\ \overline{w}(\bigcirc)$

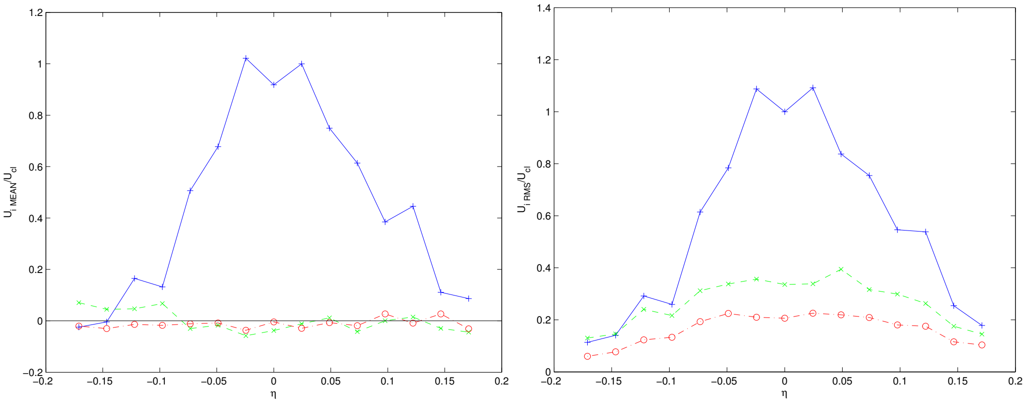

(a) Free jet - Mean (b) Free jet - RMS

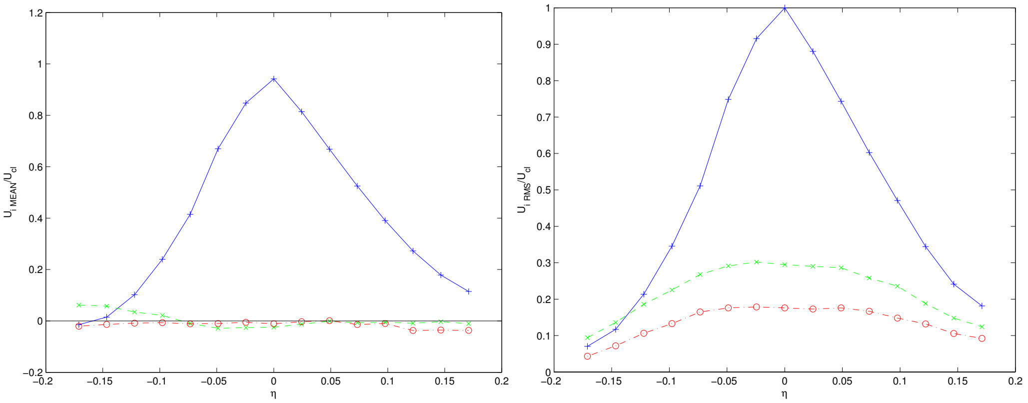

(c) Configuration 1 - Mean (d) Configuration 1 - RMS

Figure B.5: $\overline{\mathrm{u_i}}$ Section 3 of free jet and Configuration 1

$\overline{u}(+)$ $\overline{v}(\times)$ $\overline{w}(\bigcirc)$

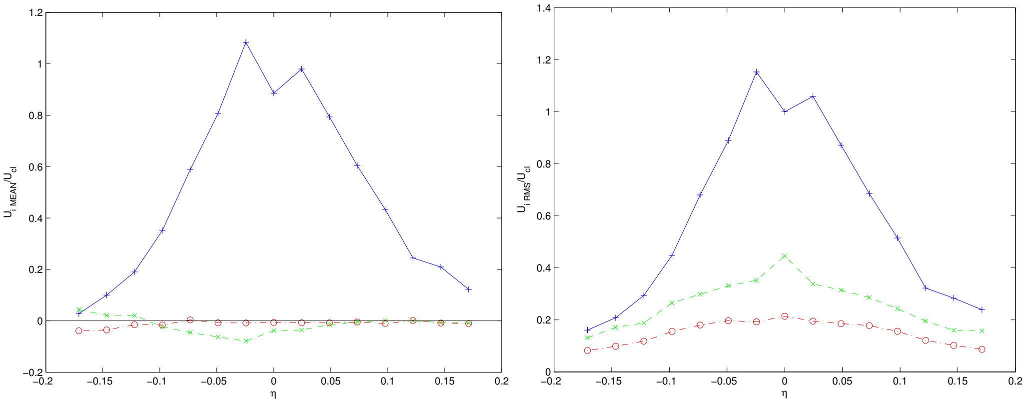

(a) Configuration 2 - Mean (b) Configuration 2 - RMS

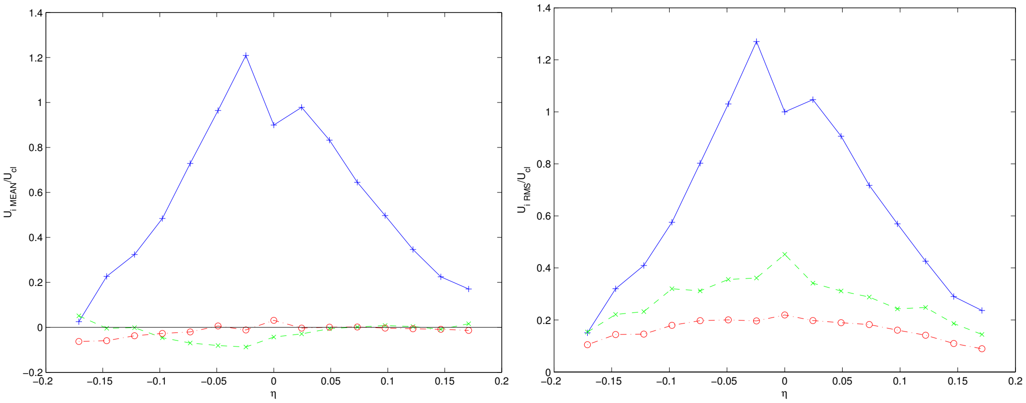

(c) Configuration 3 - Mean (d) Configuration 3 - RMS

Figure B.6: $\overline{\mathrm{u_i}}$ Section 3 of Configurations 2 and 3

$\overline{u}(+)$ $\overline{v}(\times)$ $\overline{w}(\bigcirc)$

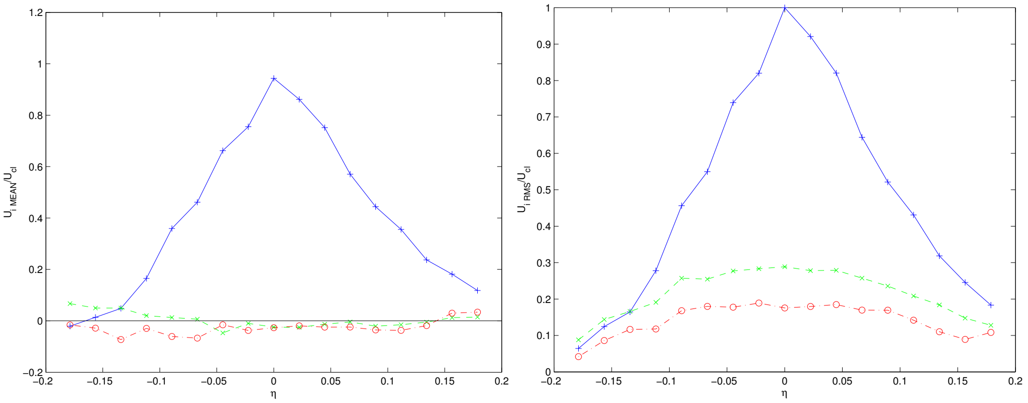

(a) Free jet - Mean (b) Free jet - RMS

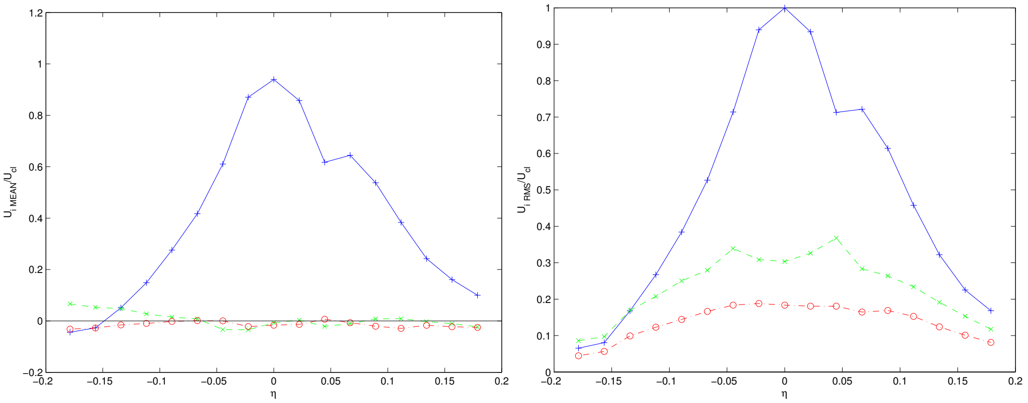

(c) Configuration 1 - Mean (d) Configuration 1 - RMS

Figure B.7: $\overline{\mathrm{u_i}}$ Section 4 of free jet and Configuration 1

$\overline{u}(+)$ $\overline{v}(\times)$ $\overline{w}(\bigcirc)$

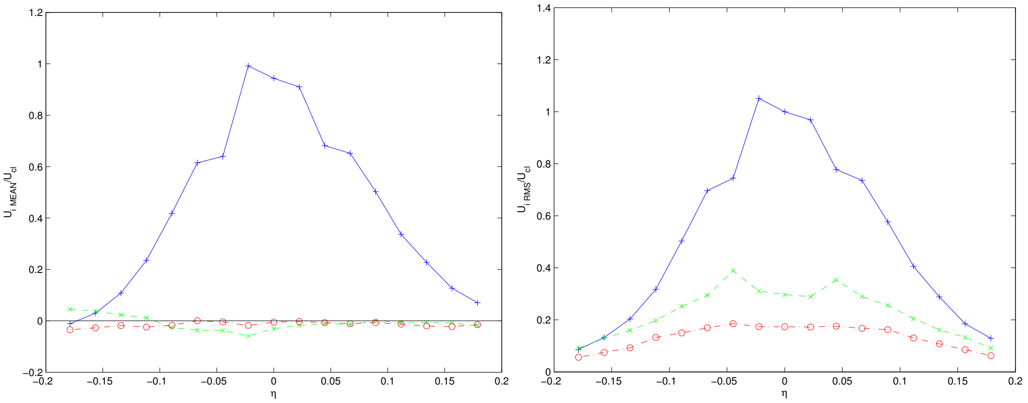

(a) Configuration 2 - Mean (b) Configuration 2 - RMS

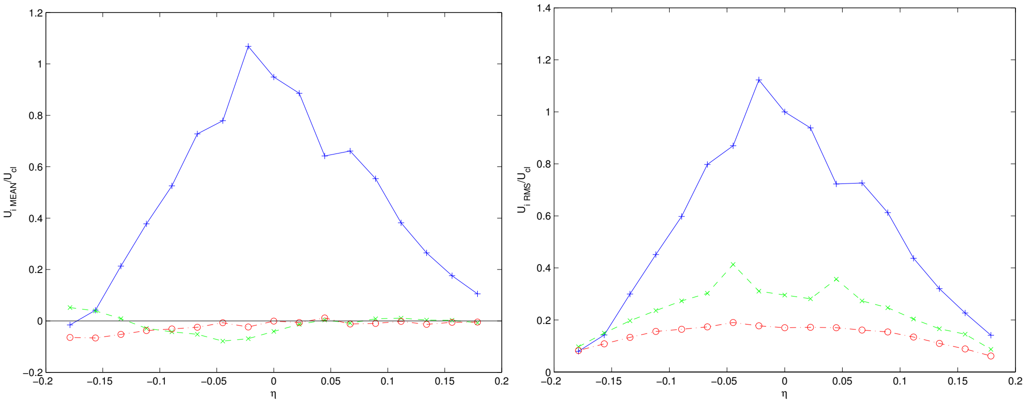

(c) Configuration 3 - Mean (d) Configuration 3 - RMS

Figure B.8: $\overline{\mathrm{u_i}}$ Section 4 of Configurations 2 and 3

$\overline{u}(+)\ \overline{v}(\times)\ \overline{w}(\bigcirc)$

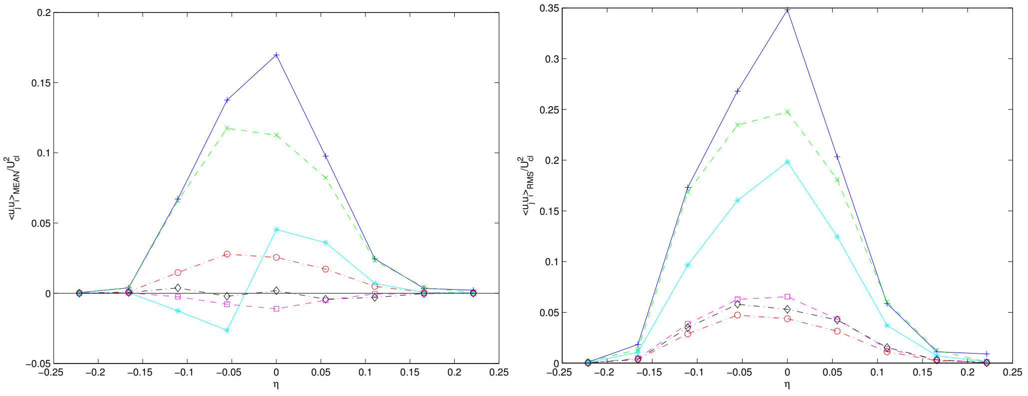

(a) Free jet - Mean (b) Free jet - RMS

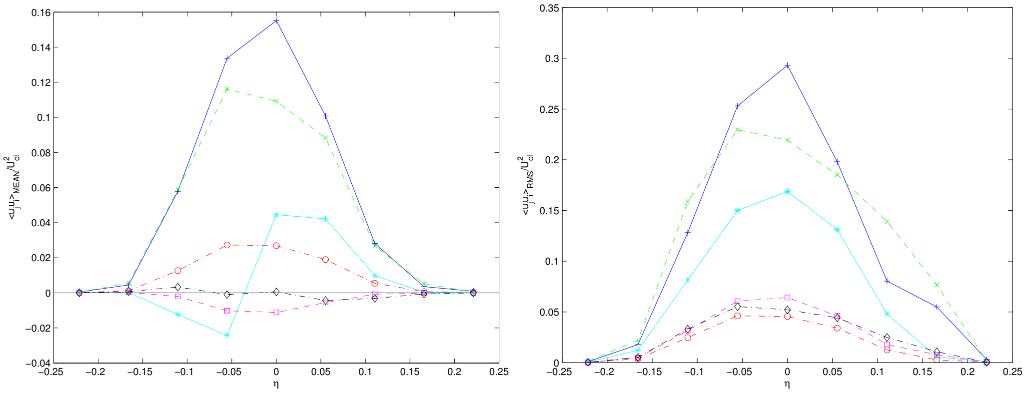

(c) Configuration 1 - Mean (d) Configuration 1 - RMS

Figure B.9: $\overline{\mathrm{u_j'u_i'}}$ Section 1 of free jet and Configuration 1

$\overline{u'u'}(+)$ $\overline{v'v'}(\times)$ $\overline{w'w'}(\bigcirc)$ $\overline{u'v'}(*)$ $\overline{u'w'}(\Box)$ $\overline{v'w'}(\Diamond)$

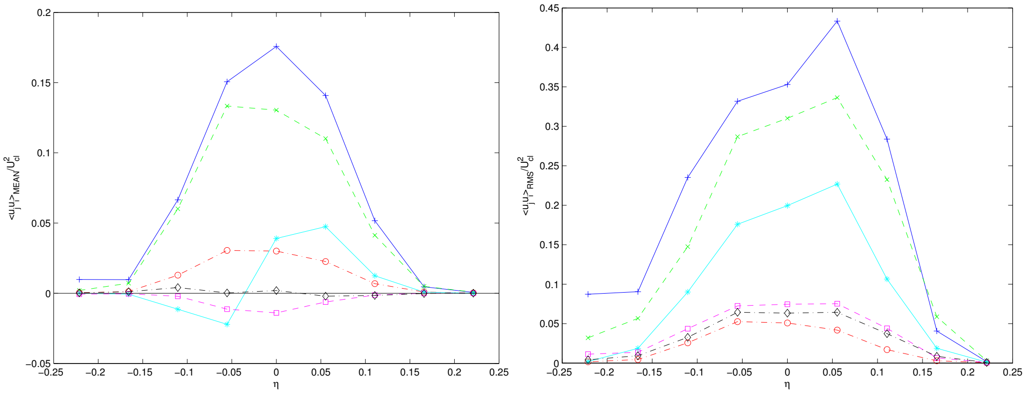

(a) Configuration 2 - Mean (b) Configuration 2 - RMS

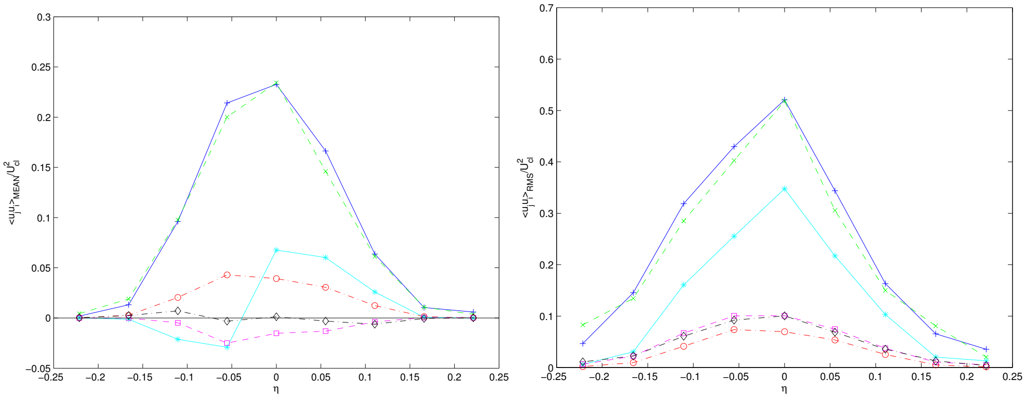

(c) Configuration 3 - Mean (d) Configuration 3 - RMS

Figure B.10: $\overline{\mathrm{u'_j u'_i}}$ Section 1 of Configurations 2 and 3

$\overline{u'u'}(+)$ $\overline{v'v'}(\times)$ $\overline{w'w'}(\bigcirc)$ $\overline{u'v'}(*)$ $\overline{u'w'}(\Box)$ $\overline{v'w'}(\Diamond)$

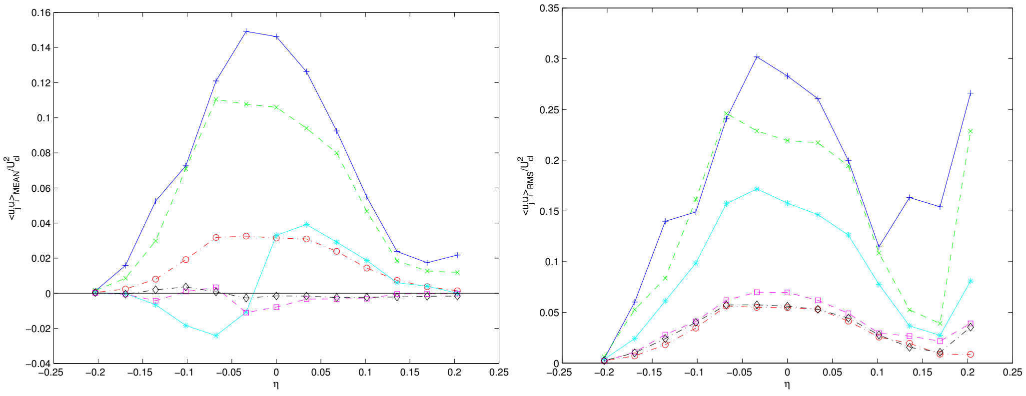

(a) Free jet - Mean

(b) Free jet - RMS

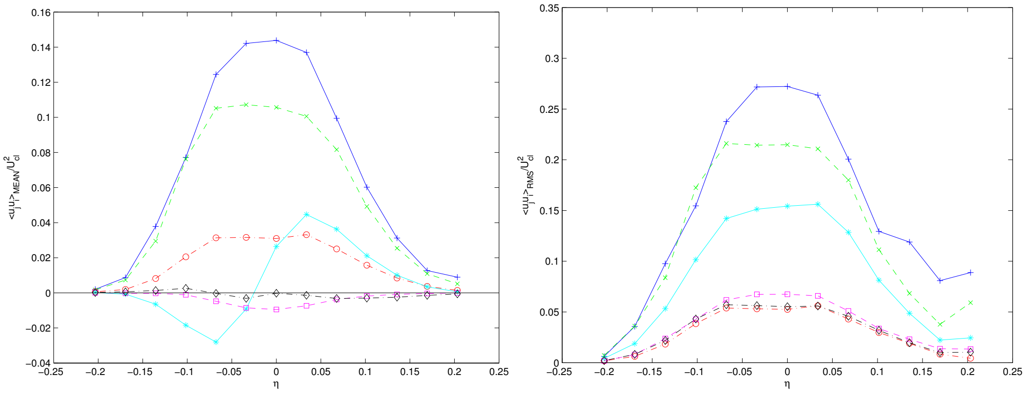

(c) Configuration 1 - Mean

(d) Configuration 1 - RMS

Figure B.11: $\overline{\mathrm{u}'_{\mathrm{j}}\mathrm{u}'_{\mathrm{i}}}$ Section 2 of free jet and Configuration 1

$\overline{u'u'}(+)$ $\overline{v'v'}(\times)$ $\overline{w'w'}(\bigcirc)$ $\overline{u'v'}(*)$ $\overline{u'w'}(\Box)$ $\overline{v'w'}(\Diamond)$

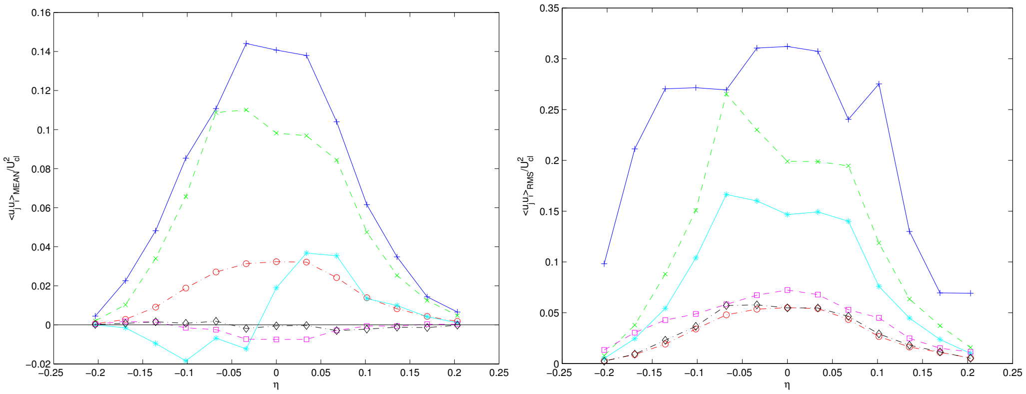

(a) Configuration 2 - Mean

(b) Configuration 2 - RMS

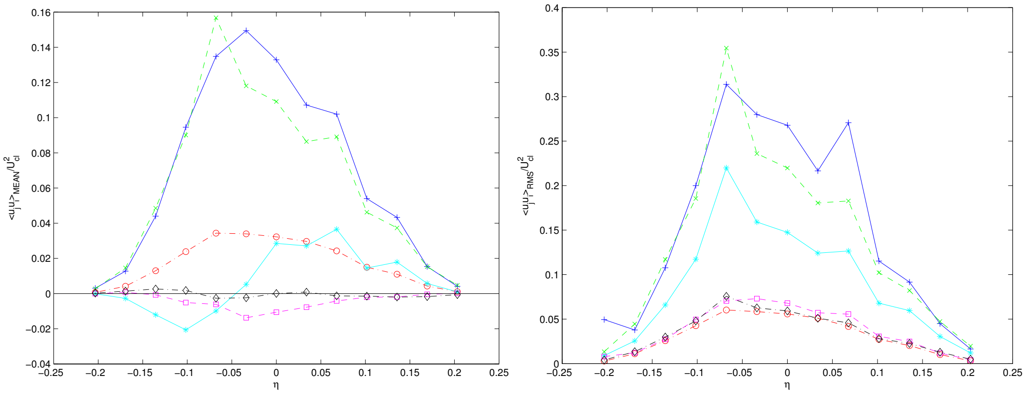

(c) Configuration 3 - Mean

(d) Configuration 3 - RMS

Figure B.12: $\overline{\mathrm{u'_j u'_i}}$ Section 2 of Configurations 2 and 3

$\overline{u'u'}(+)$ $\overline{v'v'}(\times)$ $\overline{w'w'}(\bigcirc)$ $\overline{u'v'}(*)$ $\overline{u'w'}(\Box)$ $\overline{v'w'}(\Diamond)$

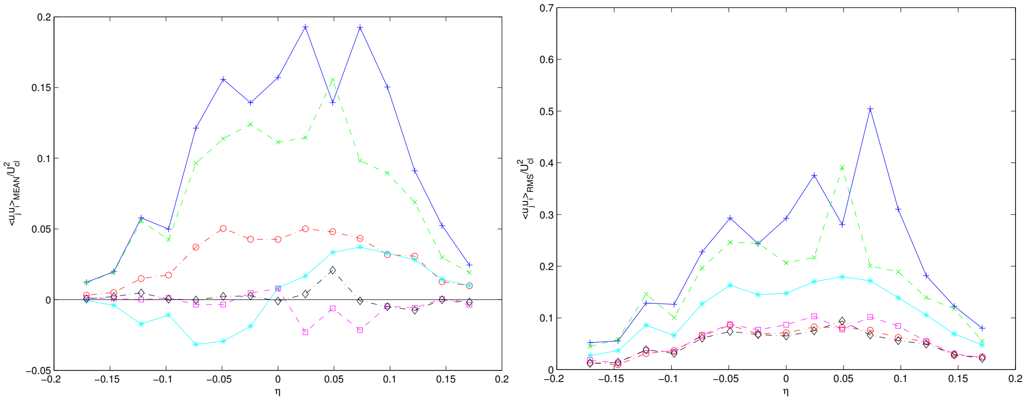

(a) Free jet - Mean (b) Free jet - RMS

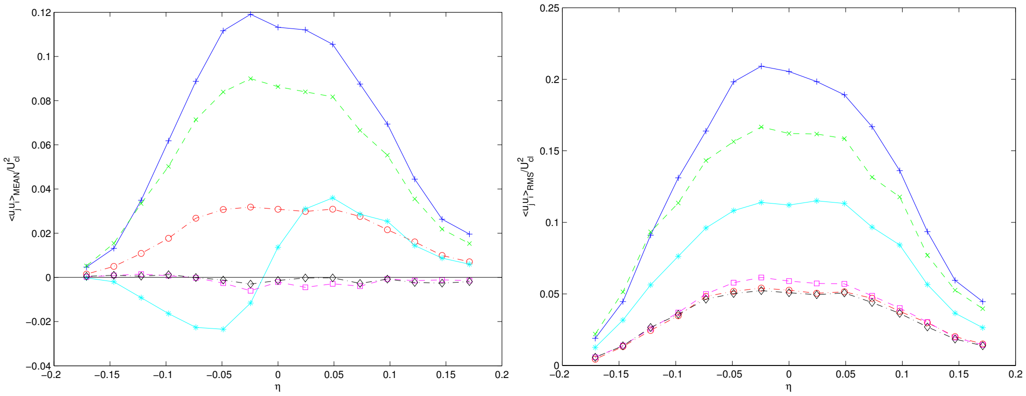

(c) Configuration 1 - Mean (d) Configuration 1 - RMS

Figure B.13: $\overline{\mathrm{u_j'u_i'}}$ Section 3 of free jet and Configuration 1

$\overline{u'u'}(+)$ $\overline{v'v'}(\times)$ $\overline{w'w'}(\bigcirc)$ $\overline{u'v'}(*)$ $\overline{u'w'}(\Box)$ $\overline{v'w'}(\Diamond)$

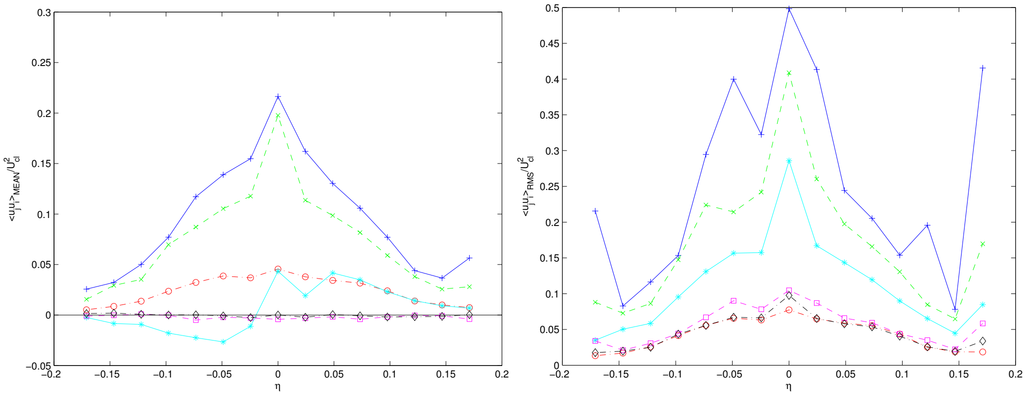

(a) Configuration 2 - Mean

(b) Configuration 2 - RMS

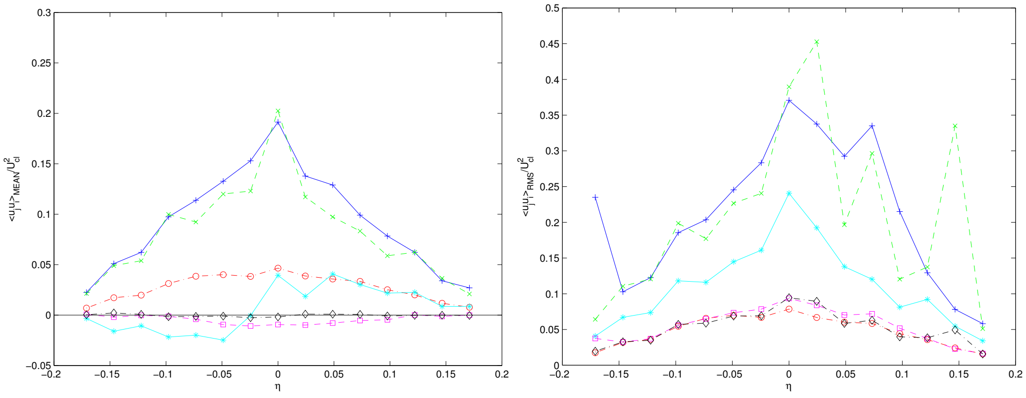

(c) Configuration 3 - Mean

(d) Configuration 3 - RMS

Figure B.14: $\overline{\mathrm{u_j'u_i'}}$ Section 3 of Configurations 2 and 3

$\overline{u'u'}(+)$ $\overline{v'v'}(\times)$ $\overline{w'w'}(\bigcirc)$ $\overline{u'v'}(*)$ $\overline{u'w'}(\Box)$ $\overline{v'w'}(\Diamond)$

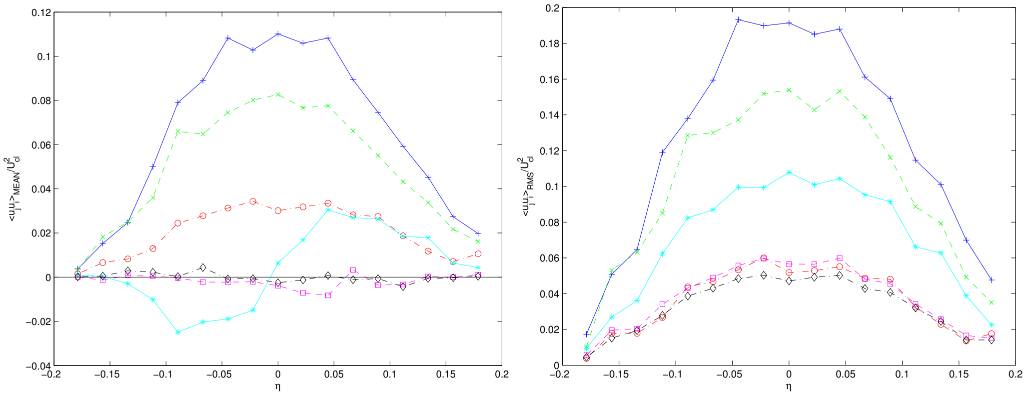

(a) Free jet - Mean (b) Free jet - RMS

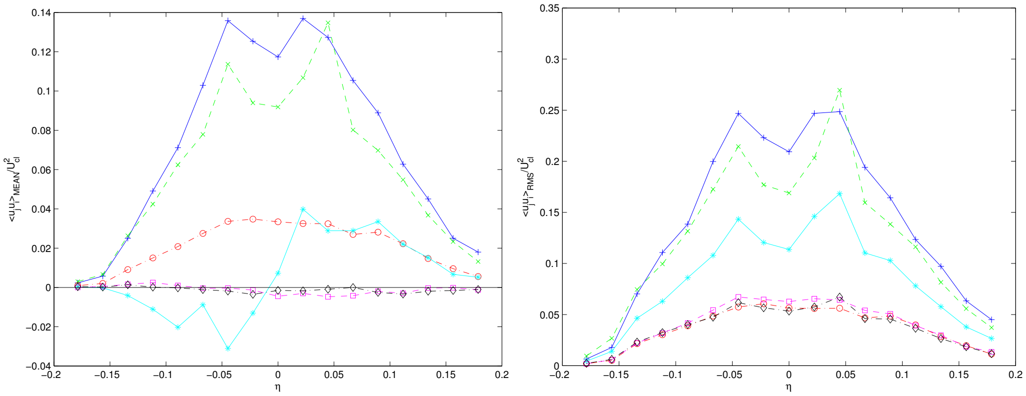

(c) Configuration 1 - Mean (d) Configuration 1 - RMS

Figure B.15: $\overline{\mathrm{u'_j u'_i}}$ Section 4 of free jet and Configuration 1

$\overline{u'u'}(+)$ $\overline{v'v'}(\times)$ $\overline{w'w'}(\bigcirc)$ $\overline{u'v'}(*)$ $\overline{u'w'}(\Box)$ $\overline{v'w'}(\Diamond)$

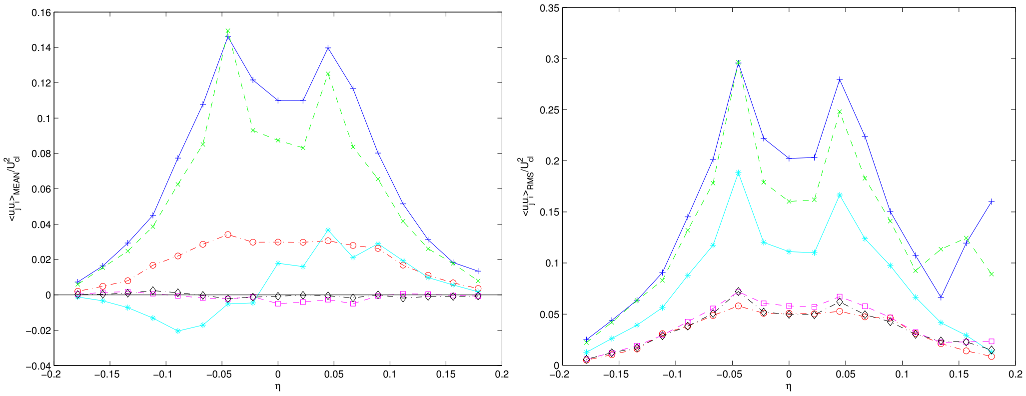

(a) Configuration 2 - Mean (b) Configuration 2 - RMS

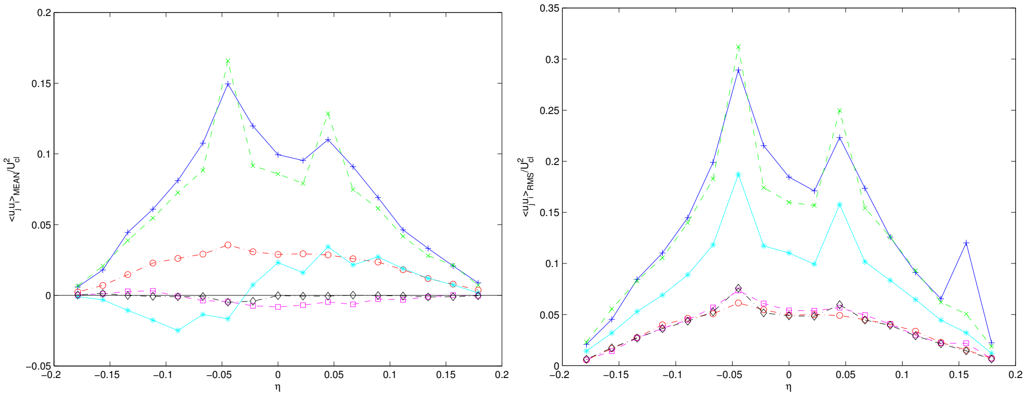

(c) Configuration 3 - Mean (d) Configuration 3 - RMS

Figure B.16: $\overline{\mathrm{u'_j u'_i}}$ Section 4 of Configurations 2 and 3

$\overline{u'u'}(+)$ $\overline{v'v'}(\times)$ $\overline{w'w'}(\bigcirc)$ $\overline{u'v'}(*)$ $\overline{u'w'}(\Box)$ $\overline{v'w'}(\Diamond)$

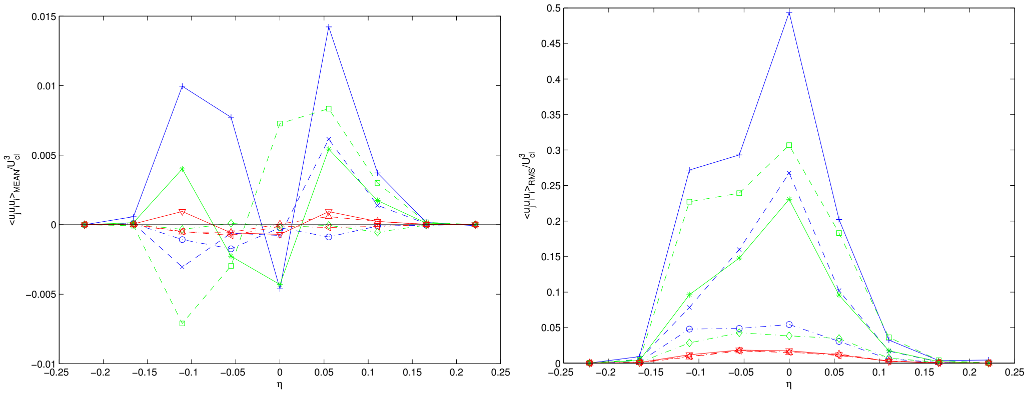

(a) Free jet - Mean (b) Free jet - RMS

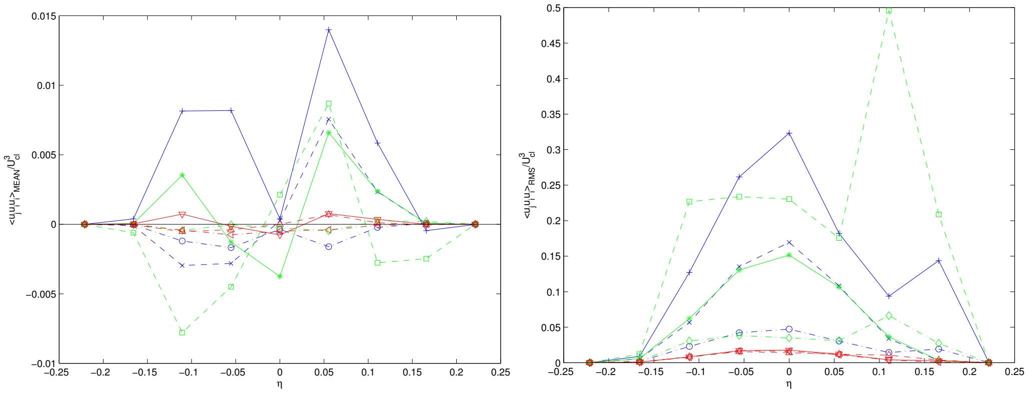

(c) Configuration 1 - Mean (d) Configuration 1 - RMS

Figure B.17: $\overline{\mathrm{u'_j u'_i u'_i}}$ Section 1 of free jet and Configuration 1

$\overline{u'u'u'}(+)$ $\overline{u'v'v'}(\times)$ $\overline{u'w'w'}(\bigcirc)$ $\overline{v'u'u'}(*)$ $\overline{v'v'v'}(\square)$

$\overline{v'w'w'}(\Diamond)$ $\overline{w'u'u'}(\bigtriangledown)$ $\overline{w'v'v'}(\triangle)$ $\overline{w'w'w'}(\triangleleft)$

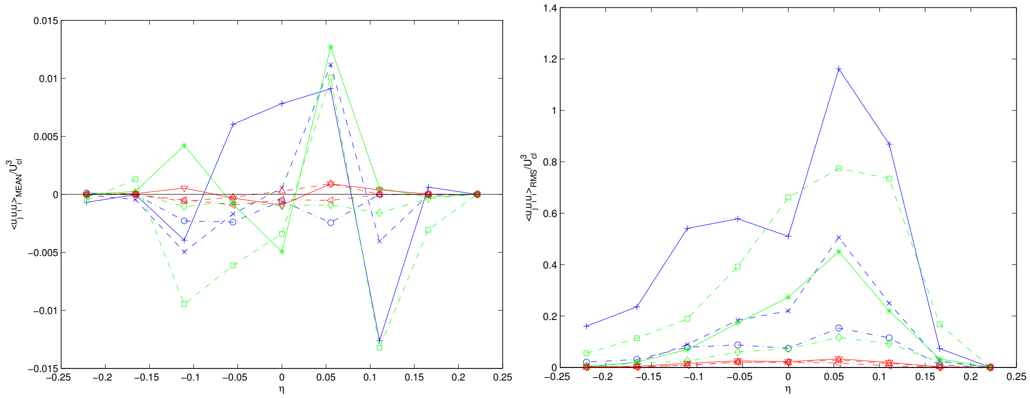

(a) Configuration 2 - Mean

(b) Configuration 2 - RMS

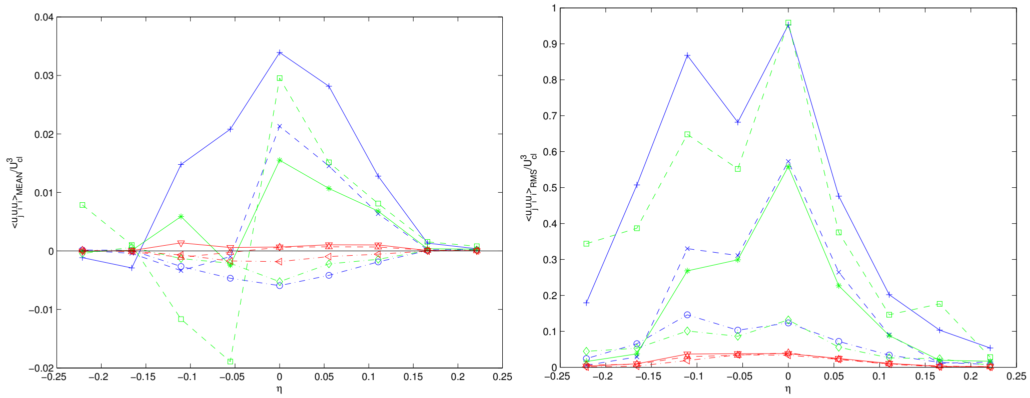

(c) Configuration 3 - Mean

(d) Configuration 3 - RMS

Figure B.18: $\overline{\mathrm{u}'_j\mathrm{u}'_i\mathrm{u}'_i}$ Section 1 of Configurations 2 and 3

$\overline{u'u'u'}(+)$ $\overline{u'v'v'}(\times)$ $\overline{u'w'w'}(\bigcirc)$ $\overline{v'u'u'}(*)$ $\overline{v'v'v'}(\Box)$

$\overline{v'w'w'}(\Diamond)$ $\overline{w'u'u'}(\bigtriangledown)$ $\overline{w'v'v'}(\bigtriangleup)$ $\overline{w'w'w'}(\triangleleft)$

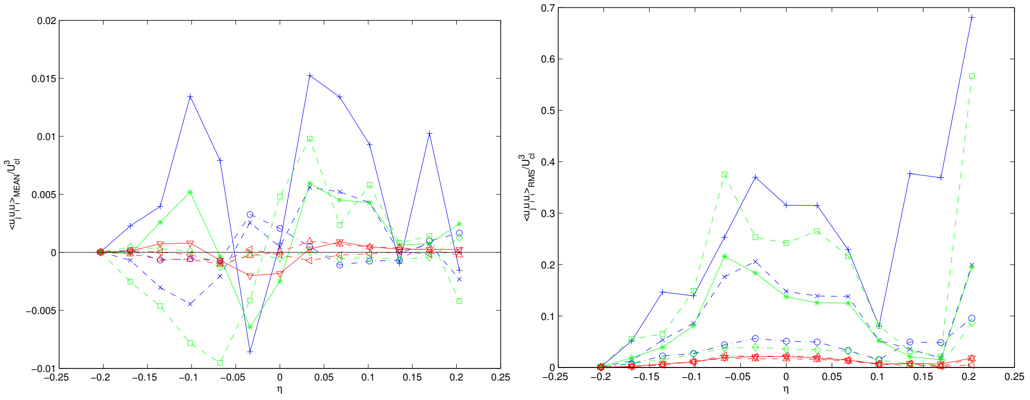

(a) Free jet - Mean (b) Free jet - RMS

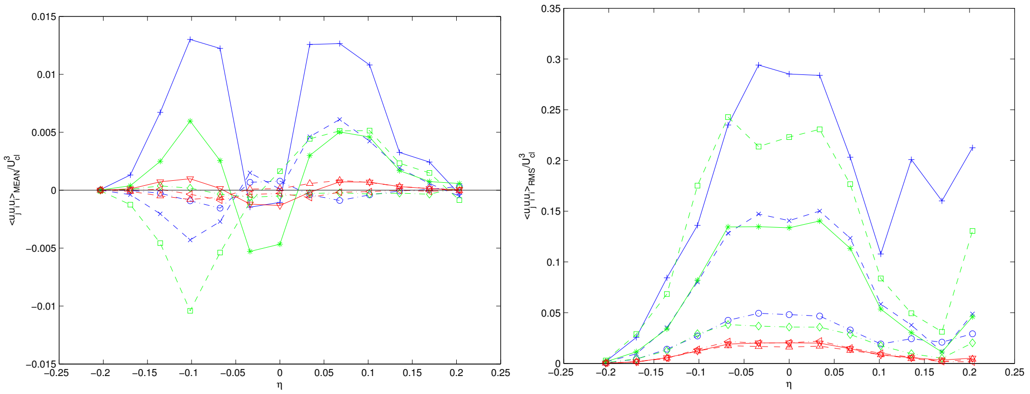

(c) Configuration 1 - Mean (d) Configuration 1 - RMS

Figure B.19: $\overline{\mathrm{u_j'u_i'u_i'}}$ Section 2 of free jet and Configuration 1

$\overline{u'u'u'}(+)$ $\overline{u'v'v'}(\times)$ $\overline{u'w'w'}(\bigcirc)$ $\overline{v'u'u'}(*)$ $\overline{v'v'v'}(\square)$

$\overline{v'w'w'}(\Diamond)$ $\overline{w'u'u'}(\bigtriangledown)$ $\overline{w'v'v'}(\bigtriangleup)$ $\overline{w'w'w'}(\triangleleft)$

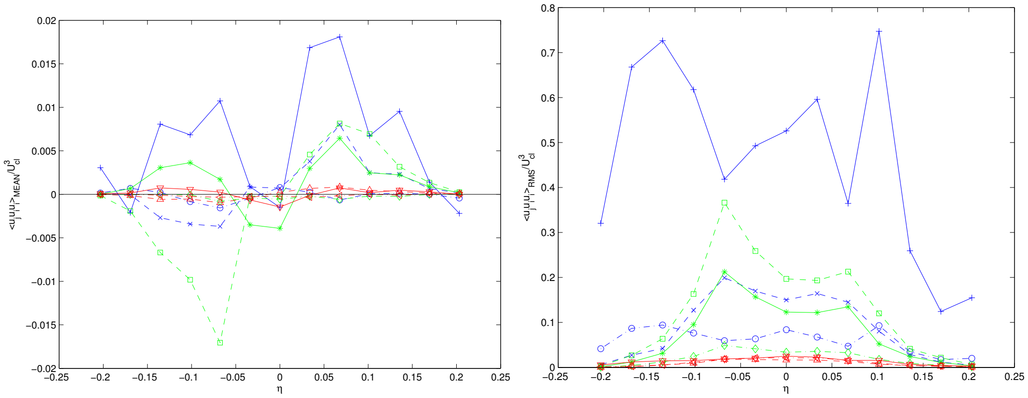

(a) Configuration 2 - Mean (b) Configuration 2 - RMS

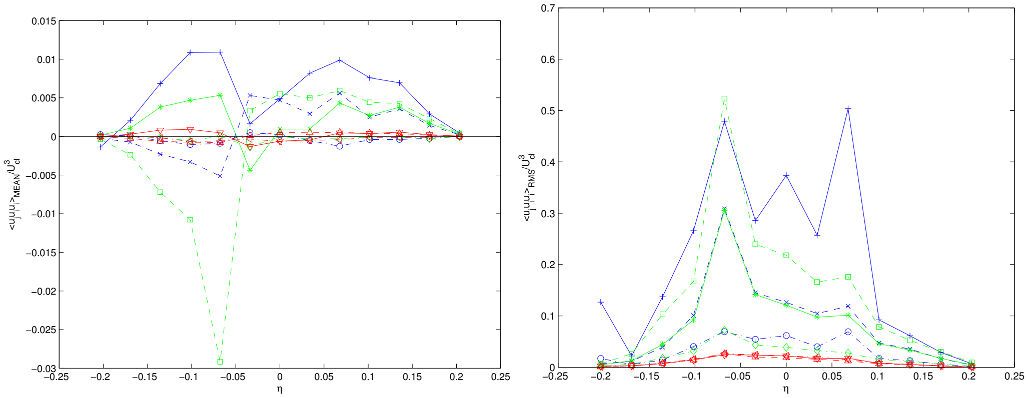

(c) Configuration 3 - Mean (d) Configuration 3 - RMS

Figure B.20: $\overline{u'_j u'_i u'_i}$ Section 2 of Configurations 2 and 3

$\overline{u'u'u'}(+)$ $\overline{u'v'v'}(\times)$ $\overline{u'w'w'}(\bigcirc)$ $\overline{v'u'u'}(*)$ $\overline{v'v'v'}(\Box)$

$\overline{v'w'w'}(\Diamond)$ $\overline{w'u'u'}(\bigtriangledown)$ $\overline{w'v'v'}(\bigtriangleup)$ $\overline{w'w'w'}(\triangleleft)$

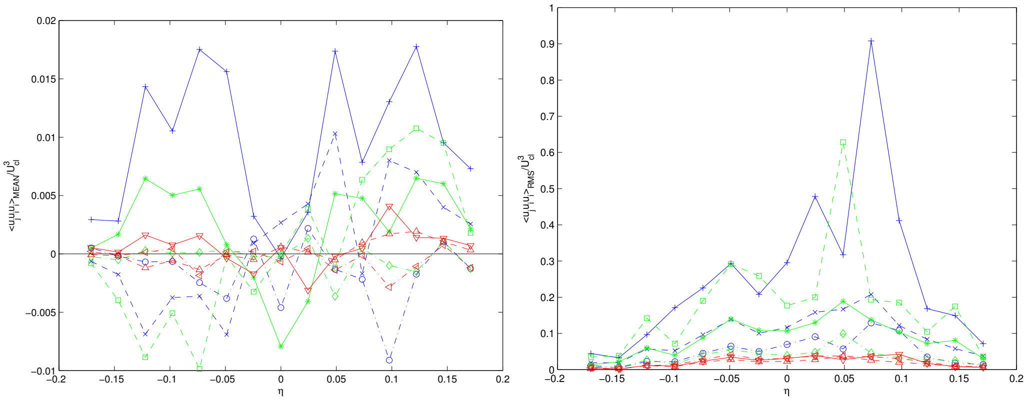

(a) Free jet - Mean

(b) Free jet - RMS

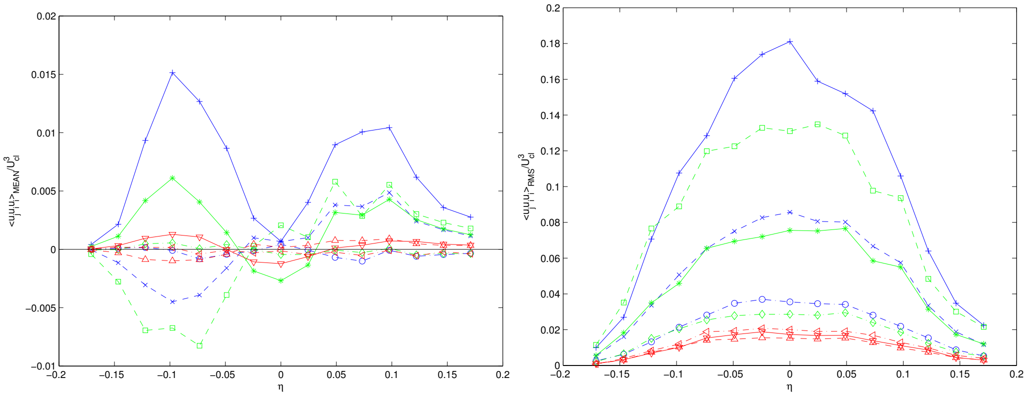

(c) Configuration 1 - Mean

(d) Configuration 1 - RMS

Figure B.21: $\overline{\mathrm{u_j'u_i'u_i'}}$ Section 3 of free jet and Configuration 1

$\overline{u'u'u'}(+)$ $\overline{u'v'v'}(\times)$ $\overline{u'w'w'}(\bigcirc)$ $\overline{v'u'u'}(*)$ $\overline{v'v'v'}(\square)$

$\overline{v'w'w'}(\Diamond)$ $\overline{w'u'u'}(\bigtriangledown)$ $\overline{w'v'v'}(\bigtriangleup)$ $\overline{w'w'w'}(\triangleleft)$

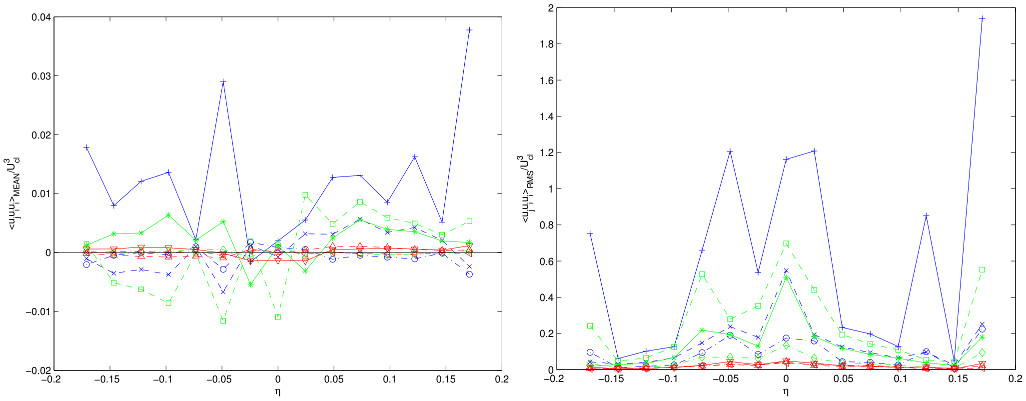

(a) Configuration 2 - Mean (b) Configuration 2 - RMS

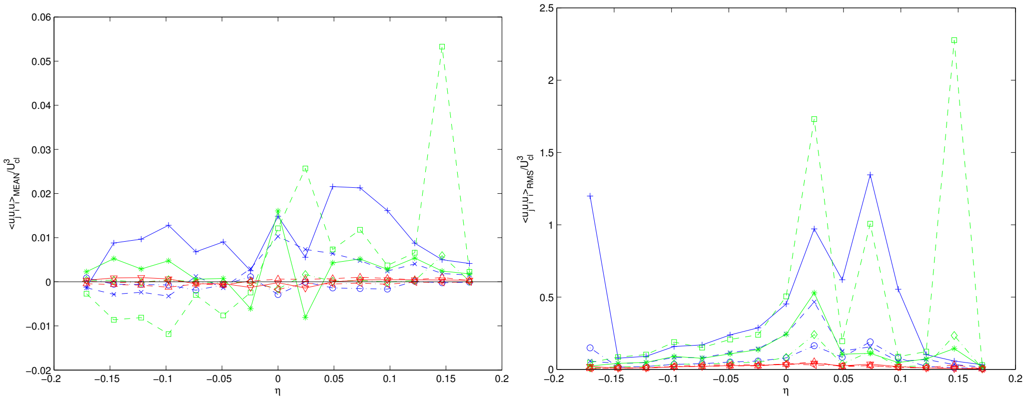

(c) Configuration 3 - Mean (d) Configuration 3 - RMS

Figure B.22: $\overline{\mathrm{u}_j'\mathrm{u}_i'\mathrm{u}_i'}$ Section 3 of Configurations 2 and 3

$\overline{u'u'u'}(+)$ $\overline{u'v'v'}(\times)$ $\overline{u'w'w'}(\bigcirc)$ $\overline{v'u'u'}(*)$ $\overline{v'v'v'}(\Box)$

$\overline{v'w'w'}(\Diamond)$ $\overline{w'u'u'}(\bigtriangledown)$ $\overline{w'v'v'}(\bigtriangleup)$ $\overline{w'w'w'}(\triangleleft)$

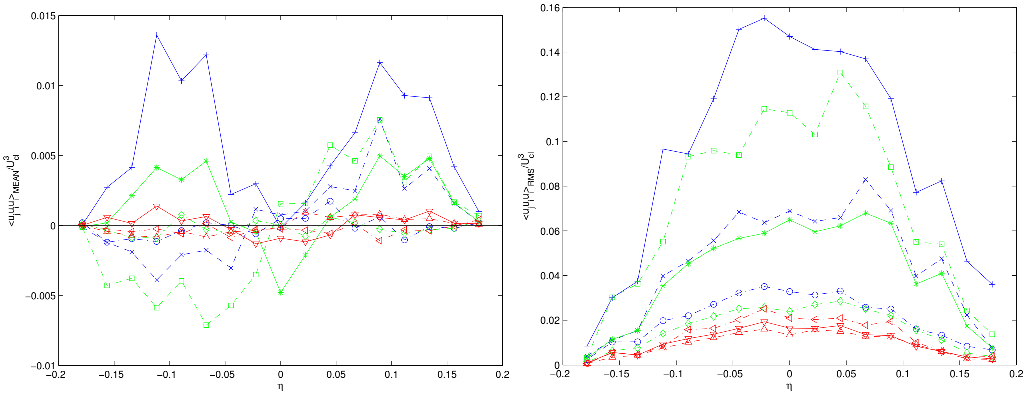

(a) Free jet - Mean (b) Free jet - RMS

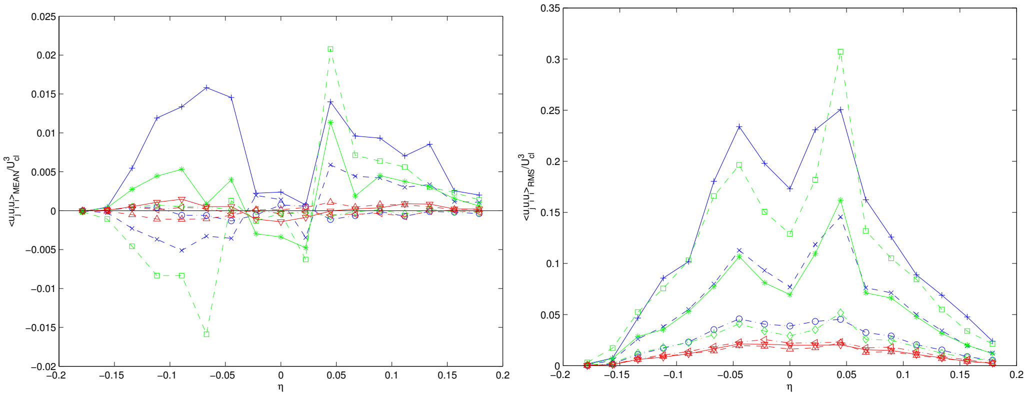

(c) Configuration 1 - Mean (d) Configuration 1 - RMS

Figure B.23: $\overline{\mathrm{u}'_j \mathrm{u}'_i \mathrm{u}'_i}$ Section 4 of free jet and Configuration 1

$\overline{u'u'u'}(+)$ $\overline{u'v'v'}(\times)$ $\overline{u'w'w'}(\bigcirc)$ $\overline{v'u'u'}(*)$ $\overline{v'v'v'}(\Box)$

$\overline{v'w'w'}(\Diamond)$ $\overline{w'u'u'}(\bigtriangledown)$ $\overline{w'v'v'}(\bigtriangleup)$ $\overline{w'w'w'}(\triangleleft)$

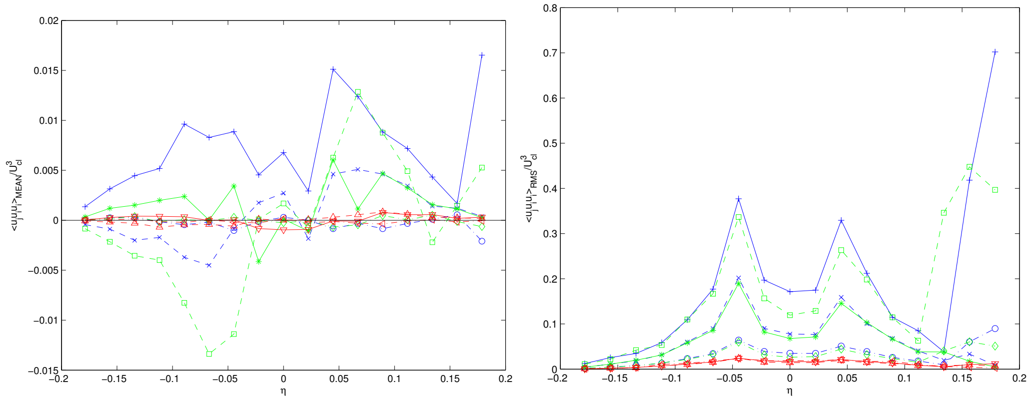

(a) Configuration 2 - Mean (b) Configuration 2 - RMS

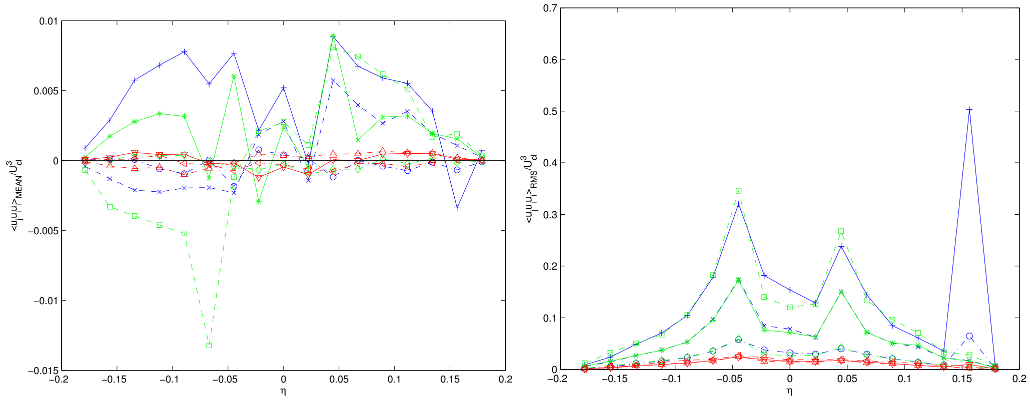

(c) Configuration 3 - Mean (d) Configuration 3 - RMS

Figure B.24: $\overline{\mathrm{u_j'u_i'u_i'}}$ Section 4 of Configurations 2 and 3

$\overline{u'u'u'}(+)$ $\overline{u'v'v'}(\times)$ $\overline{u'w'w'}(\bigcirc)$ $\overline{v'u'u'}(*)$ $\overline{v'v'v'}(\Box)$

$\overline{v'w'w'}(\Diamond)$ $\overline{w'u'u'}(\bigtriangledown)$ $\overline{w'v'v'}(\bigtriangleup)$ $\overline{w'w'w'}(\triangleleft)$